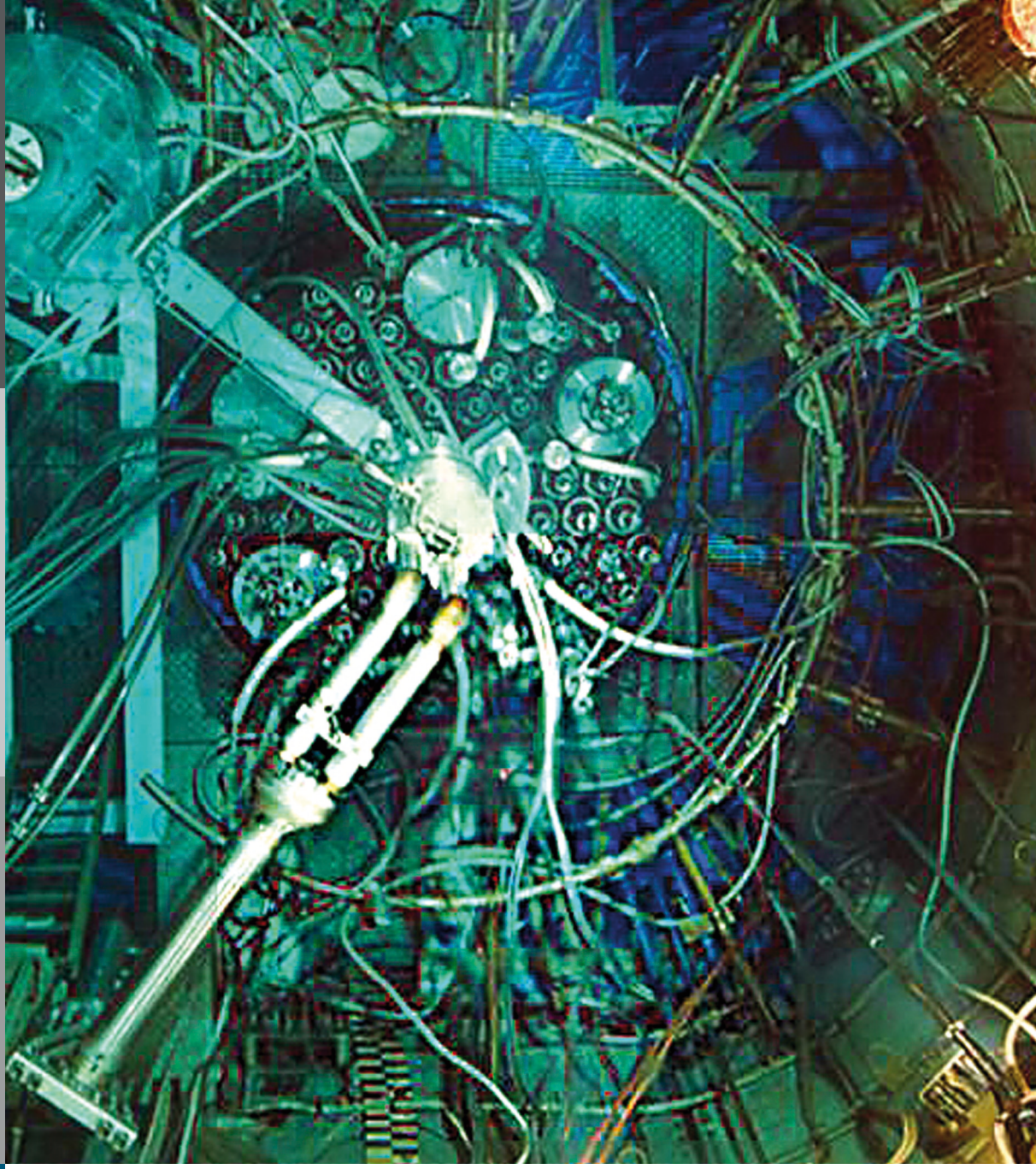

Neutron-Irradiation + Helium Hardening & Embrittlement Modeling of 9%Cr-Steels in an Engineering Perspective (HELENA)

Rachid Chaouadi

Mitglied der Helmholtz-Gemeinschaft

JÜLICH
FORSCHUNGSZENTRUM

Schriften des Forschungszentrums Jülich
Reihe Energie & Umwelt / Energy & Environment Band / Volume 20

Forschungszentrum Jülich GmbH
Institut für Energieforschung (IEF)
Werkstoffstruktur und Eigenschaften (IEF-2)

Neutron-Irradiation + Helium Hardening & Embrittlement Modeling of 9%Cr-Steels in an Engineering Perspective (HELENA)

Rachid Chaouadi

Schriften des Forschungszentrums Jülich
Reihe Energie & Umwelt / Energy & Environment Band / Volume 20

ISSN 1866-1793 ISBN 978-3-89336-545-6

Bibliographic information published by the Deutsche Nationalbibliothek.
The Deutsche Nationalbibliothek lists this publication in the Deutsche Nationalbibliografie; detailed bibliographic data are available in the Internet at http://dnb.d-nb.de.

Publisher and Distributor: Forschungszentrum Jülich GmbH
Zentralbibliothek, Verlag
D-52425 Jülich
phone:+49 2461 61-5368 · fax:+49 2461 61-6103
e-mail: zb-publikation@fz-juelich.de
Internet: http://www.fz-juelich.de/zb

Cover Design: Grafische Medien, Forschungszentrum Jülich GmbH

Printer: Grafische Medien, Forschungszentrum Jülich GmbH

Schriften des Forschungszentrums Jülich
Reihe Energie & Umwelt / Energy & Environment Band / Volume 20

ISSN 1866-1793
ISBN 978-3-89336-545-6

The complete volume is freely available on the Internet on the Jülicher Open Access Server (JUWEL) at http://www.fz-juelich.de/zb/juwel

"Experiments are never wrong,
it is our judgment or interpretation that is wrong"

Leonardo Da Vinci
(1452 – 1519)

ABSTRACT

This report provides a physically–based engineering model to estimate the radiation hardening of 9%Cr–steels under both displacement damage (dpa) and helium. The model is essentially based on the dispersed barrier hardening theory and the dynamic re–solution of helium under displacement cascades. However, a number of assumptions and simplifications were considered to obtain a simple description of irradiation hardening and embrittlement primarily relying on the available experimental data. As a result, two components were basically identified, the dpa component that can be associated with black dots and small loops and the He–component accounting for helium bubbles. The dpa component is strongly dependent on the irradiation temperature and its dependence law was based on a first–order annealing kinetics. The damage accumulation law was also modified to take saturation into account. Finally, the global kinetics of the damage accumulation kept defined, its amplitude is fitted to one experimental condition. The model was rationalized on an experimental database that mainly consists of ~9%Cr–steels irradiated in the technologically important temperature range of 50 to 600°C up to 50 dpa and with a He-content up to ~5000 appm, including neutron and proton irradiation as well as implantation. The test temperature effect is taken into account through a normalization procedure based on the change of the Young's modulus and the anelastic deformation that occurs at high temperature. Finally, the hardening–to–embrittlement correlation is obtained using the load diagram approach.
Despite the large experimental scatter, inherent to the variety of the materials and irradiation as well as testing conditions, the obtained results are very promising. Improvement of the model performance is still possible by including He–hardening saturation and high temperature softening but unfortunately, at this stage, a number of conflicting experimental data reported in literature should first be clarified.

ACKNOWLEDGEMENTS

This work was performed within the HELENA project, in the frame of an Intra European Fellowship sponsored by the European Commission. The views and opinions expressed herein do not necessarily reflect those of the European Commission.
The author is indebted to Dr. Jochen Linke, leader of the Fusion Materials Group at IEF-2, and Prof. L. Singheiser, Director of IEF-2 at Forschungszentrum Jülich for all the support and encouragements they provided to achieve the HELENA project.
The author acknowledges the support of H. Aït Abderrahim, P. d'Hondt, C. Legrain, L. Mertens and E. van Walle from SCK•CEN without whom his sabbatical leave would have not been possible.
Within the Fusion Materials Group, many thanks to the dream team: "Takeshi, Gerald, Jérémie, Katrien, Guillaume, Gerd and Gaby under the guidance of Jochen".
Also, the author expresses grateful acknowledgements to Prof. H. Ullmaier, Dr. H. Trinkaus and Dr. P. Jung for their encouragements and fruitful discussions. The author had the opportunity to visit a number of laboratories involved in the field of radiation damage and helium effects and is very thankful to Prof. A. Kimura and Dr. R. Kasada from Kyoto University, Dr. J. Dai and Dr. J. Chen from PSI Villigen and Dr. N. Yamamoto from NIMS Tsukuba. Great thanks to W. Vandermeulen for reviewing the document.

TABLE OF CONTENTS

EXECUTIVE SUMMARY

Background

A number of new nuclear systems are under development worldwide including fusion systems, fission reactors of the fourth generation and accelerator driven systems. In the design phase of such nuclear components, it is important that engineers can rely on the material property database not only in the baseline (unirradiated) condition but also on their behavior upon irradiation. While the material properties in the unirradiated condition can easily be determined, their post–irradiation behavior is more complicated to assess for two main reasons. The first is related to the inherent difficulty of characterizing irradiated materials (hot cells, excessive costs, …). The second is associated with the difficulty to provide representative conditions which are not accessible with available irradiation instruments. In the systems that were cited above, not only displacement damage but also helium generation will be present. It is important therefore to estimate the evolution of the mechanical properties when both dpa and He are present.

Scope and objectives

The HELENA project was initiated primarily to provide engineering tools that can be used to assess the material behavior under the combined effect of displacement and helium damage. Radiation damage results in a significant hardening and embrittlement of the material. Because of its engineering orientation, it is important to provide a procedure that can easily be implemented in engineering design. The property that is of prime importance is fracture toughness or more specifically the resistance against brittle fracture of the materials. Unfortunately, for most irradiated data, this is not straightforward but instead obtained through a correlation procedure. Namely, the fracture toughness transition curve is obtained by equating the shift of the transition temperature to the shift of the ductile–to–brittle transition temperature (DBTT) obtained from Charpy impact data.

Modeling Approach

Because of its engineering nature, the modeling that is developed here is based on the following strategy. It is clear that commercial materials are very complicated and differ significantly from model alloys such as binary or ternary alloys, single crystals … A number of assumptions or simplifications are required to be able to model their behavior. However, rather than doing this empirically, a physically-based approach is preferred. In other words, available physical understanding should be reflected by the model. For example, if a diffusion mechanism is involved in the investigated process, the diffusion equation should appear in the model. However, while the kinetics should follow some of these physical laws, the amplitude of the material variables can be fitted on the experimental results without losing their physical significance. For example, the activation energy of a physical process can be fixed to a specific value, lower or higher than in a simple system but the order of magnitude should be conserved.

The model is based on two components, the first one related to radiation damage (dpa–damage) while the second is related to helium damage (He–damage). Both components are essentially based on the dispersed barrier hardening theory. For the dpa component,

the effect of irradiation temperature is rationalized using the annealing data associated with a first–order annealing kinetics. The fluence dependence was modified to account for hardening (defect) saturation. The dpa–component can be written as:

$$\Delta\sigma_y^{dpa} \approx C_{dpa} \times \exp\left[-\nu \exp\left(-\frac{\Gamma}{k\,T_{irrad}}\right)\right] \times \sqrt{1-\exp\left(-\frac{\Phi}{\Phi_0^{dpa}}\right)}$$

where Φ is the neutron dose, T_{irrad} is the irradiation temperature, k is the Boltzmann constant, and C_{dpa}, ν, Γ and Φ_0^{dpa} are constants.

The He-component is based on the Trinkaus [J. Nucl. Mater. 318 (2003) 234–240] description of dynamic re-solution of helium bubbles under displacement cascades in the temperature range of interest (50 – 600°C). The He-component is given by:

$$\Delta\sigma_y^{He} \approx C_{He} \times \left\{\beta\left(\dot{\phi} \times (He/dpa)\right)^{m-2} / \dot{\phi}^3\, D^2\right\}^{1/2m} \sqrt{\Phi - \Phi_{He}^{threshold}}$$

where $\dot{\phi}$ is the dpa rate (K), (He/dpa) is the Helium–to–dpa rate, $\Phi_{He}^{threshold}$ is the threshold dose below which no He–effect is observed, D is the He–diffusion coefficient ($D = D_0 \exp\left(-\frac{U_a}{kT_{irrad}}\right)$, U_a=0.93 eV is the He–migration energy, $D_0 \approx 10^{-5}$ m^{2}s^{-1} is a temperature independent constant) and β and m are constants ($\beta \approx 10^{-30}$ m^4, m = 7).

For each component, the hardening amplitude is fitted on one experimental condition. The total hardening is obtained through a linear (p=1) or quadratic (p=2) superposition law.

$$\Delta\sigma_{total} = \left(\Delta\sigma_{dpa}^p + \Delta\sigma_{He}^p\right)^{1/p}$$

The available data and their large scatter do not allow to unambiguously prefer one or another superposition law. In the case of a quadratic superposition law (p = 2), the constants of the model are: C_{dpa} = 500 MPa, $\nu = 10^7$, Γ = 0.9 eV, Φ_0^{dpa} = 3 dpa, C_{He} = 300 MPa, U_a=0.93 eV, $D_0 \approx 10^{-5}$ m^{2}s^{-1}, $\Phi_{He}^{threshold} = \Phi_{500\ appm\ He}$ dpa, $\beta \approx 10^{-30}$ m^4, m = 7.

Experimental database

Irradiation effects on structural materials are usually monitored by examination of their irradiation–induced hardening and embrittlement and these are often measured using tensile and Charpy impact tests (DBTT). Unfortunately, the DBTT data can be misleading. Moreover, they are comparatively scarce in comparison to tensile data. It was shown that the hardening can be correlated to embrittlement using a physically–based load diagram concept. Therefore, the tensile data, or more specifically the yield strength, were selected to build the experimental database.

A literature survey showed that in order to have a representative database, it was necessary, in a first step, to incorporate various heats of the generic 9%Cr–steels and to

ignore their differences in terms of chemical composition and heat treatments. In a subsequent step, chemical composition will be examined in few cases.

Because available experimental data were obtained either at room temperature or, more often, at the irradiation temperature, it was necessary to normalize all data to a single reference temperature, namely room temperature (25°C). The normalization procedure takes the change of the Young's modulus temperature dependence into account together with the anelastic deformation that appears at high temperature. As a result, the normalized yield strength (to room temperature) can be derived as :

$$\Delta\sigma_y^{RT} \approx \frac{1-\alpha' T_{RT}}{1-\alpha' T} \times \Delta\sigma_y^{T}$$

where: $\alpha' = 2.67\ 10^{-4}\ K^{-1}$ if $T \leq RT$

$\alpha' = 5.5\ 10^{-4}\ K^{-1}$ if $600°C > T > RT$

The validity of this relation was demonstrated on a number of experimental data.

The literature survey that was carried out resulted in gathering a large number of tensile data on various 9%Cr–steels. The above mentioned normalization procedure was applied to all experimental data of the database to estimate the irradiation hardening at room temperature.

Findings

Despite the number of assumptions and the relative simplicity of the two–component model, the obtained results are very promising. It is very important to emphasize that because of the simplicity of the model developed in this work, cancellation of the contributions of other components such as chemical composition or spectrum and rate effects are not excluded. The simplicity of the presented model is dictated by the available experimental database. The database that was used is not ideal and a number of conflicting data are still not resolved. In particular, the effect of irradiation temperature is not fully clear. It was also assumed that, contrary to the dpa–contribution, the He–contribution does not saturate. Actually, it should but available data do not allow to reliably account for this saturation. The appropriate superposition law also cannot be assessed because of the lack of experimental data in the desired range.
It is clear that the present model in its simple form can be improved but this cannot be done without additional experimental data. Nevertheless, the present model can help in defining the appropriate experiments to be performed, as this is also one of the main objectives of modeling.

Recommendations for further research

The variety of materials heats, heat treatments, irradiation reactors, environmental conditions (temperature, dpa, , …) call for a radiation monitoring system that allows verification of the experimental results. It is highly recommended to include a monitor material that should be used in each irradiation setup.
Irradiation temperature effects should definitely be clarified. It is highly recommended to investigate this effect by minimizing other variables that also affect the material response. This means that a single material with identical specimen configurations should be

irradiated in the same reactor at different temperatures. This should be complemented by some post–irradiation annealing experiments.

One of the database gaps is the high dose – high He region. Specimens for such region can be obtained by combining He–implantation with subsequent neutron irradiation. By varying irradiation and implantation temperatures, dpa–levels and He–contents, the database can be clearly enlarged and improved.

A more systematic study on the correlation between the various properties would be very helpful. A tool such as the load diagram is recommended and should be experimentally demonstrated. It should also be desirable to include experimental data where the microcleavage fracture stress is affected by irradiation. Miniaturized specimens should be used together with standard ones to validate these geometries. This is very important in the perspective of IFMIF where the space availability is very critical.

I. INTRODUCTION

The successful implementation of fusion reactors as an efficient source of electrical power generation requires the resolution of a number of critical issues set down by the structural materials, in particular those of the first wall, divertors, limiters and breeding–blanket components. These components are not only submitted to classical loading such as thermo–mechanical stresses but also to neutron irradiation that drastically modifies the material properties. The materials that constitute these components should be therefore qualified to ensure their optimum performance and safe operation [1-5]. The latter is extremely important in the nuclear context.
Hence, the interaction of high energy neutrons with metallic structural materials leads to a number of radiation damage phenomena, including hardening, embrittlement, irradiation creep, void swelling, and hydrogen– and helium–embrittlement.

In absence of irradiation, structural integrity calculations together with a material property databank allow a quasi–straightforward selection of the appropriate material for a specific application. Upon irradiation, the physical and mechanical properties of the material are significantly modified and they are not easily quantifiable. Three important objectives of modeling were pointed out by Odette [6]:

- it provides a framework in which the validity of the proposed mechanisms can be quantitatively assessed;
- it provides a guide to design and to interpretation of the experimental results;
- it provides a systematic physical basis for extrapolation.

There are a number of reasons why difficulties are encountered for evaluating the performances of such materials, among which the three following.

- First of all, these difficulties are inherent to the radioactive character of such irradiated materials. In other words, the materials become highly activated necessitating hot cells utilization.
- Second, it is impossible or very difficult to reproduce the actual service conditions of operation of the materials to be characterized and evaluated.
- Third, the irradiation and testing costs prohibit evaluation of the complete testing matrix. As a result, only scarce data are usually available to determine the materials properties in the irradiated condition.

Besides the objectives outlined above, the importance of modeling finds essentially its origin in the resolution of the abovementioned difficulties. Indeed, a model can easily cover a much larger spectrum of operation conditions while it has been developed on the basis of fewer conditions. However, by modeling, it is not meant very accurate physical modeling as this is neither feasible nor possible nowadays. Rather, the modeling that is considered here is of engineering nature, with the ultimate goal to cover as much as reasonably possible the main parameters needed to describe the phenomenon. In other words, the model should be simplified to its most simple formulation taking into account the major influencing elements and including any physical background whenever available. This means that empirical description or empirical constants are accepted only when no alternative way is available. As a matter of fact, the model should be constrained

by the kinetics of the physical phenomena on one hand, and on the other hand the amplitude is fixed by the experimental observations. Such an engineering type of modeling approach was also used for other materials, such as reactor pressure vessel steels [7-11] and austenitic steels [12-18]. However, while displacement damage is the dominant damage mechanisms, the effect of helium damage was not quantified. The main objective of the present work is to quantitatively estimate the contribution of helium and dpa to the hardening and embrittlement of 9%Cr–steels. These steels are indeed seriously considered for application in a number of nuclear components including fusion, fission and spallation environments. It is important to mention however that all data presented in this report concern base metal only meaning that weldments are excluded. Although 9%Cr–steels and weldments have a number of similarities, the irradiation behavior could be similar [19] or different [20-21].

I.1. Engineering Modeling Methodology

Recent trends indicate an extensive interest in radiation damage modeling using computer simulations within the frame of the so-called multi–scale modeling approach [22-28]. Although this approach is very important and desirable to pursue, it has today not the capacity to predict commercially–available materials behavior under irradiation. Indeed, while atomic–scale modeling considers simple systems such as binary or ternary alloys, commercial materials cannot easily be represented by these model alloys. Commercial alloys contain dozens of alloying elements and many of them, although in small proportions, can drastically affect their radiation resistance. Therefore, another approach, in parallel to atomic–scale modeling, should be promoted in order to provide tools that can be used for engineering purpose, in particular for material selection and component design. This approach, illustrated in Figure 1 combines mainly three ingredients, the microstructural observations, the mechanical properties and materials science in a single framework.

There are other alternatives to the modeling approach selected here that were reported recently. The first one due to Kemp et al. [29] proposes an artificial neural network approach to analyze irradiation hardening of ferritic/martensitic steels. Unfortunately, the success of such an approach is very much dependent on the database quality and as will be seen later, this is not yet sufficient as many gaps in the database should still be filled. The second one, much closer to the one proposed in this work, was proposed by Yamamoto et al. [30] who collected a large database on radiation hardening and embrittlement of 9%Cr–steels and developed a semi–empirical model to rationalize the experimental observations. Their analysis has provided a number of insights on the effects of some variables but there was no systematic application of the model and comparison to the experimental observations.

In the engineering approach, the general concept is to simplify as much as reasonably possible the mechanisms responsible for the material degradation. This means that second–order mechanisms will be neglected or lumped in a single “not fully resolved” term which is of empirical nature. In reactor pressure vessel (RPV) steel embrittlement, this approach was used very often with success. Three damage mechanisms are

considered in RPV hardening and embrittlement, copper precipitate hardening, matrix damage and phosphorus segregation, and although a number of empirical parameters were included, the phenomenological description is often physically-based. This means that it is not a "simple" mathematical fit of a number of experimental data but rather is "constrained" by some physical laws. In other words, the magnitude can be fitted to experimental results but the phase or the kinetics should be described by a simplified physical model. This means that if the physics indicates an exponential dependence with respect to a variable while experimental data show a linear dependence, it is the exponential form that should be taken.

For the problematic of helium, the same strategy as in RPV steel embrittlement will be considered. This means that besides hardening due to precipitates, to point defect clusters and dislocations [31-32], we will consider in addition helium. However, this is not so simple because depending on the material (microstructure) and irradiation conditions (irradiation temperature) the helium will affect the material properties differently.

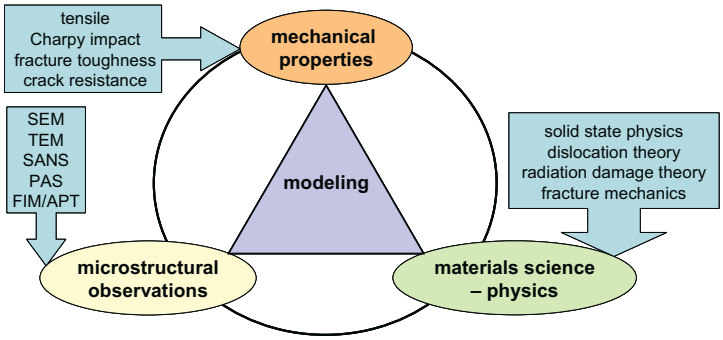

Figure 1. Ingredients needed in an engineering modeling approach.

I.2. Report Outline

In the following, the main keywords included in the title will be clearly specified, in particular the meaning of hardening and embrittlement, the engineering methodology that was selected and the application to 9%Cr–steels.

The monitoring of irradiation effects is usually based on the change of mechanical properties. Therefore, irradiation hardening and embrittlement and their correlation will be presented in section 2. In section 3, the main results of the literature review on irradiation effects on 9%Cr–steels will be given. The experimental database also based on the literature will be detailed in section 4. Section 5 will detail the main elements of the model. Application of the proposed model will be given in section 6 while the discussion of a number of critical issues will be given in section 7. Final conclusions and recommendations will follow in sections 8 and 9, respectively.

What is actually reported in literature? In most cases, tensile data (yield and ultimate tensile strengths, uniform and total elongation) and Charpy impact data, more precisely the ductile–to–brittle transition temperature (DBTT) and upper shelf energy, are the data that are reported. Sometimes – if not very often – the data are not published but are plotted in Figures. Then, only the yield strength increase and the DBTT–increase are usually plotted as a function of neutron dose. Sometimes, the data are reported as a function of irradiation temperature. Unfortunately, such Figures are misleading as the test temperature is taken equal to the irradiation temperature. Moreover, the neutron dose varies often in a large range. Also, the DBTT may vary depending on the way it is determined and also the specimen size may be different (standard Charpy versus sub-sized samples). Some experimental data although from irradiations in different reactors (neutron spectrum, neutron flux) with probably different dosimetry measurements are reported in a single diagram. As a result, the uncertainties on the conclusions when considering all these experimental biases may be very large.

II. IRRADIATION HARDENING AND EMBRITTLEMENT

2.1. Hardening versus embrittlement

In this report, focus is put on neutron radiation hardening and embrittlement of structural materials. Of course, thermo-physical, corrosion, creep, fatigue, … and other properties are also important but these will not be considered in this report. As illustrated on Figure 2, the monitoring of radiation hardening is usually done by examining the yield strength change while radiation embrittlement is monitored by the ductile–to–brittle transition temperature (DBTT). These are the two main properties that are reported in literature to quantify irradiation hardening and embrittlement. It is important to comprehensively define these two parameters to be able to model them.

In practice, technological components are designed to operate under loading conditions where the applied/generated stresses are well below the yield strength of the material. Under irradiation, the yield strength of structural materials is changed. In most cases, irradiation results in an increase of the yield strength and therefore the stresses in the component remain in the elastic regime. However, in few cases, in particular at high temperatures, material softening, i.e. reduction of the yield strength, can also occur. It is essential to verify that this softening cannot induce dimensional instabilities that might affect the operation of the component.

The DBTT is a reference temperature that is used in structural calculations to provide a lower operating temperature limit of the components and materials. Above this temperature, the material behavior is essentially ductile and therefore any high local stresses can be accommodated by plastic deformation and therefore no unstable fracture would occur. On the other hand, below the DBTT, unstable brittle fracture is possible jeopardizing the safe operation of the component. In general, the materials are chosen such that their operating temperatures are well above the DBTT.

However, upon irradiation, the DBTT is raised and therefore the lower operation temperature limit is accordingly raised to higher temperatures. Therefore, it is extremely important to capture these effects in order to ensure that the component is operating at any time in the "authorized" safe temperature window. However, the DBTT, at least as currently determined in practice, is not an intrinsic physical material property characterizing fracture [33]. As clearly emphasized by Lucas et al. [34], there is no unique DBTT for a material. The limited applicability of the Charpy impact test was also pointed out in [35] but it is still used to monitor irradiation effects. More critical, under some circumstances that will be seen later, it might bias (underestimate) the actual embrittlement [36].

Another very important material property that is very useful to monitor irradiation effects is the fracture toughness. This is probably the best monitor that directly measures the resistance of a material against fracture. Figure 3 illustrates the irradiation effect on the fracture toughness evolution with temperature. As it can be seen, not only the transition curve is affected by irradiation by increasing the probability of brittle fracture but also the

ductile crack initiation toughness is substantially reduced in the ductile regime. Moreover, although not directly obvious from Figure 2, the tearing resistance is proportionally reduced as well. For example, around room temperature, Figure 3 indicates that while the unirradiated material has a high toughness (high resistance to brittle fracture, ~270 MPa√m), after irradiation it would fail at room temperature in a brittle manner already at very low loading levels (<40 MPa√m). Of course, from a design point of view, such a figure is extremely useful for structural integrity calculations. Unfortunately, at it will be seen later, the available experimental data are too scarce to be utilized in a modeling perspective. Moreover, modeling fracture requires first the modeling of deformation.

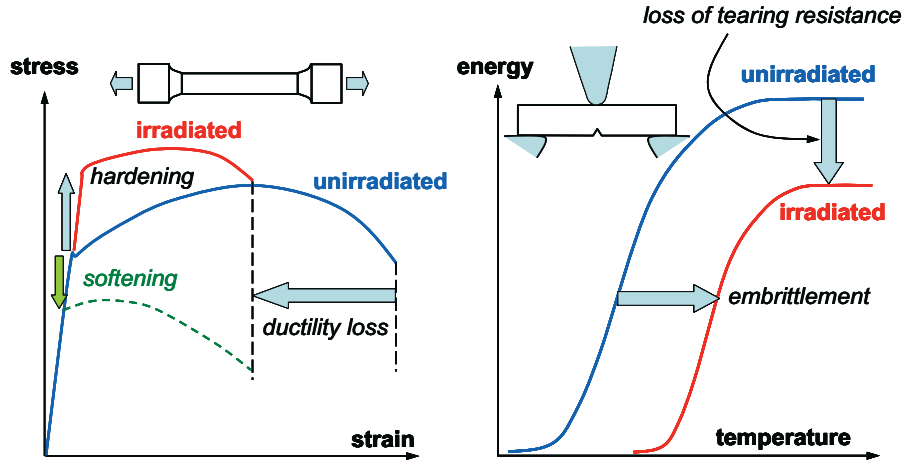

Figure 2. Monitoring irradiation hardening and embrittlement.

As reported by Odette [33], the fracture conditions can be correctly predicted by combining the relationships between:

1. the applied loading and the local crack tip stress/strain fields;
2. these stress/strain fields and the local damage evolution in the crack tip process zone; and
3. the critical damage condition leading to fracture.

The basic micro–mechanisms of the rupture process in the brittle fracture regime were given by Odette [33]. Basically, fracture occurs when the local stress exceeds a critical stress, the so–called microcleavage fracture stress, over a critical area ahead of the crack tip [37-41]. This description was originally developed for ferritic steels but the same approach can be applied to ferritic/martensitic steels [42-43]. The microcleavage fracture stress and the critical distance depend mainly on the prior austenite grain size, the lath packet size, and the size and number density of the carbides [42]. The microcleavage fracture is usually assumed to be temperature independent [44] and remains little affected by irradiation [45].

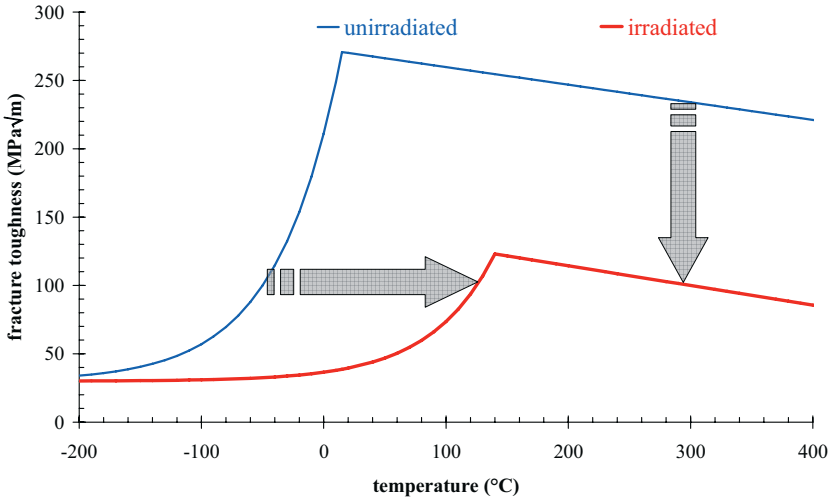

Figure 3. Effect of irradiation on the fracture toughness transition curve.

It is important to mention that the DBTT values that are reported in literature are questionable. Indeed, this temperature is arbitrarily defined at an energy level fixed to 50% of the upper shelf energy [46]. After irradiation, the upper shelf energy does not necessarily monitor the irradiation effects and might in some cases bias the DBTT value. It is not surprising to observe in some cases an increase of the upper shelf energy after irradiation [47]. At high dpa–levels, dislocation channel deformation tends to occur [20, 48-49]. This phenomenon results from the removal of defect clusters by dislocation motion and further provides the basis for an instability leading to a new mode of failure called channel fracture [49-51]. Under these circumstances, in the upper shelf temperature range, while static fracture toughness is significantly diminished, the dynamic fracture toughness remains unaffected by irradiation. Actually, the deformation mechanism is modified by the impact loading rate and therefore the DBTT when evaluated at 50% of the upper shelf energy will be incorrectly smaller. Therefore, the definition of the DBTT should be modified to avoid biasing this important parameter.

So, from a design point of view, the DBTT determined using Charpy impact tests is not directly exploitable. Actually, it has to be correlated to fracture toughness transition temperature. The latter provides a fracture toughness versus temperature curve that can be compared to the loading conditions and further used in structural integrity calculations to ensure that operation of the component is located in a safe temperature window. For instance, for reactor pressure vessel ferritic steels, it is well accepted that the shift of the Charpy impact transition temperature (ΔDBTT) is equal/proportional to the shift of the fracture toughness transition temperature ($\Delta T_{100MPa\sqrt{m}}$) [52-55]. However, this simple correlation cannot be extended to other materials or other experimental conditions.

There were many attempts to correlate hardening (yield strength increase) to embrittlement (DBTT–shift) but these simple one–to–one correlations are still a matter of debate. As it will be seen later, the hardening–to–embrittlement correlation in not linear.

The only appropriate property that can be modeled is the yield strength. Indeed, the main effect of irradiation is the creation of defects that will act as obstacles to dislocation motion. The dispersed barrier hardening theory, described in a number of reviews [16, 56-59], offers a frame in which hardening can be easily modeled. Hardening theory is well described. It is clear that hardening and embrittlement are intimately connected and therefore, it should be possible to relate them. In the following, it will be shown that such hardening–to–embrittlement correlation can be provided through the use of the load diagram approach.

2.2. On the correlation between hardening and embrittlement

From a modeling point of view, it is more practical to model the hardening than embrittlement. In most published literature, an empirical linear relationship is assumed between hardening and embrittlement [60-61] although some physically–based correlations were already proposed [62]. Rather than applying a proportionality factor between hardening ($\Delta\sigma_y$) and embrittlement (ΔDBTT), it is possible by analyzing the material flow and fracture properties in a physically–based frame such as the one offered by the load diagram (see next), to provide a more physical relationship between hardening and embrittlement. This way, even when non hardening embrittlement occurs, this phenomenon can be taken into account.

2.2.1. Load diagram

The load diagram requires instrumented Charpy impact tests in combination with tensile tests. Actually, instrumented impact test record offers an accurate description of the flow and fracture of the material. In Figure 4, the load–time test records of Charpy specimens tested at various temperatures are shown. These curves clearly show that the absorbed energy increases with test temperature. Up to the maximum load, the specimen continuously deforms with or without some ductile crack extension. The rapid load decrease is indicative of brittle fracture. In the transition region where both ductile crack extension and brittle fracture co–exist, as illustrated in Figure 5, it is possible to correlate the load–time test record to the observation of the fracture surface. Each part of the record can be associated with what occurs during the test. In particular, some characteristic loads can be used to consistently relate them to the fracture processes. Indeed, the characteristic loads:

F_{gy} : load at general yield
F_m : maximum load
F_u : unstable fracture load
F_a : arrest load

correspond to specific events on the fracture surface. Except the general yield load, all other loads are not physical but engineering parameters. Indeed, the general yield load can be associated with the dynamic yield strength of the material. However, to be directly

exploitable, it is necessary to transform the load into stress to be specimen configuration independent.

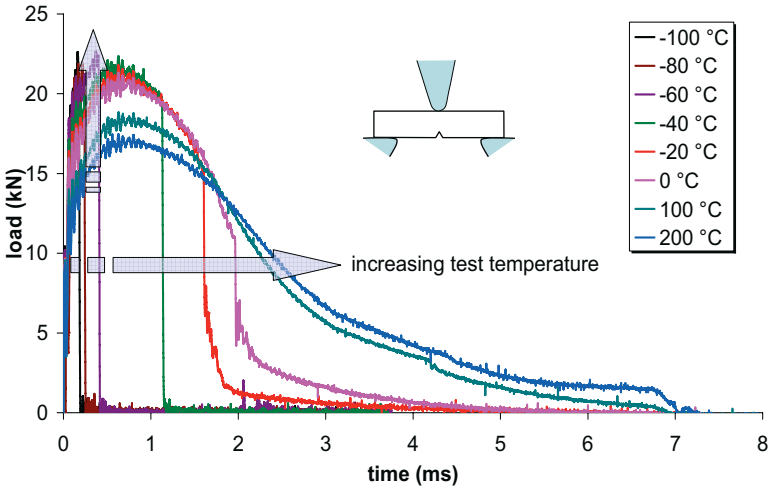

Figure 4. Charpy impact test records as a function of test temperature.

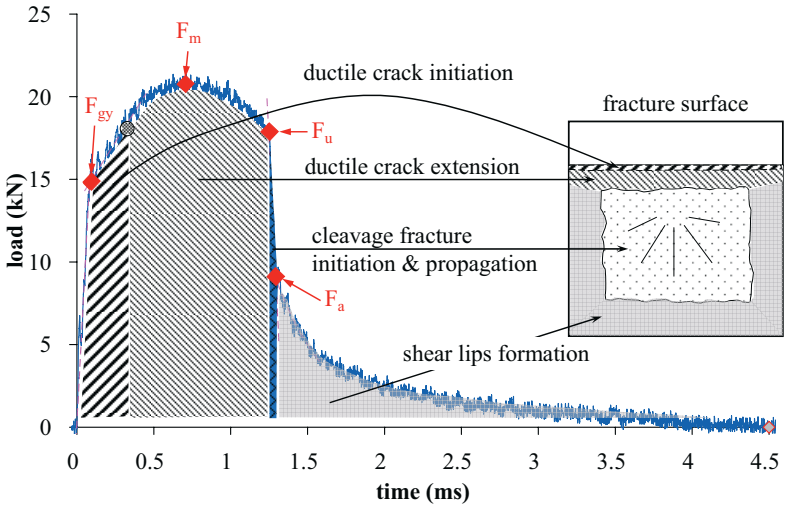

Figure 5. Charpy impact test record correlation to fracture surface.

It was shown in [63-64] that the stress during an impact test can easily be derived using the following relation:

$$\sigma = \frac{\beta\, S\, F}{2\, C_f\, (W-a)^2\, B} \quad (1)$$

where σ is the stress, S is the span (=40 mm), F is the load, W is the specimen width (=10 mm), B is the specimen thickness (=10 mm), a is the notch depth (=2 mm), C_f is the constraint factor which depends on the tup configuration: C_f=1.274 for ISO tup and C_f=1.363 for ASTM tup [64], β is a constant depending on the yielding criterion: β=2 for Tresca and β=√3 for von Mises criterion. Actually, an intermediate criterion between Tresca and von Mises ($\beta_{average}$=1.866) gives the best agreement [65]. As a result, in the case of a Charpy test with an ISO tup, the following conversion formula can be applied:

$$\sigma(MPa) = \chi \times F(kN) \quad (2)$$

where χ=45.8 for standard Charpy impact tests with an ISO tup. In the case of sub–sized Charpy impact tests of KLST–type, $\chi \approx 597.5$. Application to a typical 9%Cr–steel, Eurofer–97, is shown in Figure 6 where a good agreement is observed between standard Charpy impact tests (CVN) and sub–sized Charpy impact tests (KLST).

It was shown in [66] that during the Charpy impact test, the corresponding effective strain rate is about 10 s^{-1}. Figure 6 shows indeed a good agreement between tensile data tested at dynamic loading rate (10 s^{-1}) and the general yield strength value derived from both standard and sub–sized Charpy impact tests. Of course, locally, the strain rate may reach 10^3 s^{-1} but when integrated over a representative volume of material where deformation occurs, the equivalent strain rate is ~10 s^{-1} as experimentally verified in [66]. Note that other stresses (σ_m, σ_u and σ_a) are dependent on the initial ligament and do not have a physical significance as the general yield stress (σ_{gy}).

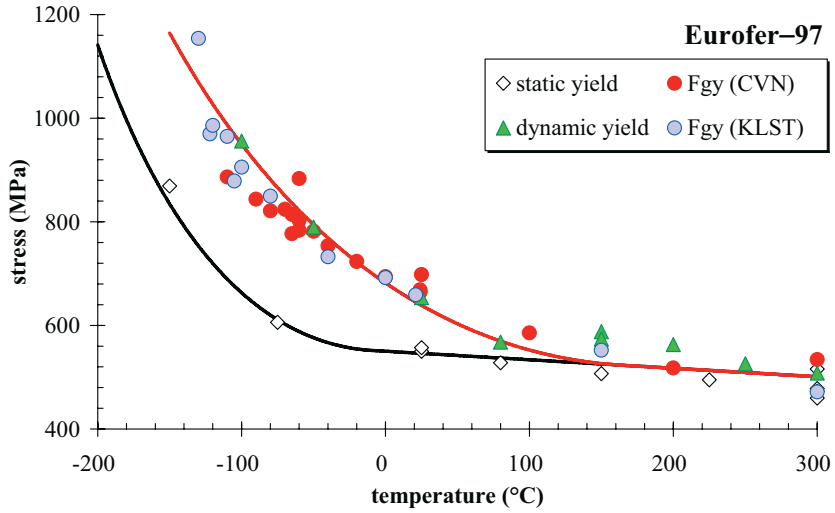

Figure 6. Both standard (CVN) and sub–sized (KLST) Charpy impact specimens provide a unique general yield strength – temperature dependence. Static ($\dot{\varepsilon} \approx 1\ 10^{-4}\ s^{-1}$) and dynamic tensile tests ($\dot{\varepsilon} \approx 10\ s^{-1}$) are also included for comparison.

It is known that material deformation occurs according to a thermally–activated slip process [67-73]. Basically, the yield strength can be represented by the sum of two components:

1. the athermal stress, σ_{ath}, accounts for the interaction between dislocations with long range obstacles (precipitates, grain boundaries, ...);
2. the thermally activated stress, σ_{th}, accounts for short range obstacles (<10 atom diameters) to dislocation motion. These short-range barriers include the Peierls-Nabarro stresses and dislocation forests.

The yield strength as a function of strain rate ($\dot{\varepsilon}$) and temperature (T) can be described by the following equation [64]:

$$\sigma(\dot{\varepsilon},T) = \sigma_P\left(1-\alpha T\right)\left[1-\left(\frac{k\,T\,Ln\left(\dot{\varepsilon}_0/\dot{\varepsilon}\right)}{H_c}\right)^{1/m'}\right]^{m} + \sigma_{ath}\left(1-\alpha T\right) \qquad (3)$$

where H_c is the activation energy (enthalpy) of a given barrier, σ_P is the so–called effective Peierls stress, $\dot{\varepsilon}_0$ is the intrinsic strain rate sensitivity of the material, m and m' are constants that describe the lattice energy barrier, k is the Boltzmann constant and the constant α is the coefficient of temperature dependence of the Young's modulus ($\alpha \approx 2.67\ 10^{-4}\ K^{-1}$)[†]. This yield strength model is also called double kink nucleation model [74]. Note that other formulations than equation (3) could also be used without any difficulty as far as they represent the experimental data.

[†] Within the temperature range under consideration, the temperature dependence of the Young modulus is assumed to be linear.

Once the stresses are calculated, a diagram can be constructed which combines the static tensile and the Charpy impact characteristic stresses of the material under consideration. A typical example is shown in Figure 7 for a 9%Cr–steel. The static and dynamic yield stress curves shown in Figure 7 are obtained using equation (3) while other curves are fitted to experimental data with engineering constrained models [66]. As it can be seen, only one parameter set allows to consistently represent the data shown in Figure 7. The shear fracture appearance SFA–curve model (bottom Figure) is essentially based on the load diagram (top Figure).

The load diagram approach rationalizes the instrumented Charpy impact and static tensile data into a unique description of the material including the strain rate effects on the flow properties and fracture behavior. More details on the load diagram can be found in [66].

Two important characteristic temperatures, namely T_I and T_O, can be derived from the load diagram. T_I is the brittle temperature and is defined as the temperature at which fracture occurs in a fully brittle manner, corresponding to a shear fracture appearance SFA = 0%. At T_I, fracture occurs at the general yield stress, σ_{gy}. At and above T_O, fracture is fully ductile (SFA = 100%).

The transition temperature, T_I offers a better alternative to the DBTT parameter that is usually defined at 50% of the upper shelf energy. As it will be seen later, the use of T_I to characterize the DBTT reduces the probability to bias the actual shift of the transition temperature.

The instrumented Charpy impact test allows also deriving the so–called microcleavage fracture stress. This critical stress is assumed to be insensitive to test temperature and strain rate [38-40, 75] if the cleavage mechanism occurs by slip (in contrast to twin–initiated cleavage). The values that were obtained on 9% Cr – steels range between 2100–2400 MPa [75-76], in the same order of magnitude of ferritic steels [66]. It is also very often assumed to be unaffected or very little affected by irradiation [44] but its reduction or increase were sometimes reported in literature. Tanigawa et al [77-78] reported a significant increase of the microcleavage fracture stress for three 9%Cr – steels (F82H, JLF-1 and ORNL-9Cr) as a result of precipitate size change and amorphization. However, the method that was used for σ_c–determination is questionable. Henry et al. [79] reported a decrease of the microcleavage fracture stress in the He–implanted zone of a three point bend specimen. However, the method that was used is also questionable; in particular their Figure 3 is not consistent as the pop–in load corresponds to a stress well below the yield strength.

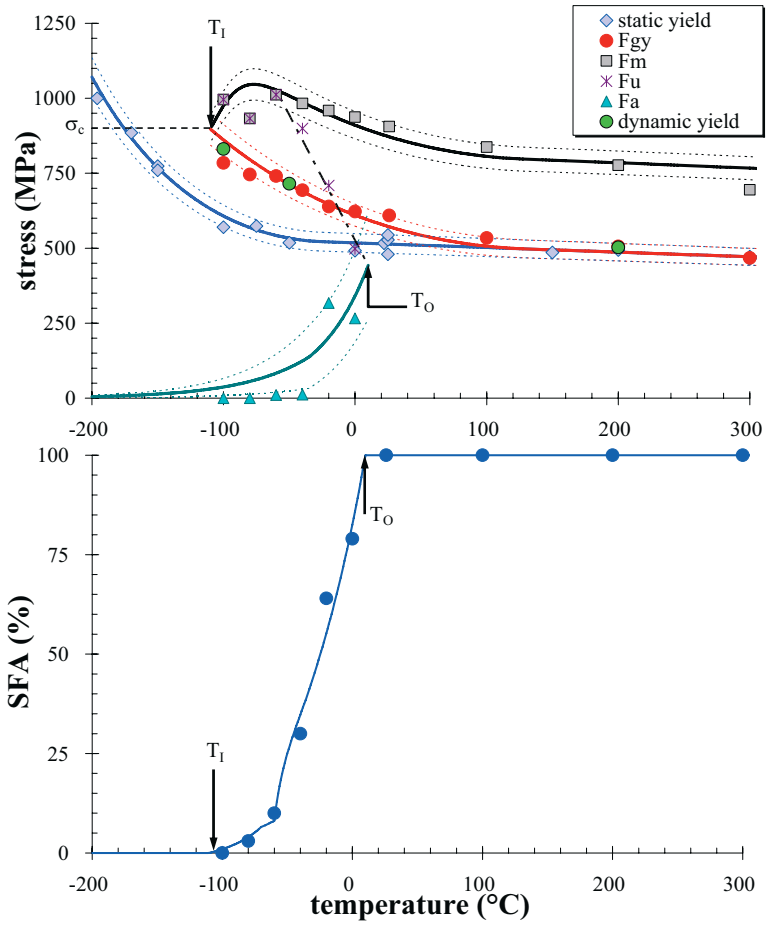

Figure 7. Load diagram of Eorofer–97: stress–temperature and SFA correlation.

2.2.2. Irradiation effect on the load diagram

It is generally well established that irradiation hardening affects primarily the athermal component of the yield strength [68-69, 73, 80]. This means that the shape of the temperature dependence of the yield strength is not modified by irradiation. It should be emphasized that all the parameters of the model except the athermal yield strength remain unchanged by irradiation. This means that the load diagram in any irradiated condition can be obtained from the unirradiated condition by modifying only the athermal yield strength. This simple description of irradiation effects is not fully true. Indeed, in such a case, the microcleavage fracture stress, also called critical stress, is implicitly assumed to be constant [60]. A slight decrease of this critical stress with temperature is sometimes reported [81]. It is usually accepted that cleavage fracture initiation is associated with the

achievement of this stress over a critical distance [37, 82]. However, the microcleavage fracture stress can be affected as well by irradiation, for instance in two specific cases, under segregation of impurities or under He–bubbles diffusion to grain boundaries and that can modify the fracture mode from transgranular to intergranular fracture [83-85]. So, the grain boundary weakening, without affecting the material hardening can enter into play.

The microcleavage fracture stress, σ_c, can also be estimated from the load diagram. It is equal to the dynamic yield strength at T_I (brittle fracture temperature corresponding to 0%–SFA) times the stress concentration factor, C_{sf}:

$$\sigma_c = C_{sf} \times \sigma(T_I) \tag{4}$$

where $C_{sf} \approx 2.35$.

This stress is usually assumed to be temperature and irradiation independent [44, 45]. Tanigawa and co-workers reported a significant increase of the microcleavage fracture stress upon irradiation of 9%Cr–steels [77-78]. However, the procedure they used to estimate the microcleavage fracture stress is doubtful because of the DBTT definition and the stress concentration factor that was used. However, an increase of the σ_c is not excluded but the magnitude should be very small. Nevertheless, experimental data are required to better quantify, if any, the change of microcleavage fracture stress. However, in presence of intergranular fracture, the microcleavage fracture stress can be lowered without hardening change leading to the so–called non–hardening embrittlement. As a result, the hardening–to–embrittlement relationship is essentially governed by two parameters, the athermal yield strength increase and the eventual change of microcleavage fracture stress. Because the cleavage fracture stress is proportional to the stress at T_I, the latter will be considered to determine the induced embrittlement.

At T_I, the yield strength is equal to:

$$\sigma(\dot{\varepsilon}, T_I^0) = \sigma_P \left(1 - \alpha T_I^0\right)\left[1 - \left(\frac{k T_I^0 \, Ln\left(\dot{\varepsilon}_0 / \dot{\varepsilon}\right)}{H_c}\right)^{1/m'}\right]^m + \sigma_{ath}\left(1 - \alpha T_I^0\right) \tag{5}$$

After irradiation, equation (5) becomes:

$$\sigma(\dot{\varepsilon}, T_I^{irrad}) = \sigma_P \left(1 - \alpha T_I^{irrad}\right)\left[1 - \left(\frac{k T_I^{irrad} \, Ln\left(\dot{\varepsilon}_0 / \dot{\varepsilon}\right)}{H_c}\right)^{1/m'}\right]^m + \left(\sigma_{ath} + \Delta\sigma_{irrad}\right)\left(1 - \alpha T_I^{irrad}\right) \tag{6}$$

Assuming that other material parameters such as σ_P and H_c, … are not changed by irradiation (only the athermal part is elevated), the relation between $\Delta T_I = T_I^{irrad} - T_I^0$ and $\Delta\sigma_{irrad}$ is non linear requiring a numerical solution. Note that the procedure described above is similar to the one described by Wullaert et al. [45].

In the following, first, the relation between hardening and embrittlement without change of the microcleavage fracture stress is considered. Figure 8 illustrates the effect of irradiation on the load diagram. As it can be seen, the increase of the athermal yield strength component assuming a constant microcleavage fracture stress lead to an increase of the transition temperature, T_I. A similar load diagram with the same athermal yield strength increase but allowing for a reduction of the microcleavage fracture stress is shown in Figure 9, resulting in an additional non–hardening transition temperature increase, ΔT_{NHE}. [82, 86]. Such non–hardening embrittlement can occur as a result of enhanced radiation–induced segregation of impurity elements to grain boundaries or radiation enhanced helium diffusion and accumulation to grain boundaries [84].

Unfortunately, experimental data on the alteration of the microcleavage fracture stress by irradiation or where irradiation changed the fracture mode are very scarce.

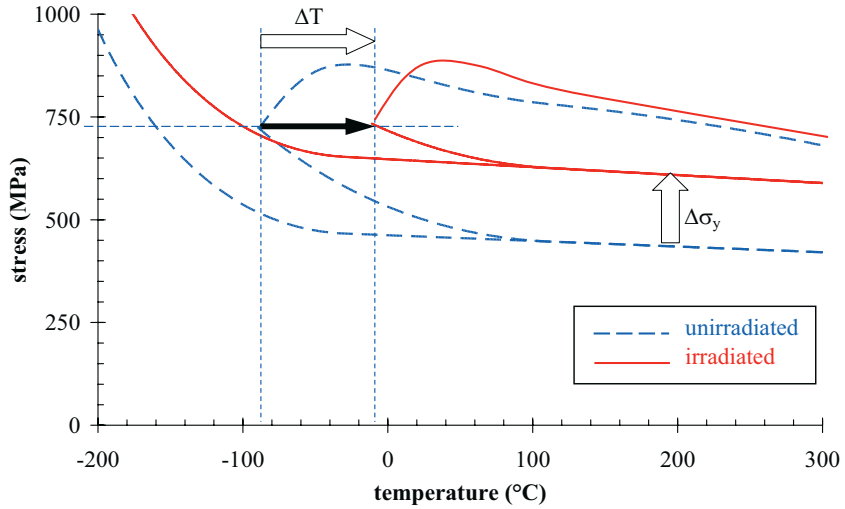

Figure 8. Relation between hardening and embrittlement in absence of non hardening embrittlement.

As it can be seen, the microcleavage fracture stress plays an important role to determine the relationship between hardening and embrittlement. Unfortunately, there are very few experimental data on its dependence on temperature and irradiation. The microcleavage fracture stress is often reported to slightly decrease with test temperature [87]. A decrease of the microcleavage fracture stress was suggested by a number of investigators to explain excessive embrittlement with regard to hardening, see for example [87-88].

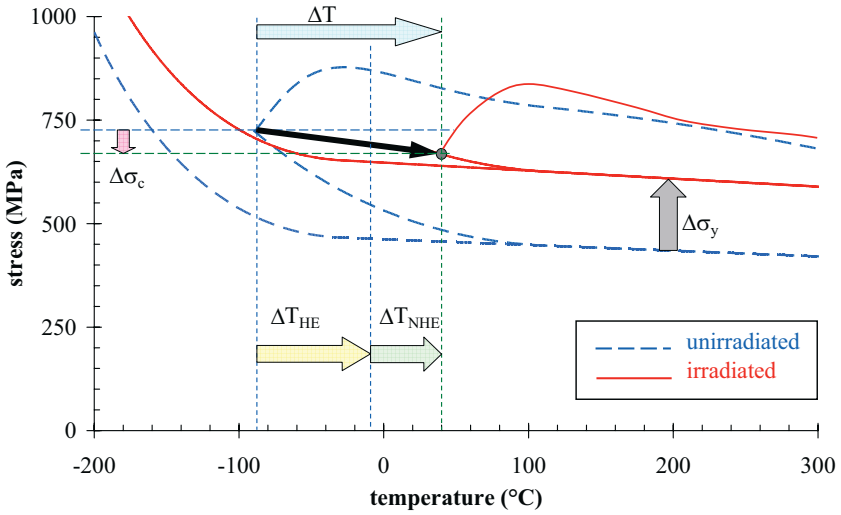

Figure 9. Relation between hardening and embrittlement in presence of non hardening embrittlement.

Assuming the general case of invariable microcleavage fracture stress, it is possible to estimate the relationship between the yield strength increase, $\Delta\sigma_{ath}$, and the transition temperature increase, ΔT_I. This relation is shown in Figure 10 indicating clearly the non–linear character of this correlation. At low neutron dose levels corresponding to yield strength changes below about 250 to 300 MPa, there is a quasi–linear relationship between hardening and embrittlement with a slope of about 1/3 °C/MPa. However, above 300 MPa of hardening, the slope continuously increases and can exceed 1 °C/MPa above about 450 MPa–hardening. This Figure clearly shows that simple linear correlation between hardening and embrittlement valid at low dose levels might be very unconservative at higher dpa levels.

It is important to emphasize that the relation between DBTT–change, yield strength change and microcleavage fracture stress is not that easy and will depend on a number of other parameters. An illustration can be found in [87] where for the same yield strength increase and the same microcleavage fracture stress, the change of DBTT can still be different. This would mean that the strain rate sensitivity or/and the activation enthalpy are drastically affected by irradiation. However, this requires a full characterization of the tensile and Charpy impact properties, which is usually not available.

It is clear that the correlation between hardening and embrittlement is not fully understood because of the DBTT definition, such as the data reported in [81, 89]. For example, a 9Cr-2WVTa steel irradiated at 365°C up to 7 dpa leads to a large increase of the yield strength ($\Delta\sigma_y$=125 MPa) and a negligible embrittlement (ΔDBTT=4°C) which obviously is strange. At a higher dose level, 14 dpa, the 9Cr-2WV exhibits a DBTT shift and a yield strength increase respectively of 29°C and 141 MPa in comparison to 15°C

and 147 MPa for the 9Cr-2WVTa [81]. Moreover, this abnormal behavior is not confirmed by the data obtained at a higher irradiation temperature (393°C) [32, 90]. There is clearly an inconsistency between these two data series. Other indications also support the bias introduced by the DBTT definition, as can be seen from the shape of the transition curves shown in [88, 91-92].

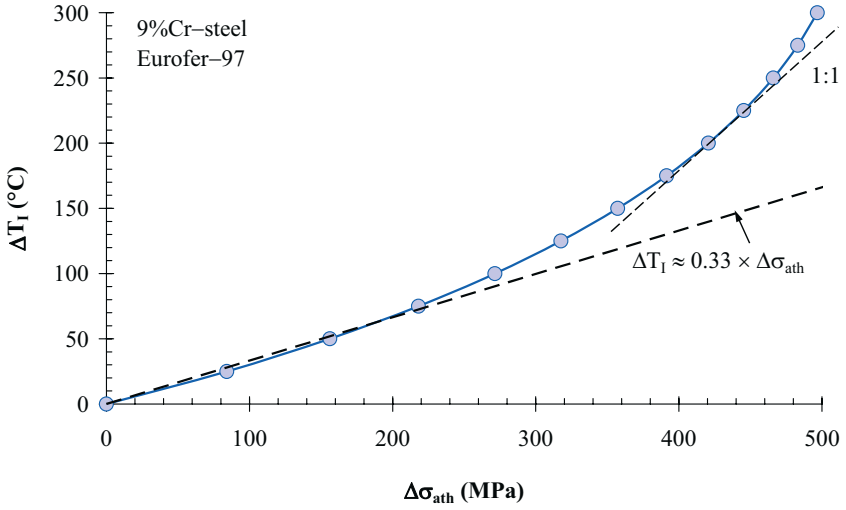

Figure 10. Correlation between hardening ($\Delta\sigma_{ath}$) and embrittlement (ΔT_I).

Finally, a good and full characterization of the material in the unirradiated condition is essential to derive the effect of irradiation on the deformation and fracture properties. In the irradiated condition, very limited and appropriately selected tests would be sufficient to build diagrams such as those shown in Figure 8. Of course, some validation of the procedure in few conditions is necessary but systematic characterization of irradiated materials including tensile, Charpy impact and fracture toughness tests are not required at each dose level. However, when change of fracture mode is suspected, it is important to evaluate the change of the microcleavage fracture stress to account for the additional non–hardening embrittlement. Simple tensile tests on notched bars associated with detailed finite element calculations and scanning electron microscopy observations can be used to determine the microcleavage fracture stress when required.

2.2.3. Load diagram application

It is essential to understand the importance of the general property–to–property correlation concept and the particular case of the load diagram. It was already mentioned that one of the parameters used to monitor irradiation effects is the DBTT. This DBTT is conventionally defined as the temperature at which the absorbed energy is half the upper shelf energy. In a recent investigation, it was experimentally demonstrated that the upon irradiation of Eurofer-97 at 300°C, the DBTT–change is found systematically and

significantly lower than the shift of the fracture toughness transition curve, $\Delta T_{100MPa\sqrt{m}}$ [36]. Moreover, the upper shelf energy level is not or very little affected by irradiation while crack resistance measurements indicated a drastic loss of initiation toughness and tearing resistance. On the other hand, the load diagram indicated a shift of the temperature T_I that is in agreement with the shift of the fracture toughness transition curve. This was attributed to the dislocation channel deformation phenomenon that is different when the specimen is loaded at dynamic loading rates [93]. Therefore, most of DBTT values reported in literature should be considered with care. On the other hand, the correlation between the temperature T_I and $T_{100MPa\sqrt{m}}$ is more consistent (see Figure 11) [36]. Actually, it is the ductile fracture component that affects the DBTT–value and therefore an alternative way is to reduce the energy level at which the DBTT is evaluated to a level where the fracture is typically brittle. Also, experimental data, where the upper shelf level is not affected by irradiation or even increases after irradiation, do not indicate that a significant decrease of upper shelf toughness and tearing resistance is possible at static loading rate. This was confirmed by crack resistance tests performed at dynamic (impact) loading rate exhibiting no or negligible effect of irradiation (see Figure 12) [93]. On the other hand, crack resistance tests performed at static loading rate show a drastic effect of irradiation (see Figure 13). This clearly shows that a negligibly small effect on Charpy impact upper shelf does not necessarily mean that static initiation and tearing resistance would behave similarily. [93]. Close examination of the Charpy impact test records at upper shelf temperatures of unirradiated and irradiated samples shows that both load–time traces are very similar (identical) except in the very early (<1ms) phase of the deformation process (see Figure 14) [93]. Actually, the material ahead of the notch is modified (annealed) by the deformation process during this 1ms–phase and the irradiated material cannot be distinguished from the unirradiated material above 1 ms.

These few examples clearly show the importance of considering different material properties and analyzing the experimental data in a consistent manner to help understanding the underlying physical mechanisms.

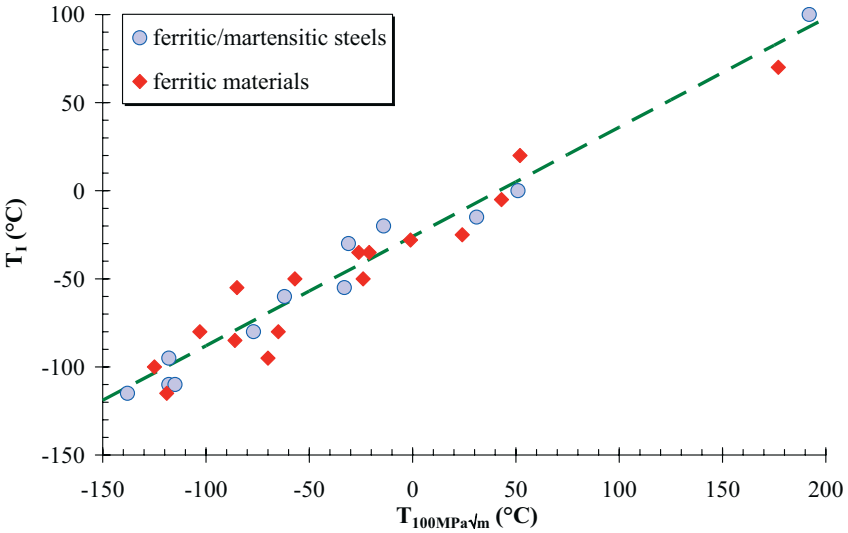

Figure 11. On the correlation between T_I and $T_{100MPa\sqrt{m}}$.

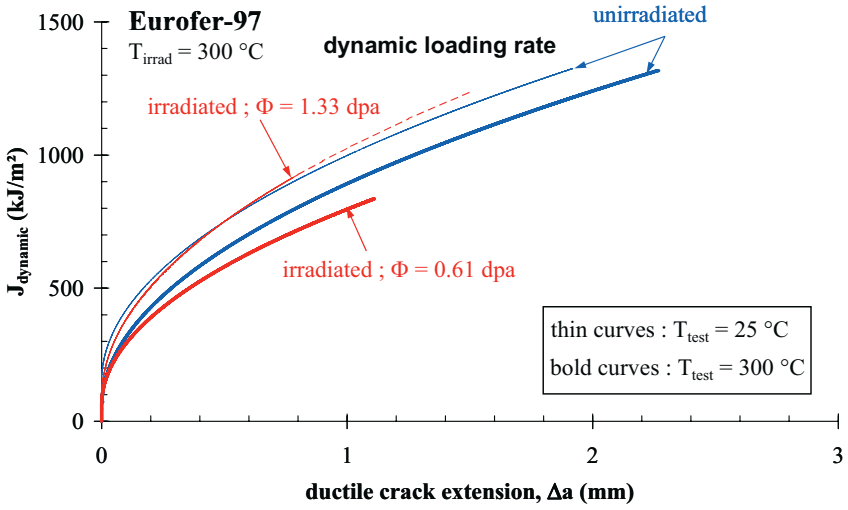

Figure 12. Negligible effect of irradiation on the crack resistance curve at dynamic (impact) loading rate.

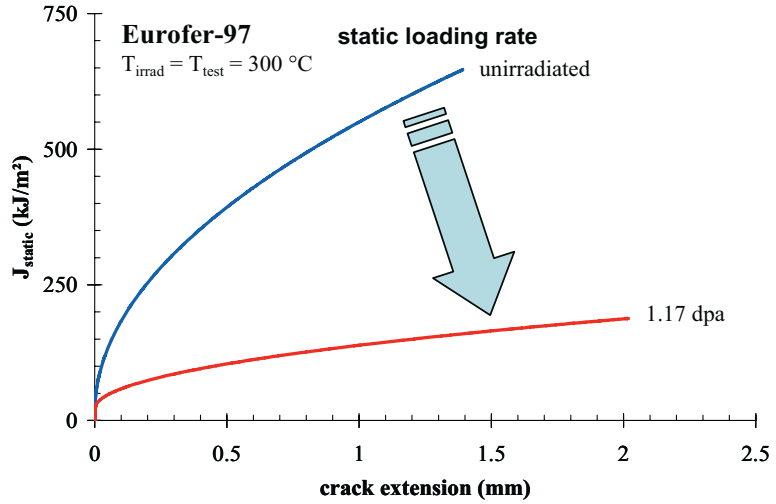

Figure 13. Significant effect of irradiation on the crack resistance curve at static loading rate.

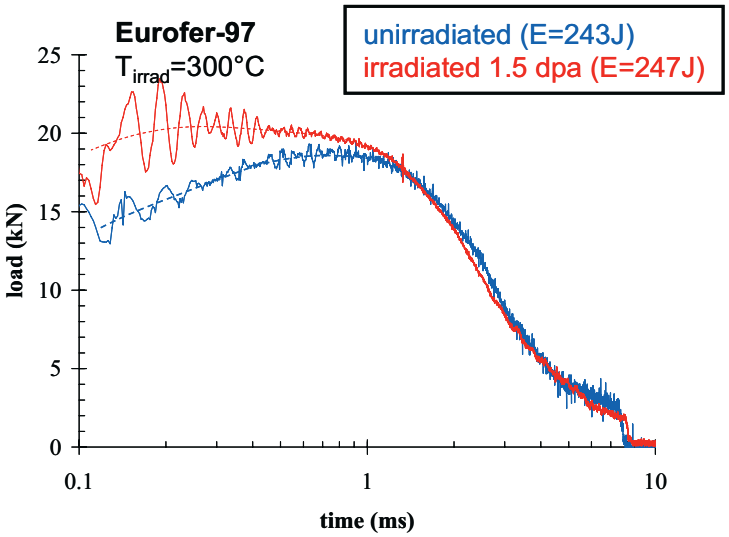

Figure 14. After about 1 ms, no difference can be depicted between the unirradiated and irradiated test records.

2.3. Conclusion

The limitations of the conventional DBTT based on Charpy impact tests were clearly established in particular when plastic instability (plastic flow localization) due to dislocation channel deformation occurs.

It was shown that the load diagram approach offers a frame in which an increase of the yield strength can be correlated to the change of the DBTT as measured by T_I. The most important aspect is that the material should be well characterized in the unirradiated condition (tensile, Charpy impact, fracture toughness). In the irradiated condition, only tensile data are required if the microcleavage fracture stress is not affected by irradiation. Otherwise, the microcleavage fracture stress should be determined by combining tests with a notched geometry, scanning electron microscopy (SEM) examination and finite element calculations.

III. RADIATION EFFECTS ON 9%CR–STEELS

3.1. Introduction

Under neutron bombardment, the physical and mechanical properties of fusion reactor components will be altered. The nature and amplitude of the changes of the mechanical properties will depend on a number of parameters, including irradiation temperature and neutron dose. More details on the interaction of neutrons with solids can be found in [94-97]. In general, any radiation damage model should rely on the microstructural changes resulting form these atomic–scale interactions and their consequences on the mechanical properties. For many metals, one can distinguish two types of defects that are created in the atom lattice: the neutron–induced point defects and the transmutation products. Point defects are created when impinging neutrons knock atoms from their lattice sites via elastic or inelastic collisions. Elastic collisions occur in such a way that a part of the kinetic energy of the neutrons is transmitted to atoms. Inelastic collisions involve neutron absorption and subsequent emission of a γ–, α– or p–particle. The recoiled atoms are forced into interstitial positions, the so–called self–interstitial atoms (SIA), leaving empty lattice sites, the so–called vacancies. Of course, irradiation temperature plays an important role in the evolution of these point defects (SIA's and vacancies) and the resulting microstructure. For the transmutation elements, hydrogen (H) and helium (He) are usually generated by fast neutrons following (n,p)– and (n,α)– reactions. Because of their low solubility in metals, such gases have a detrimental effect on the mechanical properties of metals.

It is also generally accepted that the irradiation–induced defects act as obstacles to dislocation motion increasing thereby the yield strength. Most of the models that were developed to account for radiation hardening are based on the interaction of a moving dislocation with these defects [12, 17, 18, 97]. As a consequence, the plastic flow to dissipate the available energy for cracking is also reduced leading to the so–called irradiation embrittlement of the material. However, this simple description should be moderated. Indeed, softening rather than hardening can also occur after irradiation [31, 98-100]. Moreover, the deformation and fracture mechanisms can also be modified by irradiation (dislocation channel deformation, intergranular fracture). All these effects should be captured by the model but in the present work, focus is put on irradiation hardening as most of the available data exhibit such a behavior.

A list of possible mechanisms involved in the irradiation–induced changes in the microstructure of many structural materials was given in [12-13]. Although qualitatively known, it is still very difficult to quantitatively estimate the contribution of each of these mechanisms to radiation damage. Nevertheless, in practice, only the major mechanisms are considered and these are often simplified to be applied in an engineering perspective.

Temperature is an important parameter in radiation damage evolution and three main temperature regions can be distinguished [1]:

- At low temperature: radiation hardening occurs already at low dpa with a decreasing rate above a certain dose level. Most of the defects are related to point

defect generated during the collision cascades. Because of the low temperature, there is insufficient thermal energy to drastically modify the defects evolution.
- In the intermediate temperature region, the thermal activation energy promotes the agglomeration of single defects, and consequently voids and planar defect clusters can form, resulting in swelling and enhanced irradiation creep.
- Finally, in the high temperature regime, embrittlement can be associated with the formation of helium bubbles at grain boundaries.

The mechanical properties of 9%Cr–steels provide important data input for structural integrity calculations. These properties are directly related to their microstructure which undergoes modifications under service. It is therefore important to characterize these materials before and after irradiation, in particular with special attention to the microstructure and its stability with respect to irradiation and thermal aging. A complete description of microstructural evolution under irradiation is out of the scope of this report; a number of very interesting papers were written on the subject [6, 101]. Here, only a brief description will be given together with some specific aspects related to 9%Cr–steels.

3.2. Materials: 9%Cr–ferritic/martensitic steels

The 9%Cr–steels were initially developed for application in the petrochemical and chemical industries and power generation plants, in particular gas turbines and boilers. This choice was motivated by their good mechanical properties such as high strength and creep–rupture properties. In the nuclear field, ferritic/martensitic steels of the Fe–9–12% CrMoV(Nb) type have mainly been used as wrapper and in few cases as cladding materials in fast breeder reactor fuel elements in the temperature range of 360–550 and 600°C, respectively [1, 19, 102-109]. In the last decade, these steels gained interest for application not only in fusion technology but also in advanced nuclear systems such as generation-IV (GEN-IV) fission reactors, spallation sources and accelerator–driven systems (ADS) [104, 110-118]. As a result, extensive R&D was worldwide directed towards the behavior of these steels under irradiation. The environmental conditions differ from one system to another but helium production is significant [119]. The selection for ferritic/martensitic steels is based on their good thermo–physical and mechanical properties, good compatibility with major cooling/breeding materials in the foreseen temperature window of application and low sensitivity to swelling and He–induced high–temperature embrittlement. Since the mid–80's, the R&D activities were gradually redirected from the optimization of conventional alloys to reduced activation heats. The reduction of activation was reached by substituting Mo by W while Nb is replaced by V and Ta [102, 120-125]. These activities were performed in close collaboration within a consortium including Europe, Japan and the USA under the IEA–implementing Agreement on Research and Development of Fusion Reactor Materials [1, 120, 126-128].

In particular, EUROFER (a 9%Cr-1WVTa steel) in Europe [3, 129-141], F82H (8%Cr-2WVTa steel) in Japan [78, 127, 134, 141-155] and various 9-12%Cr–steels in the US [32, 35, 83, 87-88, 91-92, 125, 149, 156-163] were extensively characterized with respect

to their irradiation behavior. One of the major critical issues of these materials is their irradiation embrittlement in the low temperature range [1]. An additional critical issue that it is difficult to assess is the synergetic effect of displacement damage and helium [164]. Table 1 summarizes a number of 9%Cr–steels that were examined in literature.

Table 1. Summary of the various 9%Cr–steels found in literature.

materials	B	C	N	Al	Si	P	S	Ti	V	Cr	Mn	Co	Ni	Cu	Nb	Mo	Ta	W	heat treatment	reference
Eurofer-97 (9Cr-1WVTa)		0.11	0.03			0.005			0.2	9	0.48		0.021		0.0017		0.07	1.1	980°C/30min + 750°C/1.5h	165
9Cr-1MoVNb		0.09	0.05	0.013	0.08	0.008	0.004	0.002	0.209	8.62	0.36	0.013	0.11	0.03	0.063	0.98		0.01	1050°C/30min + 700°C/5h	156
JFMS (9.5Cr-2MoVNb)		0.05			0.67	0.009	0.006		0.12	9.58	0.58		0.94		0.06	2.31			1050°C/30min + 775°C/6h	166
Eurofer-97 (9Cr-1WVTa)		0.11	0.03			0.005			0.2	9	0.48		0.021		0.0017		0.07	1.1	980°C/30min + 750°C/1.5h	167
F82H (8Cr-2WVTa)	0.0002	0.09	0.007	0.001	0.07	0.003	0.001	0.004	0.19	7.82	0.1		0.02	0.01	0.0002		0.04	1.98	1040°/30min + 750°C/1h	148
9Cr-1MoVNb		0.09		0.013	0.08	0.008	0.004	0.002	0.209	8.62	0.36	0.013	0.11	0.03	0.063	0.98		0.01	1040°C/1h + 760°C/1h	112
9Cr-2WV		0.12		0.018	0.23	0.014	0.007	0.01	0.24	8.95	0.51	0.012	0.01	0.03	0.01	0.01		2.01		
9Cr-2WVTa		0.11		0.017	0.21	0.015	0.008	0.01	0.23	8.9	0.44	0.012	0.01	0.03	0.01	0.01	0.06	2.01		
F82H (8Cr-2WVTa - IEA heat)	0.0002	0.09	0.006	0.003	0.11	0.002	0.002		0.16	7.71	0.16						0.02	1.95	1040°C/38min + 750°C/1h	20
EM10 (9Cr-1Mo)		0.096	0.024		0.37	0.015				8.8	0.51		0.18			1.09			980°C/30min + 750°C/30min	113
EM10 (9Cr-1Mo)		0.096	0.024		0.37	0.015				8.8	0.51		0.18			1.09			970°C/15min + 750°C/30min	168
T91 (9Cr-1MoVNb)		0.105	0.0055		0.43	0.009			0.2	8.26	0.38		0.13		0.075	0.95			1050°C/1h + 760°C/1h	
F82H (8Cr-2WVTa - IEA heat)		0.11	0.008					0.01	0.16	7.7							0.02	2	1040°C/40min + 750°C/1h	149
F82H (HT#2)		0.11	0.008					0.01	0.16	7.7							0.02	2	+ 920°C/1h + 750°C/1h	
9Cr-2WVTa		0.1	0.023					0.01	0.18	8.8							0.065	1.97	1050°C/1h + 750°C/1h	
JLF-1 (8Cr-2WVTa)		0.1	0.0215					0.002	0.2	8.9							0.09	1.95	1050°C/1h + 780°C/1h	
9Cr-2WVTa		0.11	0.021		0.21				0.23	8.9	0.44		0.01		0.01	0.01	0.06	2.01	1050°C/30min + 750°C/1h	116
0.1C-9Cr-1W-V, B,Ta	0.006	0.1			0.15	0.012	0.003		0.29	9.2	0.24						0.1	1.2	1050°C/5min + 790°C/1h	169
9Cr-2WVTa		0.11	0.021		0.21				0.23	8.9	0.44		0.01		0.01	0.01	0.06	2.01	1050°C/30min + 750°C/1h	170
mod 9Cr-1Mo (8Cr-1MoVNb)		0.092	0.055		0.15				0.2	8.32	0.48		0.09		0.06	0.86			1050°C/30min + 760°C/1h	
mod 9Cr-1Mo (9Cr-1MoVNb)		0.089	0.035	0.002	0.28	0.021	0.006	0.002	0.21	9.24	0.47	0.019	0.16	0.08	0.054	0.96			1038°C/1h + 760°C/1h	158
OPTIFER IV (8.5Cr-1WVTa)	0.003	0.11	0.06			0.004	0.004	0.02	0.23	8.5	0.6						0.15	1.16	1000°C/30min + 730°C/2h	171
GA3X (9Cr-2WVTa)		0.159	0.0018	0.015				0.001	0.214	9.17	0.042	0.003	0.021	0.0017	0.011	0.0077	0.011	2.12	1000°C/1h + 700°C/2h	
OPTIMAR (10.5Cr-1MoVNb)	0.0072	0.11	0.033	0.014	0.31	0.004	0.003		0.21	10.5	1.22	0.003	0.6		0.21	0.63			960°C/2h + 1075°C/30min + 700°C/2h	
OPTIFIER Ia (9Cr-1WVTa)	0.006	0.1	0.015	0.008	0.06	0.0047	0.005	0.007	0.26	9.3	0.5		0.005	0.035	0.009	0.005	0.066	0.965	1075°C/30min + 780°C/2h	
F82H (8Cr-2WVTa)	0.003	0.092	0.0027	0.01	0.091	0.0031	0.0031	0.0104	0.189	7.73	0.083	0.0024	0.032	0.0059	0.0057	0.0053	0.018	2.06	1040°C/30min + 750°C/2h	
ORNL 3971 (9Cr-2WVTa)	0.001	0.11	0.0215	0.017	0.21	0.015	0.008	0.01	0.23	8.9	0.44	0.012	0.01	0.03		0.01	0.06	2.01	1050°C/30min + 750°C/1h	

materials	B	C	N	Al	Si	P	S	Ti	V	Cr	Mn	Co	Ni	Cu	Nb	Mo	Ta	W	heat treatment	reference
MANET-I	0.0085	0.14	0.02	0.054	0.37	0.005	0.004		0.2	10.8	0.76	0.01	0.92	0.015	0.16	0.77			980°C/2h + 1075°C/30min + 750°C/2h	172 – 173
MANET-II	0.007	0.1	0.023	<0.02	0.14	<0.006	<0.007		0.22	9.94	0.79	<0.02	0.66	<0.01	0.14	0.59			965°C/2h + 1075°C/30min + 750°C/2h	
OPTIFER-Ia	0.006	0.1	0.015	0.008	0.06	0.0047	0.005	0.007	0.26	9.3	0.5		0.005	0.035	0.009	0.005	0.066	0.965	1075°C/30min + 780°C/2h	
OPTIFER-II	0.006	0.125	0.016	0.008	0.038	0.004	0.002	0.007	0.28	9.43	0.5		0.005	0.007	0.009	0.005	0.02	0.005	950°C/2h + 780°C/2h	
F82H	0.003	0.092	0.0027	0.01	0.09	0.003	0.003	0.0104	0.189	7.73	0.083	0.0024	0.032	0.0059	0.0057	0.0053	0.018	2.06	1040°C/30min + 750°C/2h	
ORNL	<0.001	0.11	0.0215	0.017	0.21	0.015	0.008	<0.01	0.23	8.9	0.44	0.012	<0.01	0.03		0.01	0.06	2.01	1050°C/30min + 750°C/1h	
OPTIFER-V	0.0002	0.115	0.0225	0.007		0.0035	0.0025	0.007	0.245	8.38	0.039	0.003	0.005	0.005	0.007	0.005	0.061	0.985	1040°C/30min + 750°C/2h & 950°C/30min + 750°C/2h	
OPTIFER-VI	0.0002	0.09	0.263	0.007		0.0036	0.0025	0.007	0.205	9.48	0.37	0.005	0.005	0.006	0.007	0.005	0.069	1.03	1040°C/30min + 750°C/2h & 950°C/30min + 750°C/2h	
OPTIFER-VII	0.0082	0.109	0.021	0.001	0.02	0.0035	0.003		0.19	9.31	0.602		0.005			0.002	0.055	1.27	1040°C/30min + 750°C/2h & 950°C/30min + 750°C/2h	
F82H-mod	0.0002	0.09	0.008	0.002	0.11	0.002	0.002	0.004	0.16	7.7	0.16	0.0037	0.021	0.0063	0.0101	0.003	0.009	2.04	950°C/30min + 750°C/2h	
JLF-1	<0.0005	0.106	0.028		0.05	0.012	0.003		0.18	8.7	0.52						0.08	1.91	1040°C/30min + 750°C/2h & 950°C/30min + 750°C/2h	
F82H		0.097	0.002	0.025	0.09	0.002	0.003			7.46	0.07						0.03	2.1	1040°C/40min + 740°C/2h	152
9Cr-2W		0.12			0.1	0.004	0.0017	0.04	0.26	8.98	0.52		0.02				0.07	2.07	1050°C/30min + 700°C/1h	174
JLF-3		0.09			0.1			0.001	0.2	7.03	0.45					0.01	0.07	1.97	1050°C/30min + 775°C/1h	175
MANET II		0.11	0.039			0.005	0.004			10.3	1.22		0.62	0.008	0.14	0.57			1075°C/30min + 750°C/2h	176
JLM-0		0.1			0.056	0.002	0.0017	0.02	0.25	8.65	0.5						0.044	1.92	1050°C/30min + 740°C/30min	31
JLM-1 (=JLM-0 + B)	0.0032	0.1			0.042	0.002	0.0014	0.021	0.26	9.03	0.53						0.051	2.06	1050°C/30min + 740°C/30min	
NFL-0		0.1			0.056	0.002	0.0017	0.02	0.25	8.65	0.5						0.044	1.92	1050°C/30min + 760°C/30min	177
NFL-1	0.0032	0.1			0.042	0.002	0.0014	0.021	0.26	9.03	0.53						0.051	2.06	1050°C/30min + 760°C/30min	
NFL-2	0.0029	0.1		0.028	0.05	0.002	0.002	0.018	0.25	8.98	0.53						0.059	2.01	1050°C/30min + 760°C/30min	
NFL-3	0.0027	0.1		0.029	0.04	0.002	0.001	0.017	0.24	8.92	0.52						0.058	2.01	1050°C/30min + 760°C/30min	
NFL-4	0.0027	0.1		0.009	0.03	0.002	0.002	0.017	0.25	9.01	0.52						0.06	2.03	1050°C/30min + 760°C/30min	
9Cr-WVTa	0.005	0.125	0.003						0.18	9.24				0.0005			0.1	1.06	1100°C/1h + 750°C/1h	178
9Cr-3WVTa	0.007	0.167	0.003						0.16	9.16				0.0005			0.1	3.08	1100°C/1h + 800°C/1h	
9Cr-1MoVNb		0.085	0.04		0.26				0.2	8.44	0.33				0.07	0.98			1050°C/1h + 760°C/1h	
MANET (DIN 1.4914)	0.0085	0.13	0.02		0.37				0.22	10.6	0.82		0.87		0.16	0.77			1050°C/2h + 1075°C/30min + 750°C/2h + 650°C/15min	179
EM10		0.105	0.024		0.37	0.016			0.03	8.76	0.48		0.18		0.05	1.05			980°C/30min + 750°C/30min	105
9Cr-1MoVNb	0.001	0.09	0.05	0.013	0.08	0.008	0.004	0.002	0.209	8.62	0.36	0.013	0.11	0.03	0.063	0.98		0.01	1040°C/30min + 760°C/1h	180
9Cr-1MoVNb (#30176)	0.0006	0.092	0.055	0.011	0.15	0.012	0.004	0.001	0.2	8.32	0.48	0.017	0.09	0.03	0.06	0.86		0.01	1040°C/30min + 760°C/1h	

In a modeling perspective, these steels were selected in the present work because they are expected to offer a large experimental database given all the international programs dedicated to their irradiation behavior, in fusion but also in other frameworks such as GEN-IV and ADS [4, 118, 181-187]. Note that the focus in this work is directed towards 9% Cr–steels. The 12%Cr–steels which were also often investigated together with the 9%Cr–steels were excluded from the database. The reason is the presence of δ–ferrite or α'–phase that enhances irradiation embrittlement by promoting χ–phase (chi phase) formation [83, 175, 188]. Note also that a monotonic decrease of the Charpy upper shelf energy was noticed with increasing Cr–content [189].

The 9%Cr–steels that are examined in this report exhibit typically a fully tempered martensitic microstructure with lath shaped martensite subgrains with a high density of $M_{23}C_6$ precipitates [190-193]. The $M_{23}C_6$ precipitates are Cr–rich carbides resulting form the tempering treatment [194]. They are preferentially located along grain and subgrain boundaries [190]. Other types of precipitates can also be found such as Ta– and V–rich MX–type precipitates [34, 195].

3.2.1. Effect of composition

Many investigations were carried out in the 90's to optimize the chemical composition of 9%Cr–steels [89, 123-124, 196-199]. In the case of 9%Cr–W–steels operating below 500°C, the 9%Cr–1WVTa was the most promising steel from the toughness point of view [196]. Such a typical steel, called Eurofer, was developed in Europe and was the subject a many investigations within the Fusion R&D activities [126, 133, 140, 190, 200-203]

As it will be seen later, in some cases, despite similar chemical compositions and heat treatments, very large discrepancies in the mechanical properties of the unirradiated condition can be noticed. This is the case for example with the 9%Cr–1MoVNb heats that were investigated by Klueh et al. [87, 161, 180, 204-205].

From the irradiation behavior point of view, it is difficult to unambiguously establish the relation between composition and irradiation hardening and embrittlement [85, 102, 196, 198-199, 206-207]. Of course, an element such as Ni would enhance the post–irradiation hardening and embrittlement in particular at low temperatures. But other elements such as W, Mo, Nb, V, … were primarily optimized to improve the mechanical properties in the unirradiated condition rather than improving the radiation resistance [124, 208, 198]. Sometimes, the microstructure optimization is done based on ageing properties [209].

Finally, it is important to point out that the effect of Cr–content on the DBTT–shift as shown in the famous Figure due to Kohyama et al. [128] and that is generally used to support the choice of 9%Cr–content is incorrect. Other data showing not so spectacular change of DBTT with Cr–content were also reported in [123, 127]. However, the DBTT determination based on Charpy impact data might be affected by the steel microstructure. As a result, the minimum DBTT–change shown to occur around 9%Cr–content is biased by the possible dislocation channel deformation inducing flow localization. It is believed that chromium content does not have a crucial effect except when compared to pure Fe or

high Cr–steels (>11%Cr) where the δ–phase, χ–phase or α'–phase may form [87, 188]. This is supported by experimental data reported by Hamilton and Gelles [210] who found that irradiation hardening was nearly independent of Cr–content. On the other hand, corrosion resistance is very much improved by Cr–addition [123, 211].

It is a matter of fact that 9%Cr–ferritic/martensitic steels have seen their development drastically increased the last years not only for fusion materials application but also for the next generation of fission reactors and the subcritical accelerator–driven systems. There is a worldwide interest of the international community in these materials because, as iron/chromium–based alloys, they offer an economically– and technically more viable alternative as structural materials than other special materials. Moreover, a well–established knowledge already exists on ferritic steels and it is expected that a number of findings will still be applicable to the martensitic steels. Of course, the approach that is followed here is not restricted to steels but can easily be implemented to other materials if the necessary ingredients are known.

3.2.2. Effect of heat treatment

The heat treatment affects directly the final microstructure of the material and consequently the mechanical properties [160, 209, 212-216]. A wide range of strength and toughness levels can be obtained as a function of heat treatment. In general, better toughness is obtained for low strength materials [214]. The 9%Cr–steels are usually submitted to a normalization treatment at 950–1100 °C followed by a tempering treatment at 700–800 °C. The effect of normalization on impact properties was found to be negligible [217]. Contrary to Rieth [217], Schäfer et al. [216] reported experimental data on F82H that exhibit a reduction of DBTT when normalization temperature is decreased from 1040°C to 920°C. The reduction of DBTT is concomitant to a reduction of the yield strength. The increasing of normalization temperature increases the grain size [218] and the increase of the annealing temperature reduces the material strength [218]. On the other hand, experimental data on MANET-I [217] and MANET-II [219] show that the effects of tempering temperature on the DBTT and USE are significant. In particular, it is found that increasing tempering temperature results in both reduction of the DBTT and increase of the USE. Recently, Wakai et al. [220] reported data on F82H irradiated at 250°C in the JMTR to 2 dpa that indicate a minimum irradiation hardening for tempering at 750°C for 1 h. Maiti et al. [42] reported a number of mechanical properties that indicate a peak in the microcleavage fracture stress when normalized around 1050°C. Above this temperature, the microcleavage fracture stress decreases.

Optimum heat treatment of 9%Cr–steels seems to be a normalization treatment at ~1000-1050°C/1h and a tempering treatment at 750°C/1-2h [213, 220]. In general, a reduction of the prior austenite grain size, by lowering the autenitization temperature, decreases the DBTT [160, 218]. Moreover, for a given grain size, tempering at higher temperature reduces the DBTT resulting from the lower strength. Irradiation effects can also be affected by the initial heat treatment [148, 216, 219].

3.2.3. Thermal aging

It is important to point out that besides irradiation resistance, the 9%Cr–steels should also exhibit a good resistance to thermal ageing. A number of investigations examined the behavior of 9%Cr–steels and in particular the effect of chemical composition on thermal aging [31, 124, 161, 190, 192, 207, 209, 213, 221-223]. In general, it is found that 9%Cr–steels are thermally stable for temperatures not exceeding 600°C. Above this temperature, Laves phases were observed and reductions of strength were noticed [102, 214, 222-223]. These Laves phases were also observed at lower temperatures, for example, in long term (>10000 h) thermally aged samples at 450-650°C [83, 207] and irradiated at 460°C to 60 dpa [197].

Swindeman et al. [224] reported loss of strength of a 9Cr-1MoV steel after aging above 600°C resulting from a coarsening of the tempered martensite substructure, in particular the precipitation of Laves (Fe_2Mo type) phase. Similarly, Gelles et al. [225] reported also precipitate coarsening under irradiation at 600°C. On the other hand, Hsu and Lechtenberg [226] reported that a thermal aging of an 8Cr-2WV steel at 600°C/1000 h without Laves phase formation. Laves phase was found by Fernandez et al. [192] on F82H steel after aging at 550°C and 600°C for 5000 h which resulted in a significant degradation of the Charpy impact properties. At 500°C during 5000 h, no effect was observed in aged Eurofer [190].

In general, the 9%Cr–steels under irradiation were found stable if the temperature remains below about 600°C [161, 226]. Above, softening was usually observed.

3.3. Effect of chemical composition/heat treatments on irradiation behavior

The aim here is not to present a detailed study on the effect of chemical composition on these kind of steels, other references can be found in literature, for example [102]. Here, we briefly report some of the effects related to chemical composition on the irradiation behavior, in particular chromium, the first alloying element that is added primarily to improve the oxidation and corrosion resistance. Kohyama et al. [128] collected literature data and showed that the DBTT–shift upon irradiation as a function of Cr–content exhibits a minimum around 9%Cr–content. This critical amount favoring a minimum DBTT–shift was also reported in [89, 127, 206]. However, as already mentioned before, the monitoring of irradiation embrittlement by the DBTT can be biased if dislocation channel deformation occurs [36]. Hamilton et al. [121] investigated the effect of Cr and Mn on the irradiation behavior of Cr–steels irradiated to 30 dpa at 375°C. The minimum DBTT–shift was obtained with the 7.5%Cr–content. The data indicate also a reasonable correlation between embrittlement and Mn–content.

Klueh et al. performed a detailed study to understand the differences observed between tensile and Charpy impact post-irradiation data of 9Cr-2WV and 9Cr-2WVTa [32, 90, 92]. In particular, the post–irradiation hardening of both steels are comparable but their embrittlement not. In particular, Ta was found to lower the DBTT. The possible causes were systematically investigated, such as grain size (lath size or prior austenitic grain

size) and microstructure, but were ruled out. The plausible explanation according to these authors is the change of effective surface energy, and by extension the critical fracture stress. This is probably true. However, an additional potential reason for the difference between both steels is the upper shelf behavior and the DBTT definition. Indeed, the upper shelf energy of 9Cr–2WVTa is 30% higher than of 9Cr–2WV (11.2 J versus 8.4 J). This means that the density/size of the second phase particles in 9Cr-2WV are higher than in 9Cr–2WVTa. The tearing resistance (ductile crack growth) is different in these steels. Because the DBTT is evaluated at 50% of the upper shelf energy, the DBTT is influenced by the ductile tearing resistance.

The "best" choice of the 9Cr–2WVTa composition was supported by the experimental data of Klueh and coauthors [89] that show the least embrittlement in terms of DBTT–change.

In a general way, literature data do not report any clearly identified effect of a specific element on irradiation behavior. Instead, the effects of the elements refer often to the initial properties rather than on irradiation behavior.

The appropriate heat treatments were usually optimized to obtain high strength/high toughness but a lowest DBTT [102, 212, 216-220, 227-228]. However, high strength leads to lower toughness and vice versa. One way to improve toughness is to reduce the size and number density of the carbides [229]. But this would result in a lower strength. From the post–irradiation behavior point of view, few investigations were published in literature [148, 160] and these do not allow providing a clear and full understanding. Klueh et al. [160] reported no significant effect of the heat treatments for 9Cr–1MoVNb irradiated at 365°C and 420°C in a range of 4 to 100 dpa. They suggested reducing the initial DBTT by reducing the prior austenite grain size. On the other hand, Wakai et al. [148] reported a significant effect of the tempering temperature and time on the post–irradiation hardening of F82H steel irradiated at 250°C up to 1.9 dpa. In particular a second normalizing and tempering treatment was found beneficial in reducing the radiation hardening. However, no explanation was provided.

As it will be seen later, all 9%Cr–steels considered in our database were considered to belong to one single heat despite some differences in their chemical composition and heat treatments. Two underlying reasons for this choice are that, on one hand, obviously there is no significant effect of material composition and heat treatment on the post irradiation behavior (in terms of irradiation hardening and embrittlement) and on the other hand, it will be difficult or impossible to built an appropriate database that can be used for modeling if chemistry and heat treatment variables are also taken into account.

Several techniques have been used to study helium effects, including nickel and boron doping, helium implantation with accelerators and injector foils and spallation neutron sources [152, 154, 156, 157, 159, 194, 197, 230-238]. Finally, note that because Ni and B may induce undesirable changes in the initial microstructure [108], another very interesting technique was proposed in [239-241] that uses Fe–isotopes rather than Ni or B, in particular ^{54}Fe, which was used also for hydrogen production [242-243].

Unfortunately, its excessive price, something like 20 kUS$/g [236], makes it financially unacceptable.

3.4. Microstructural changes under irradiation of 9%Cr–F/M steels

Irradiation temperature is the primary parameter that controls the irradiation–induced defects. In general, their density decreases while their size increases with increasing irradiation temperature [114].

Below about 450°C, a number of radiation – induced precipitates were identified, including G–phase, α'–phase, M_6C and χ– phase [83]. Laves phase, which forms during thermal aging at 400–600°C, does not form during irradiation below 600°C [83].

Small angle neutron scattering (SANS) measurements performed by Mathon et al. [244] revealed nano–scale precipitation of Cr–enriched bcc α'–phase under irradiation. It was shown by these authors that precipitation kinetics under irradiation are much faster than under thermal ageing and the α' formation by a classical nucleation and growth process occurs according to a simple irradiation–accelerated mechanism. Finally, for the 9%Cr–steels, the irradiation hardening is mainly attributed to point defect clusters rather than precipitates.

Materna-Morris et al. [108] reported systematic microstructural investigations on five 9%Cr–steels irradiated at 250 and 450°C. Dislocation loops could be identified at 250°C (10^{21}–10^{23} m^{-3}) but not at 450°C. α'–precipitates were also found at 250°C (10^{21}–10^{22} m^{-3}) but not at 450°C except for one material. On the other hand, He–bubbles were found at both irradiation temperatures, with size and number density of 1.5–3 nm/10^{21}–10^{23} m^{-3} and 2–6 nm/10^{21}–10^{22} m^{-3} at 250°C and 400°C, respectively. The He-bubbles were usually located near subgrain boundaries and dislocations.

Dubuisson et al. [106] noticed that in general, in terms of precipitates, the microstructure is not significantly modified by irradiation. Actually, small dislocation loops are the defects that are mostly reported in literature [6, 106], their number decreasing with increasing temperature.

Kai and Klueh [245] conducted detailed microstructural analysis on three 9%Cr–steels, 9Cr–1MoVNb, 9Cr-2WVTa and 9Cr–2WV, irradiated at 420°C to 35 dpa. Before irradiation, the mainly $M_{23}C_6$ precipitates were identified together with MC carbides. After irradiation, a high dislocation loop density was observed in all steels without formation of additional phases except in the 9Cr–1MoVNb where chi phase is observed.

Ogiwara [246] reported microstructural TEM data on JLF–1 steel ion–irradiated at 420°C up to 60 dpa using single and dual–beam ion irradiation.
Tanigawa et al. [247] reported amorphization of the radiation–induced precipitate $M_{23}C_6$ of Fe–ion irradiated F82H at 300°C but not at 500°C and amorphization of Laves phase irradiated/aged F82H at 300°C.

Amorphization of $M_{23}C_6$–precipitates was initially reported by Dai et al. [193] and confirmed by a number of other authors [114, 117, 185, 247-249]. The amorphization of $M_{23}C_6$–precipitates under irradiation does not only occur at low temperature but at high temperature as well [247]. Laves phases were also amorphized in Fe ion aged F82H steel at 300°C [247]. Further discussion on amorphization, in particular the effect of temperature, can be found in [247].

In the case of 9%Cr–steels, the majority of precipitates in both unirradiated and irradiated condition are $M_{23}C_6$–type [146]. Moreover, an apparent effect of irradiation on precipitation was reported in [146]. Ando et al. [250] reported microstructural observations of ion–irradiated F82H indicating that the defects consist of interstitial loops [6, 31, 174] and defect clusters, consistent with other authors [12, 251].

A non exhaustive summary of the various microstructural observations is given in Table 2.

Table 2. Summary of microstructural studies performed on irradiated 9%Cr–steels.

reference	material	T_{irrad} (°C)	dose (dpa)	He–content (appm)	dislocation loop size (nm)	dislocation loop density (m^{-3})	precipitate size (nm)	precipitate density (m^{-3})	void/bubble size (nm)	void/bubble density ($10^{23} m^{-3}$)
Ogiwara [246]	JLF-1	420	60		5.1	$8.4\ 10^{22}$				
	JLF-1	420	60	900	6.6	$1.4\ 10^{23}$	7.3	$4.8\ 10^{21}$		
	Fine M(Ta,V)X precipitates under dual beam responsible of the additional hardening									
Tanigawa [77]	F82H (IEA)	300	5		3.5	$6.6\ 10^{23}$				
	JLF-1	300	5		3.6	$5.9\ 10^{23}$				
	ORNL9Cr	300	5		4.2	$7.6\ 10^{23}$				
	$\Delta\sigma_y$=370, 314 and 463 MPa (for F82H-IEA, JLF-1 and ORNL9Cr, respectively). Based on dislocation loops, $\Delta\sigma_y$=310, 300 and 363 MPa. The difference in radiation hardening of the various materials was attributed to precipitate accumulation on block/packet and PAG boundaries.									
Tanigawa [247]	F82H (IEA)	300/500	10/20	150/300						
	JLF-1									
	ORNL9Cr									
	Qualitative data only, M23C6 amorphization in F82H at 300°c but not at 500°C, refined microstructures after irradiation.									
Jung [165]	Eurofer-97	250	0.38	2500						
	After annealing at 550°C and 750°C, high density of bubbles with 1.5 and 1.7 nm size, respectively.									
Dai [144]	F82H	60	0.8	125	2.1	$1.6\ 10^{22}$				
			1.6	235	2.4	$2.4\ 10^{22}$				
			5.9	1055	3.1	$3.3\ 10^{22}$				
	Size and density of the small loops increase with dpa. No bubbles are observed. Upon annealing (160-400°C/0.3-2h) loop size increases while loop density decreases. Only partial recovery of the yield strength is observed. The residual hardening can be attributed to the total dislocation line density that has increased from $1.2\ 10^{14}$ m^{-2} to $5.5\text{-}7.5\ 10^{14}$ m^{-2}.									
Ando [250]	F82H	360	3-50	up to 3300	~20	n.a.	<5	n.a.		
	Interstitial loops (20 nm), defect clusters ((<5nm) and dislocation networks were detected. He–implantation results in additional hardening due to nano–voids.									
Jia [252]	F82H weld	68	2.2	125	3.8	$3.1\ 10^{22}$			-	-
		110	3.8	214	3.3	$3.0\ 10^{22}$			-	-
		200	5.7	375	3.9	$3.1\ 10^{22}$			-	-
		245	10.4	780	5.8	$4.1\ 10^{22}$			1	$5.0\ 10^{23}$
		345	11.1	1000	7.5	$1.6\ 10^{22}$			1.3	$5.3\ 10^{23}$
	Radiation defects identified as black dots and interstitial loops with size and density similar to base metal. Bubbles are observed only at high temperatures / high He–contents.									
Jia [114]	F82H	360	11.8	1115	8.1	$1.5\ 10^{22}$			1.6	$4.3\ 10^{23}$
		295	9.7	670	6.5	$2.7\ 10^{22}$			1.4	$4.0\ 10^{23}$
		255	10.1	735	5.5	$3.8\ 10^{22}$			1.2	$4.2\ 10^{23}$
		235	9.9	560	3.6	$3.6\ 10^{22}$			0.9	$4.7\ 10^{23}$
		210	9.9	560	3.5	$3.4\ 10^{22}$			0.8	$4.6\ 10^{23}$
		175	9.9	560	3.3	$2.3\ 10^{22}$			0.7	$5.1\ 10^{23}$
		140	9.4	705	3.7	$3.6\ 10^{22}$				
		200	5.7	375	3.7	$1.9\ 10^{22}$				
		110	3.8	225	3.2	$2.7\ 10^{22}$				
		90	2.7	145	2.1	$2.6\ 10^{22}$				
	T91	360	11.8	1115	8.9	$1.3\ 10^{22}$			1.4	$5.1\ 10^{23}$
		295	10.1	725	5.4	$3.3\ 10^{22}$			1.2	$5.3\ 10^{23}$
		250	8.3	540	4.5	$3.6\ 10^{22}$			1.1	$5.4\ 10^{23}$
		205	5.8	380	4.4	$1.8\ 10^{22}$				
		130	4.6	235	3.8	$2.5\ 10^{22}$				
		110	3.8	225	3.0	$2.1\ 10^{22}$				
	Between ~90 and ~250°C, size and density are both insensitive to irradiation temperature. Above ~250°C, defect size increases while density decreases. At ~10 dpa, Helium bubbles with ~1nm size and 4-5 10^{23} m^{-3} density were observed above T_{irrad}≈175°C and He–content > 500 appm He. $M_{23}C_6$–amorphization observed below T_{irrad}≈200°C.									
Mathon [244]	LA4Ta (CW)	325	0.7				1.1	$1.3\ 10^{24}$		
		325	2.9				1.2	$3.4\ 10^{24}$		
		aging 400°/10000h					1.5	$1.1\ 10^{23}$		
	LA12LC (CW)	325	0.7				1.4	$5.0\ 10^{22}$		
		250	2.4				1.2	$6.6\ 10^{23}$		
		400	2.4				0.9	$3.6\ 10^{23}$		
	LA12TaLC (CW)	250	2.4				1.3	$6.8\ 10^{23}$		
		400	2.4				0.8	$1.3\ 10^{23}$		
	LA13Ta (CW)	325	0.7				-	0		

reference	material	T_{irrad} (°C)	dose (dpa)	He–content (appm)	dislocation loop size (nm)	dislocation loop density (m^{-3})	precipitate size (nm)	precipitate density (m^{-3})	void/bubble size (nm)	void/bubble density ($10^{23} m^{-3}$)
Mathon [244]	F82H	325	0.7				-	0		
		325	2.9				*	*		
	HT9	325	0.7				1.2	$1.0\ 10^{24}$		
	MANET-II	325	0.7				1.2	$3.1\ 10^{23}$		
	T91 (CW)	325	0.7				1.3	$0.9\ 10^{23}$		
	EM10	325	0.7				1.0	$6.0\ 10^{23}$		
	EM10 (CW)	325	0.7				1.5	$1.4\ 10^{23}$		
	SANS measurements for Cr–rich α'–precipitation under irradiation much faster than under thermal aging. α'–phase density increases with Cr content and neutron exposure but decreases with increasing temperature. Irradiation hardening is mainly due to point defect clusters but the α'–phase contribution becomes evident for high Cr–content steels. (*) vacancy clusters rather than α'–precipitates.									
Ando [235]	F82H	350	5		8.5	$9.0\ 10^{22}$				
	50 appm He co–implantation does not cause additional hardening. Irradiation hardening is largely due to dislocation loops, dot–like defects and network dislocations. Ni–addition increases hardening but not through the He–embrittlement process.									
Hashimoto [253, 157]	9Cr-1MoVNb	400	12.1	30	21 25	$5.0\ 10^{21}$ $4.0\ 10^{21}$	95 --	$<1.0\ 10^{20}$ --	9	$3.0\ 10^{21}$
	9Cr-1MoVNb-2Ni	400	12.3	161	20 24	$7.0\ 10^{21}$ $6.0\ 10^{21}$	98 (M_2X) 54	$<1.0\ 10^{20}$ $5.0\ 10^{20}$	5	$9.0\ 10^{21}$
	9Cr2VWTa-A	400	12	25	18 28	$1.0\ 10^{22}$ $5.0\ 10^{21}$	95 --	$<1.0\ 10^{20}$ --	2.7	$1.3\ 10^{21}$
	9Cr2VWTa-B	400	12	25	23 30	$1.0\ 10^{22}$ $4.0\ 10^{21}$	102 --	$<1.0\ 10^{20}$ --	9.0	$9.6\ 10^{20}$
	9Cr2VWTa-2Ni-A	400	12.3	150	17 16	$1.0\ 10^{22}$ $6.0\ 10^{21}$	92 (M_6C) 7	$<1.0\ 10^{20}$ $2.0\ 10^{21}$	3.0	$2.7\ 10^{21}$
	9Cr2VWTa-2Ni-B	400	12.3	150	23 28	$1.0\ 10^{22}$ $6.0\ 10^{21}$	98 (M_6C) 6	$<1.0\ 10^{20}$ $2.0\ 10^{21}$	4.3	$3.0\ 10^{21}$
	A and B correspond to the tempering temperature, 700°C and 750°C, respectively. The irradiation–induced loops correspond to a_0<100> and (a_0/2)<111> type loops, respectively while precipitates correspond to $M_{23}C_6$ and M_6C/M_2X type precipitates. The increase of hardening in Ni–doped steels was attributed to the formation of radiation–induced precipitates (M_6C/M_2X) and cavities.									
Materna-Morris [108]	OPTIFER-Ia	250	0.8	<60		$5.9\ 10^{21}$		$1.0\ 10^{22}$	2.0	$1.5\ 10^{22}$
	OPTIFER-Ia	450	0.8			--		--	2.0	$5.7\ 10^{21}$
	OPTIFER-II	250	0.8	<60		$2.6\ 10^{23}$		$2.1\ 10^{21}$	3.0	$3.8\ 10^{24}$
	OPTIFER-II	450	0.8			--		--	6.0	$1.2\ 10^{21}$
	F82H	250	0.8	<20		$1.9\ 10^{22}$		$7.5\ 10^{21}$	1.5	$<1.4\ 10^{23}$
	F82H	450	0.8			--		$1.9\ 10^{22}$	3.0	$<3.7\ 10^{22}$
	ORNL 3791	250	0.8	<10		$1.0\ 10^{21}$		$3.5\ 10^{21}$	2.0	$<1.1\ 10^{21}$
	ORNL 3791	450	0.8			--		--	3.0	$<4.6\ 10^{21}$
	MANET-II	250	0.8	70		$1.4\ 10^{21}$		$3.8\ 10^{21}$	2.0	$3.6\ 10^{22}$
	MANET-II	450	0.8			--		--	4.0	$1.1\ 10^{22}$
	Precipitate and loop size were not given. The embrittlement (ΔDBTT) of the various materials were shown to be proportional to the He – content (calculated from ^{10}B burn–up). However, this is not supported by the tensile properties.									
Kai [245] Klueh [32]	9Cr-2WV	420	36		50	$3.0\ 10^{21}$	160 160	$3.2\ 10^{19}$ $1.1\ 10^{18}$	25	$2.5\ 10^{19}$
	9Cr-2WVTa	420	36		50	$3.0\ 10^{21}$	143 36	$4.1\ 10^{19}$ $5.6\ 10^{18}$	25	$4.0\ 10^{19}$
	9Cr-1MoVNb	420	36		100	$5.0\ 10^{19}$	155 40 10 (χ)	$2.6\ 10^{19}$ $6.8\ 10^{18}$ $8.6\ 10^{20}$ (χ)	30	$6.0\ 10^{20}$
	The precipitates correspond to $M_{23}C_6$, MC (V– and Ta–rich) and χ precipitates, respectively. The major microstructural change for all steels after irradiation is the formation of dislocation loops and the χ– phase for the 9Cr-1MoVNb steel.									
Dubuisson [106]	HT9	419	79				5.4	$1.2\ 10^{22}$		
	DIN 1.4914	429	68				11.7	$2.0\ 10^{21}$		
	DIN 1.4914	459	50				21.9	$8.0\ 10^{20}$		
	The radiation defects responsible of the embrittlement were identified as M_6C–precipitates .									
Kohno [155]	F82H	365	6.7						12.7	$6.8\ 10^{19}$
		405	35.8						22.7	$2.3\ 10^{20}$
		550	37.0						--	--
		670	28.3						--	--
		750	37.1						--	--
	Precipitates were identified to be $M_{23}C_6$ except at 750°C with W–rich Laves phase. No change of the size and distribution of carbides is observed upon irradiation. No cavity formation was observed for irradiation at or above 550°C.									

3.5. Effect of Helium

A significant analytical and theoretical work has been done on helium embrittlement at Forschungszentrum Jülich [254-256,] and in the US [257-262]. These investigations resulted not only in a significant improvement of basic understanding on the nucleation and growth of He–bubbles in solids but also a reasonable agreement with experimental data was reached [97, 263-265]. However, from an experimental point of view, most of these data were related to swelling of austenitic stainless steels. Moreover, there was no database extensive enough to include a reasonably large number of variables. Finally, for the properties of interest in this report, namely hardening and embrittlement, experimental data are scarce, mainly because of the difficulty to inject helium in materials.

The development of advanced nuclear systems such as fusion and spallation sources has motivated material scientists to increase the efforts in assessing the effect of helium on the mechanical properties of structural materials. In the following, a brief review will be given on the few techniques that were used to inject in controlled manner helium into metals. Afterwards, a literature survey will be made to extract the most important parameters that should be taken into account.

3.5.1. Helium generation in fusion materials

Besides the usual radiation damage related to the atomic displacements resulting in the perturbation of the crystalline structure, another damage mechanism that affects the structure of the material is the production of transmutation products through nuclear reactions. This damage mechanism is a concern for both fusion and spallation environments [119, 266-267]. While the amounts of metallic atoms that are produced under irradiation through a transmutation process are very small and do not significantly affect the material properties, it is not the case for gas atoms, such as helium and hydrogen. Although its production rate will be significantly higher than for helium [119, 266, 268] hydrogen will not be treated here. Indeed, its effect is less critical because of its relatively high mobility in comparison to He. Therefore the limited experimental investigations reported in literature are in the low temperature range, around room temperature [269]. Hydrogen can be easily removed by a diffusion process when temperature is above ~250°C [270]. Helium on the other hand is a serious issue and may drastically degrade the mechanical properties of materials. Contrary to hydrogen, increasing temperature would favor He–diffusion to grain boundaries under the supply of vacancies forming large He–bubble size that might lead to premature fracture. In the following, focus is put on helium, not on hydrogen despite the production rate of the latter that is about one order of magnitude higher.

The (n, α)–nuclear reactions are the main source of He generation [241, 263, 271]. Other sources are generally less critical, for example, first wall materials exposed to high fluxes of α–particles escaping from the confinement or He–generation by tritium decay since they do not significantly affect the bulk properties [263].

There are three important reactions contributing significantly to He–production in fusion reactor structural materials involving neutron interaction with atoms [263].

1. The first one is related to high energy neutron–induced (n, α)–reactions, such as:

$$ {}^{A}_{Z}M + {}^{1}_{0}n^{f} \rightarrow {}^{A-3}_{Z-2}M' + {}^{4}_{2}He \quad \text{(several MeV)} \tag{7a} $$

$$ {}^{A}_{Z}M + {}^{1}_{0}n^{f} \rightarrow {}^{A-4}_{Z-2}M'' + {}^{1}_{0}n' + {}^{4}_{2}He \tag{7b} $$

   The cross-sections of such reactions are very high for a fusion neutron spectrum. Example of cross sections for various metals as a function of neutron energy can be found in [263]. (n,α)–reactions occur in a fission reactor but require a hard neutron spectrum. The He–production rate in typical material test reactors (MTR) is low (<1 appm He/dpa). Fast breeder reactors and mixed neutron–proton reactors have an energy spectrum that promotes higher He–generation rates. Finally, the fusion 14 MeV neutrons resulting from the deuterium–tritium fusion reaction allows He–generation at a rate of about 10 appm He/dpa. Helium generation cross sections of various elements for 14 MeV neutrons can be found in [272].

2. The second one is related to the thermal neutrons with two–step reactions involving specific isotopes, such as Ni:

$$ {}^{58}_{28}Ni + {}^{1}_{0}n^{th} \rightarrow {}^{59}_{28}Ni + \gamma \tag{8a} $$

$$ {}^{59}_{28}Ni + {}^{1}_{0}n^{th} \rightarrow {}^{56}_{26}Fe + {}^{4}_{2}He \qquad (4.76\ MeV) \tag{8b} $$

   This He–generation process was often used to simulate fusion irradiation conditions and will be discussed later.

3. Finally, the third reaction involves boron because of its very high cross section ($\sigma_{th} \approx 4000$ barn [263, 272]):

$$ {}^{10}_{5}B + {}^{1}_{0}n^{th} \rightarrow {}^{7}_{3}Li \quad (0.84\ eV) + {}^{4}_{2}He\ (1.47\ MeV) \tag{9} $$

The first reaction with high energy neutrons (14 MeV fusion reactions) is the most interesting one but unfortunately there are, to date, no sources that are capable of providing such a neutron spectrum with a relatively high flux. It is the objective of the International Fusion Materials Irradiation Facility (IFMIF) to provide such an intense 14 MeV neutron flux to investigate fusion materials [273]. In the absence of such an experimental tool, researchers have used the Ni– and B–doping techniques to generate helium.

Nickel was extensively used to generate helium [157, 159, 194, 232, 234-236, 238, 253, 274]. However, these data were excluded from the database, in particular at low temperature where Ni might affect not only the helium component but also the radiation damage component [236]. Boron was also used in 9-12%Cr–steels to increase the He–production, in particular by Wakai et al. [152, 142-143, 152, 154, 197, 233-234].

Other helium generating processes such as proton bombardment, α-particle implantation and tritium trick were also used; their description can be found in literature [271]. For the very high He–contents (above 0.1 at.%), most of the available data were obtained by implantation. Unfortunately, as will be seen later, the associated dpa level is usually quite small (< 1 dpa).

Finally, it is worth mentioning some alternative approaches. The first one related to the doping approach was suggested to reduce uncertainties of using Ni and B by replacing the natural dopants by their isotopes [236, 241]. The second approach suggests the use of thermal neutron shielded and unshielded capsules in a mixed neutron spectrum reactor allowing various He–to–dpa values. Finally, an interesting in–situ He–implantation technique was proposed by Yamamoto et al. [275] which consists in irradiating in a high flux reactor the target (material to be investigated) that was previously coated with NiAl. The (n,α)–reaction with Ni allows a uniform He concentration of 5–50 appm He/dpa to a depth of 5–8 μm.

For ITER, the maximum radiation damage level achieved by any structural material is not exceeding a few dpa. On the other hand, for DEMO, the radiation damage levels will reach 150–200 dpa with He–production rates of ≤10 appm He/dpa and hydrogen isotopes of ≤50 appm H/dpa [273].

3.5.2. Helium effects on the mechanical properties of fusion materials

From an experimental point of view, many contradictions can be found in literature on the effect of helium on the mechanical properties. For high He–contents, obtained usually with implantation, there is a clear effect of He on hardening and consequently on embrittlement. But in the low range of He–concentrations, from a few appm He up to few hundreds, literature data is confusing [35, 161]. The contribution of helium to hardening and embrittlement is far from being well established. For example, the significant difference in irradiation hardening between specimens irradiated in HFIR and EBR-II cannot be attributed to helium [161].

3.6. Conclusion

The basic irradiation effects on 9%Cr–steels were reviewed. The tempered martensite consists of a lath structure containing mainly Cr–rich $M_{23}C_6$ precipitates. Other precipitates might be found such as MC, MX, Laves phase but their impact is small. The metallurgical structure of 9%Cr–steels is usually stable below ~600°C. Under irradiation, no significant phase formation was reported.

Of course from an engineering modeling point of view, it is necessary to simplify the story without loosing much reliability. It is clear that in the low temperature regime, the defect structure in the irradiated condition is dominated by point defect clusters and small dislocation loops. There are indications that with increasing neutron exposure, a number of these defect clusters are transformed into small loops. The density of these defects decreases with increasing irradiation temperature and we can consider that above about

450°C, the annealing recovery does not allow to maintain the effectiveness of these point defect clusters and small loops. This means that above 450°C, the damage component vanishes.

In comparison to neutron displacement damage, helium studies are not so extensive. A number of investigators have clearly revealed the presence of helium bubbles. However, it is not clear at all from which threshold level helium starts to have significant effect on hardening and embrittlement. For high He–content, usually obtained though implantation techniques, there is no doubt that the observed hardening results primarily from He. On the other hand, for less than about 1000 appm He, the effect of He on hardening/embrittlement is not so obvious as very often the dpa component is also high.

For modeling purposes and for the temperature window of interest on one hand and the fact that major irradiation effects are observed in the low temperature range on the other hand, we will deliberately limit the damage modeling into two distinct components, one related to the displacement damage and the other on the He–component. The dpa component will be primarily related to the point defect clusters and their evolution into small loops. The He–component will be related to helium bubble generation. We could also have included a third component related to phase precipitation but its contribution is small and appears mainly at high temperature. Anyhow, as it can be seen from the summary Table 2 there are not sufficient data that allow investigation of the kinetics of precipitation as a function of dose and irradiation temperature.

IV. EXPERIMENTAL DATABASE

4.1. Introduction

An experimental database is a requirement to develop an engineering modeling. As already mentioned, one of the most important properties from a design point of view is fracture toughness. Unfortunately, experimentally measured fracture toughness data are scarce and only very few data could be found in literature [47, 276-279]. As a result, focus is put on the tensile and Charpy impact data which are mostly reported in literature for monitoring irradiation effects.

Modeling relies on a number of key experimental data to precisely define a number of generic trend curves such as the temperature dependence, the fluence dependence, the helium content dependence … Therefore, the performance of any model depends on the experimental data on which it relies. Any excessive scatter in the experimental data would be transferred to or reflected on the model prediction. Biased experimental data would bias the model parameters as well, and therefore, it is important to discard from the database any suspicious data. The difficulty remains how to detect the suspicious data when raw data are not available and only treated data are given in literature. For example, only the DBTT data (from Charpy impact tests) or yield strength change (from tensile tests) are often reported in literature. Details on the number of specimens that were used and the individual instrumented test records are usually missing. Also details on the irradiation conditions are missing. Moreover, other parameters such as the specimen size, test procedure, dosimetry measurement, … should ideally be taken into account. In practice, this is unfortunately not the case. For example, there is no monitor material in any of these irradiations to effectively verify the correspondence between radiation damage in various reactors. Also, in some cases, physical inconsistencies were detected in the experimental data requiring their censoring. However, the data censoring was very limited to avoid a drastic reduction of the size of the database. So, all these uncertainties lead to a large scatter in the input data, see for example Figures 15 and 16 taken from literature. Of course, another important parameter which is responsible of this large scatter is related to the material composition and heat treatments. As it will be seen later, the scatter is significantly reduced when data from a single material irradiated in the same reactor and tested in the same laboratory are examined. Some of literature data had to be discarded because of variable irradiation temperature [113, 117, 280]. It is clear that the combination of all these small differences can lead to a wrong picture on the actual irradiation effects but there is no other alternative. Nevertheless, the work presented here does not aim to remain as it is presented here but would require updating as new more reliable experimental data become available.

In the following, the initial properties of 9%Cr–steels will be examined together with effects of irradiation and post-irradiation annealing treatments. In particular, the flow and fracture properties will be examined. These are very important to support the findings of the present work in terms of modeling.

4.2. Analysis of the experimental data used in the database

4.2.1. Baseline properties of 9%Cr–steels

4.2.1.1. Tensile properties

The initial tensile properties of 9%Cr martensitic steels exhibit a temperature dependence typical of bcc materials. Depending on the chemical composition but more specifically on the heat treatments, the 9%Cr–steel properties found in literature exhibit a very large scatter, as shown in Figure 15 for the yield strength and Figure 16 for the tensile strength. The temperature dependence of the yield strength exhibits a typical trend curve of many steels but, as it can be seen, at room temperature, the yield strength ranges between 380 and 760 MPa. Actually, the variations in the tensile properties are not well understood. For example, the chemical composition and the heat treatments of the 9%Cr-1MoVNb steel investigated by Klueh et al [161] are typical of this steel class and quite similar to other materials (1040°C/0.5h + 760°C/1h) but the yield strength at 400°C is significantly higher than usually observed, 754 MPa versus ~460 MPa. Another similar steel with a slightly different heat treatment (1050°C/0.5h+700°C/5h) exhibiting also such high yield strength at high temperature was recently reported by Klueh et al. [156]. Addition of 2%Ni may also increase the tensile resistance of 9%Cr–steels [180]. The irradiation–induced hardening will be affected by the initial yield strength simply because of the saturation phenomenon (defect recombination). It is therefore important to keep in mind these large discrepancies in the initial tensile properties when assessing the performances of the model.

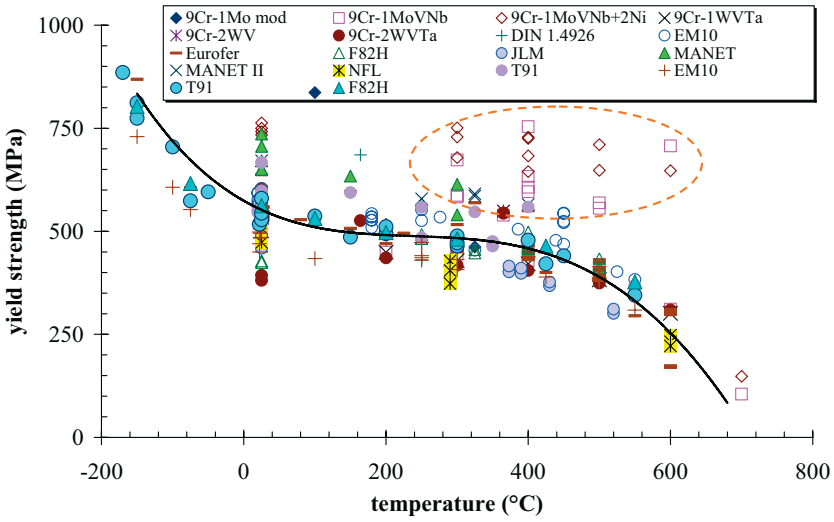

Figure 15. Yield strength – temperature dependence in the unirradiated condition of various 9%Cr–steels.

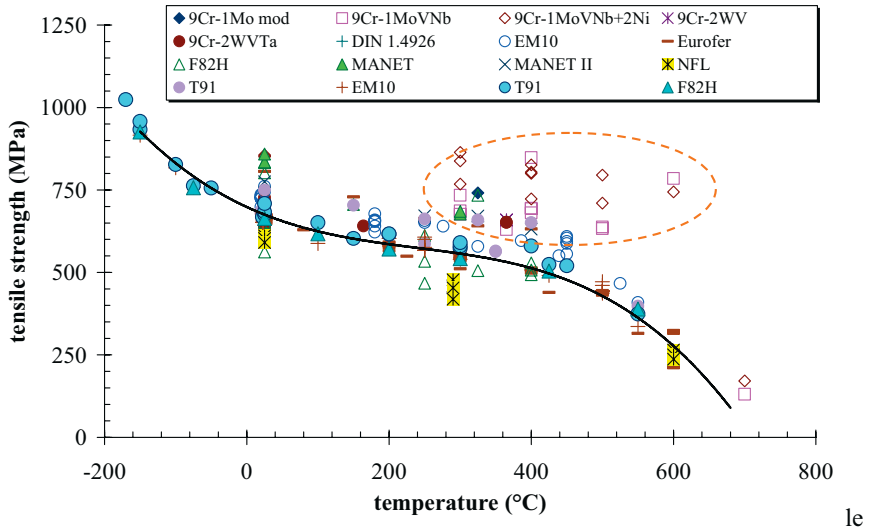

Figure 16. Tensile strength – temperature dependence in the unirradiated condition of various 9%Cr–steels.

The data which clearly lie outside the general trend curve were identified as those of 9%Cr-1MoVNb steel and are plotted in Figure 17. The chemical composition of these steels is very similar and the heat treatments as well (see Table 3). Actually, the same heat labeled XA-3590 was used in [112, 156, 161, 180, 205]. Despite these similarities, the tensile data indicate values which cannot be understood.

Finally, it is interesting to select only one material, say F82H instead of all 9%Cr–steels. This is shown in Figure 18 and as it can be seen at room temperature, large deviations can be observed.

These examples clearly illustrate the difficulty of relying on experimental data that are used to calibrate and validate modeling. It should be emphasized here that these data are in the unirradiated condition and still one single material can exhibit such a large scatter in the initial properties. As a matter of fact, this modeling approach should be carefully looked at given all these discrepancies.

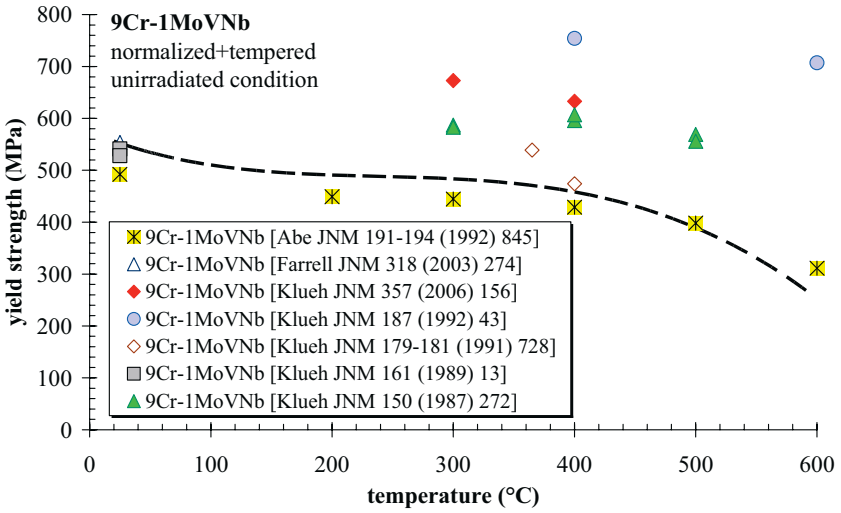

Figure 17. Yield strength – temperature dependence of unirradiated 9Cr-1MoVNb steels.

Table 3. heat treatments of the various 9Cr-1MoVNb steels.

reference	$T_{normalization}$ (°C)	$t_{normalization}$ (hr)	$T_{tempering}$ (°C)	$t_{tempering}$ (hr)
Abe et al. [281]	1050	0.5	760	1.5
Farrell et al. [112]	1040	1	760	1
Klueh et al. [156]	1050	0.5	700	5
Klueh et al. [161]	1040	0.5	760	1
Klueh et al. [199]	1050	0.5	760	1
Klueh et al. [180]	1040	0.5	760	1
Klueh et al. [205]	1040	0.5	760	1

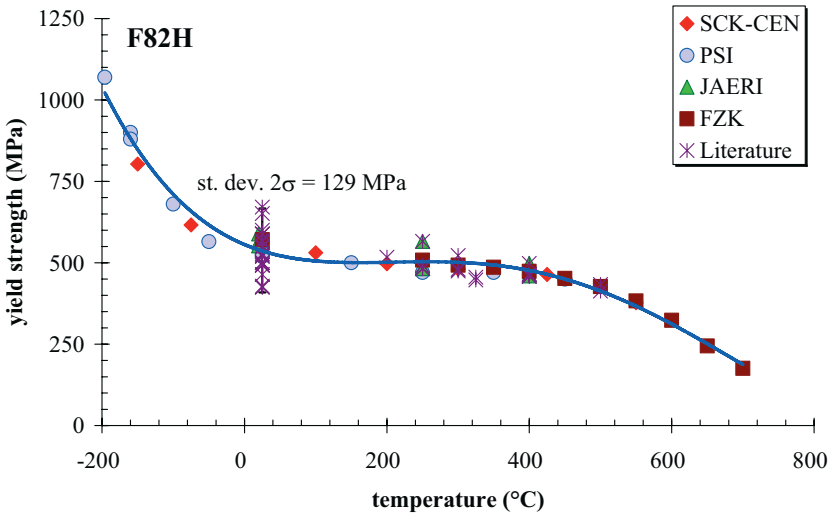

Figure 18. Yield strength – temperature dependence of unirradiated F82H steel.

4.2.1.2. Charpy impact properties

The initial Charpy impact properties of 9%Cr–steels vary also from one material/heat to another. As a matter of fact, examination of the KLST–Charpy impact properties obtained by Schneider et al. [172-173] on various 9%Cr–steels shown in Figure 19 indicate that there is only a little dependence of the transition curve on the material. Also indicated in Figure 19 is the transition temperature range for a single material, namely F82H, which was tested by various laboratories in a round robin exercise. As it can be seen, the scatter is in the order of magnitude of the scatter observed on all other materials. More important, examination of the dynamic general yield strength depicted in Figure 20 clearly shows the small effect of material on this property.

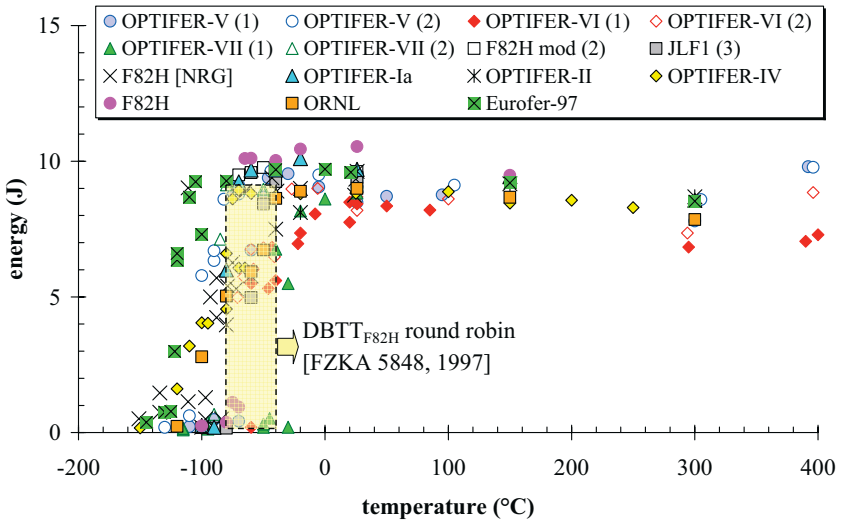

Figure 19. The DBTT of unirradiated 9Cr–steels is within the DBTT–range measured during a round robin on a single F82H material.

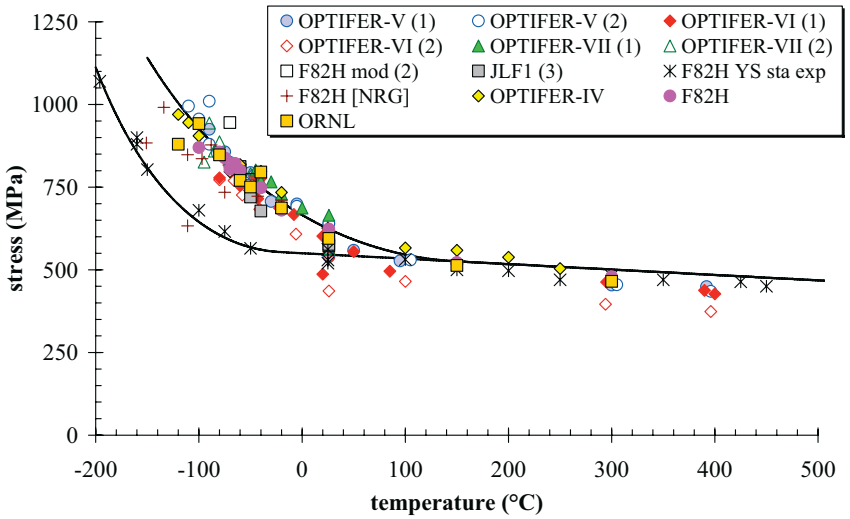

Figure 20. Load diagram representing a variety of 9%Cr–steels that exhibit a single yield strength temperature dependence.

4.2.2. Irradiation Effects on the mechanical properties of 9%Cr–steels

It is important to emphasize that nearly identical initial properties do not mean that the various steels will be equally affect by irradiation. However, using the same Schneider et al. data [172-173], it is not always easy to extract consistent information on the actual

effects of irradiation. This is illustrated in Figure 21 which shows the Charpy transition curves of F82H irradiated between 60°C and 450°C. As it can be seen, the upper shelf plateau seems unaffected by irradiation. It indicates also that it is independent of irradiation temperature. The ductile–to–brittle transition temperature does not depend on the irradiation temperature in a consistent manner. On the other hand, a consistent picture is obtained if the general yield strength is used to monitor irradiation effects. This is illustrated in Figure 22 obtained on F82H irradiated at 300°C but unfortunately many data were missing. Nevertheless, these two figures illustrate the importance of analyzing multiple– rather than single– property data to get a global picture of the effects of irradiation. Another illustration is given in Figures 23 and 24 on F82H irradiated at 300°C to various neutron doses. The Charpy impact data on various 9%Cr–steels reported by Schneider et al. [172-173] and Rieth et al. [282-283] were systematically analyzed and are shown in Figures 25.a to 25.f. Details on the determination of the dynamic yield strength can be found in [172-173, 282]. Despite the large scatter, the right hand pictures representing the variation of the general yield strength with temperaure are more consistent than the left hand side pictures depicting the variation of absorbed energy as a function of temperature.

In Figure 26, the correlation between the embrittlement (measured by the DBTT) and hardening (measured by the general yield strength) exhibits a large scatter and clearly show the difficulty of modeling to reproduce such results.

As a matter of fact, we will consider in the following only tensile data, namely the yield strength, and all other data, in particular Charpy impact data, will be used only as a support. Thus, the experimental database will be exclusively based on tensile data. However, another difficulty appears as all tests are not performed at the same temperature and this will be analyzed hereafter.

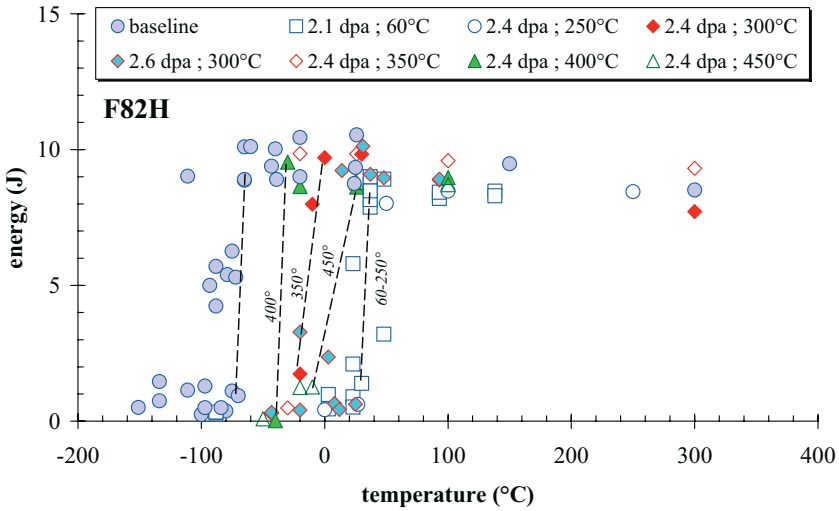

Figure 21. Illustration of the difficulty of DBTT–determination in the unirradiated and irradiated conditions (F82H steel) [173].

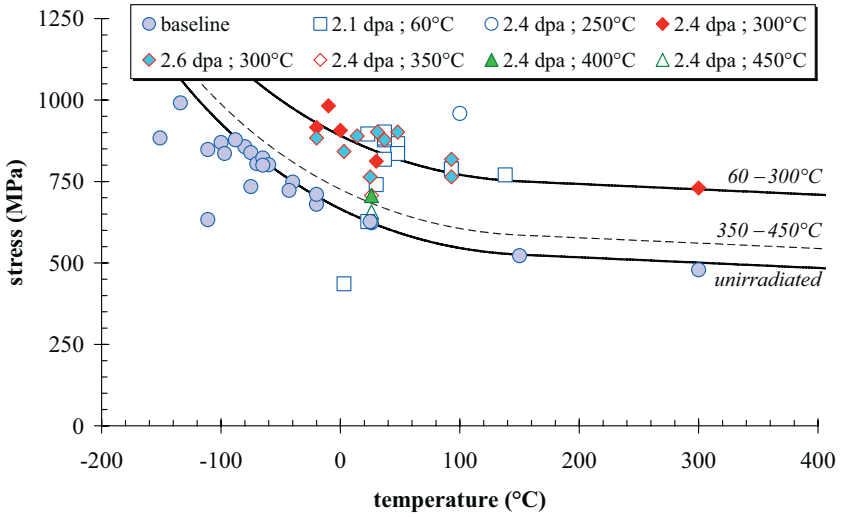

Figure 22. Same tests as Figure 21 but represented by the general yield strength [173].

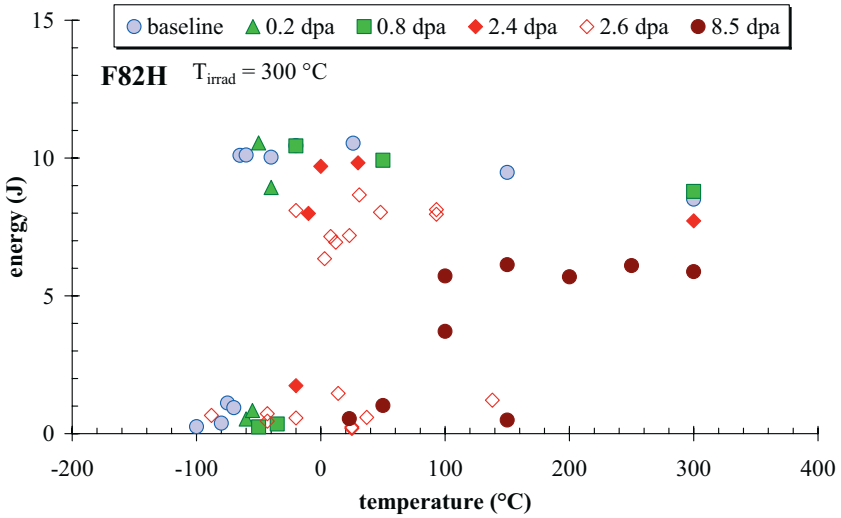

Figure 23. Effect of neutron dose on the Charpy impact transition behavior of F82H irradiated at 300°C.

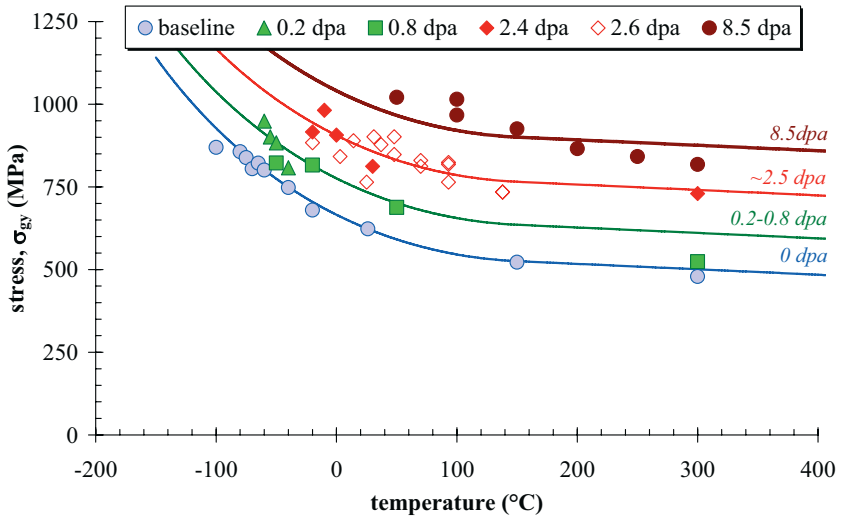

Figure 24. Derivation of the irradiation hardening from the instrumented Charpy impact data of Figure 23.

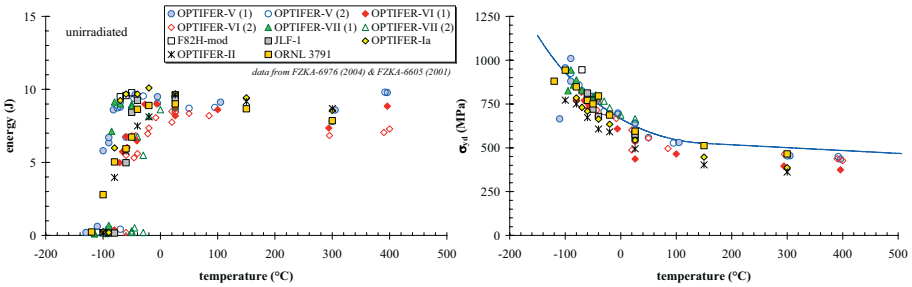

Figure 25.a. Charpy impact energy transition behavior and associated general yield stress: unirradiated condition.

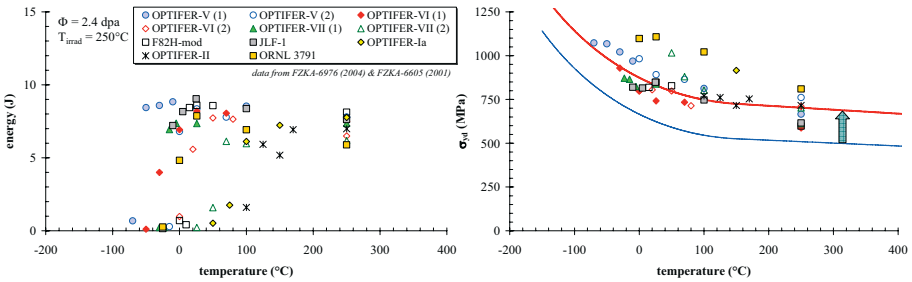

Figure 25.b. Charpy impact energy transition behavior and associated general yield stress: irradiated condition Φ=2.4 dpa; T_{irrad} = 250°C.

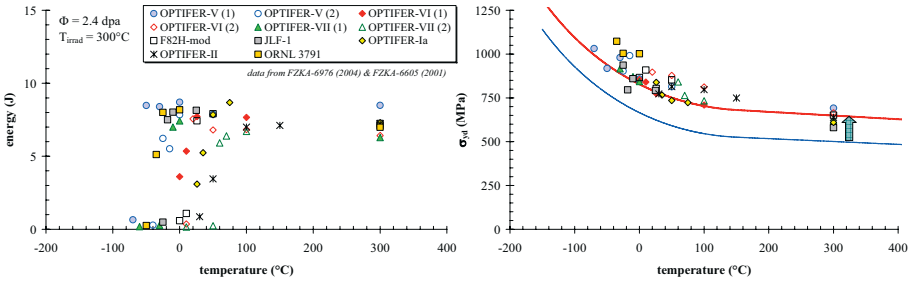

Figure 25.c. Charpy impact energy transition behavior and associated general yield stress: irradiated condition Φ=2.4 dpa; T_{irrad} = 300°C.

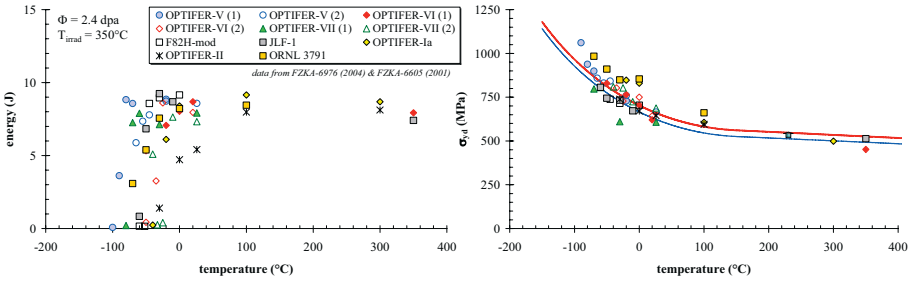

Figure 25.d. Charpy impact energy transition behavior and associated general yield stress: irradiated condition Φ=2.4 dpa; T_{irrad} = 350°C.

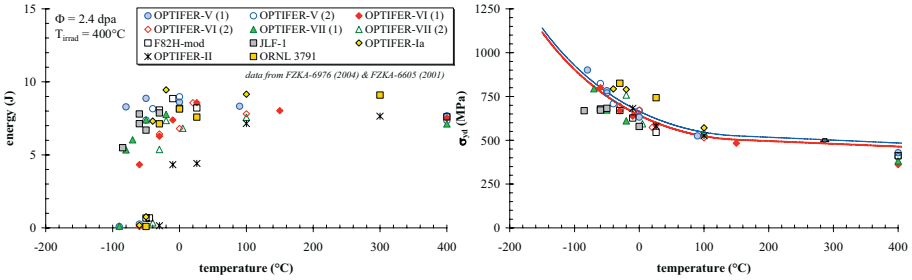

Figure 25.e. Charpy impact energy transition behavior and associated general yield stress: irradiated condition Φ=2.4 dpa; T_{irrad} = 400°C.

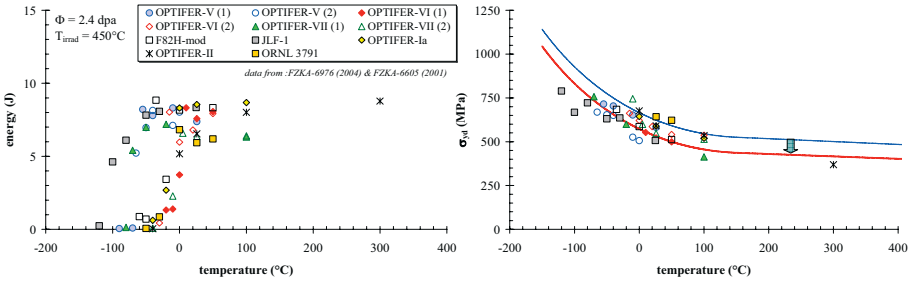

Figure 25.f. Charpy impact energy transition behavior and associated general yield stress: irradiated condition Φ=2.4 dpa; T_{irrad} = 450°C.

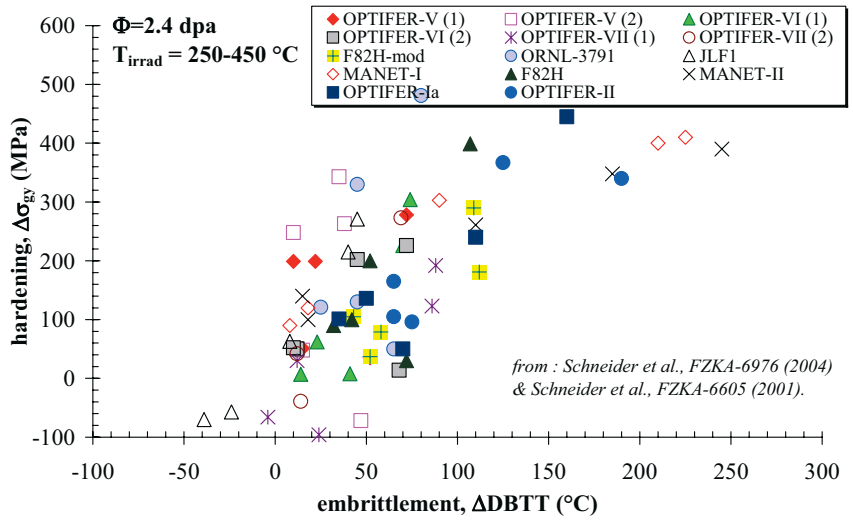

Figure 26. Correlation between the yield strength change and tensile strength change.

4.3. Test temperature effect on irradiation–hardening

In practical applications, tensile tests that are reported in literature are very often performed either at room temperature (~25°C) or at the irradiation temperature. There are only few cases where tensile tests were performed in a large temperature range. Therefore, to be consistent when comparing irradiation hardening values obtained at different temperatures, it is necessary to perform a kind of normalization procedure to consistently analyze the data.

As indicated in chapter II, deformation is a thermally-activated process described by equation (3). This equation indicates that the athermal component varies with the test temperature because the Young's modulus variation with temperature. In a first step, the yield strength should be corrected to remove the effect of the Young's modulus. If the

yield strength in the athermal range is plotted as a function of test temperature, Figure 27 indicates that the slope of the trend line is approximately $\alpha \approx 5.3\ 10^{-4}\ K^{-1}$, which is significantly higher (about twice) than the Young's modulus slope ($\alpha \approx 2.76\ 10^{-4}\ K^{-1}$). This means that another phenomenon is concurrently reducing the yield strength and this will be discussed next..

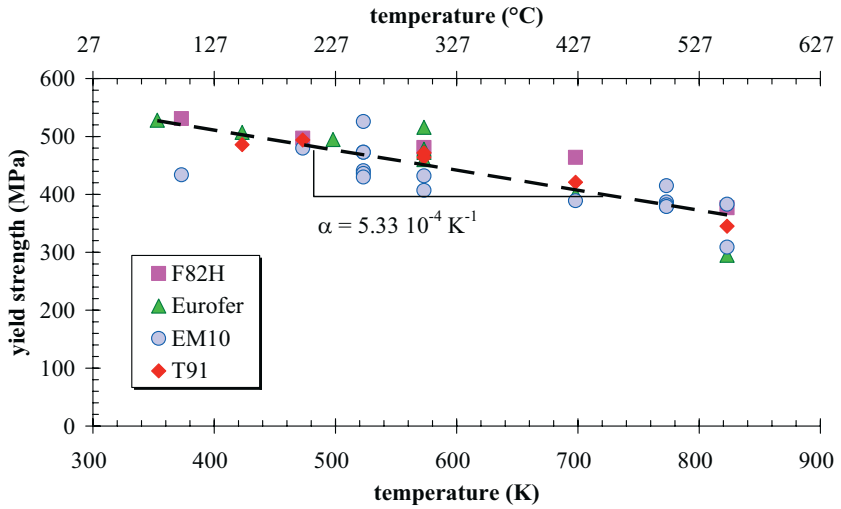

Figure 27. Effect of test temperature on the yield strength of 9%Cr–steels.

It is also interesting to examine some available experimental data on the effect of test temperature on irradiation hardening. To illustrate the effect of test temperature on irradiation hardening, the data were normalized to the increase of the yield strength at room temperature. The results are shown in Figure 28. As it can be seen, within the temperature range under consideration, there is a linear decrease of the normalized yield strength change with test temperature. The measured slope of this curve indicates $\alpha \approx 5.5\ 10^{-4}\ K^{-1}$, a value which is in close agreement with Figure 27. So, both experimental data sets shown in Figures 27 and 28 indicate a linear decrease with a constant slope, approximately twice the usual Young's modulus temperature slope. As a matter of fact, at high temperature, the measure of the yield strength at quasi-static strain rates (of the order of $10^{-4}\ s^{-1}$) may be affected by the anelastic deformation. There is experimental evidence that in the high temperature range, Young's modulus measured dynamically using ultrasonic waves lead to higher values than when derived from tensile tests [284]. Sawada et al. [284] reported Young's modulus data measured with two methods, namely ultrasonic pulse method versus classical tensile test. The reported data are in close agreement with other published data and trend curves [3, 134, 285-286]. While good agreement between the two methods is observed at low temperature, both methods deviate in the high temperature range (see Figure 29). The illustration shown in Figure 29 shows how the anelastic deformation can bias the Young's modulus measurement during a tensile test. Young's modulus as measured in a tensile test is actually affected by the

loading rate as a result of the combination of the elastic and anelastic strains [287]. An estimate of the contribution of the anelastic deformation can be made based on experimental data obtained on both Young's modulus and yield strength.

Experimental data show that the slope of the temperature dependence of the yield strength is roughly twice the slope of the temperature dependence of the Young's modulus, as obtained on other independent data.

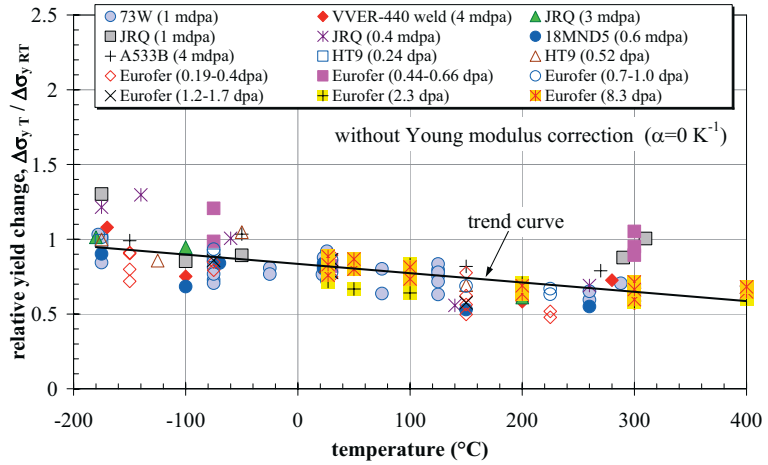

Figure 28. Effect of test temperature on the irradiation hardening (yield strength change).

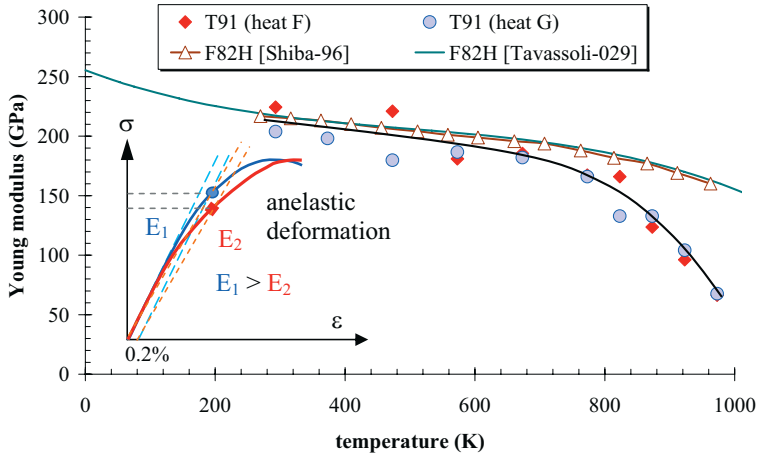

Figure 29. Young's modulus measurement as a function of temperature using both tensile testing and ultrasonic method. The large discrepancy above 600K can be attributed to anelastic deformation. Data from Shiba et al. [286] were obtained using the ultrasonic method.

It is very interesting to observe that if the ultimate tensile strength change rather than the yield strength change is considered, Figure 30 is obtained. This Figure is similar to Figure 28 except that the yield strength is replaced by the tensile strength. The ultimate tensile strength does depend neither on the Young's modulus nor on the anelastic strain and that's what Figure 30 shows. This clearly supports that above mentioned explanation, i.e., the anelastic deformation and the Young's modulus temperature dependence do not enter into account when dealing with tensile strength.

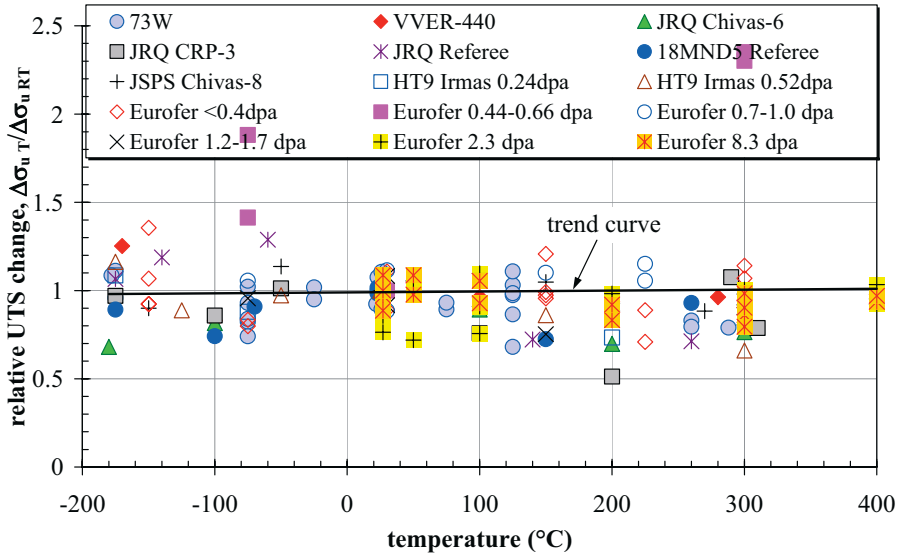

Figure 30. No effect of test temperature on the radiation–induced change of the tensile strength.

In the following, the normalization procedure is developed. From an engineering point of view, the engineering yield strength is usually evaluated at a fixed plastic strain of 0.2% (ε_y=0.002). At a specific strain rate, the Hooke equation allows to write:

$$\sigma_y(T) = E(T) \times \varepsilon_y = (1 - \alpha T) \times E_0 \times \varepsilon_y \qquad (10)$$

Here E is the Young's modulus, T is the temperature and ε_y is the elastic strain.

However, if anelastic deformation occurs, then this relation changes to:

$$\sigma_y(T) = E(T) \times \varepsilon_y(T) \qquad (11)$$

where the strain ε_y, assumed to be linearly dependent on temperature, is given by:

$$\varepsilon_y(T) = (1 - \beta T) \times \varepsilon_{y\,0} \qquad (12)$$

Equation (10) can be re-written as:

$$\sigma_y(T) = E(T) \times \varepsilon_y(T) = (1 - \alpha T) \times E_0 \times (1 - \beta T) \times \varepsilon_{y\,0} \qquad (13)$$

this can be approximated by:

$$\sigma_y(T) \approx \left[1-(\alpha+\beta)T\right]\times E_0 \times \varepsilon_{y\,0} \qquad (14)$$

In our evaluation, α is taken equal to 2.76 10^{-4} s^{-1} and (α+β) equal to 5.5 10^{-4} s^{-1}.

Thus, the normalized yield strength increase can be written as:

$$\Delta\sigma_y^{RT} \approx \frac{1-\alpha' T_{RT}}{1-\alpha' T}\times\Delta\sigma_y^{T} \qquad (15)$$

where:
$$\begin{cases} \alpha'=2.67\ 10^{-4}\ \mathrm{K}^{-1} & \text{if} \quad T \le RT \\ \alpha'=5.5\ 10^{-4}\ \mathrm{K}^{-1} & \text{if} \quad 600°\mathrm{C} > T > RT \end{cases} \qquad (16)$$

For example, after irradiation, if the measured hardening obtained by testing at T=300°C is $\Delta\sigma_y^{T} = 100\ MPa$, the estimated hardening if the test was done at room temperature (T_{RT}=25°C) would be $\Delta\sigma_y^{RT} = 134\ MPa$ MPa.

Application of the preceding normalization procedure to the data of Figure 28 leads to the horizontal line shown in Figure 31. Another support of this methodology is given by the tensile test data obtained on Eurofer-97 irradiated to various neutron doses and tested in the range of -150 °C to +300°C [130]. The results in terms of yield strength increase as a function of neutron dose are depicted in Figure 32 where both as tested (at the test temperature) and after T-correction data are shown for comparison. The correction procedure outlined above applied to the data (blue dots) shown in Figure 32 clearly shows that the scatter is much reduced (red diamonds).

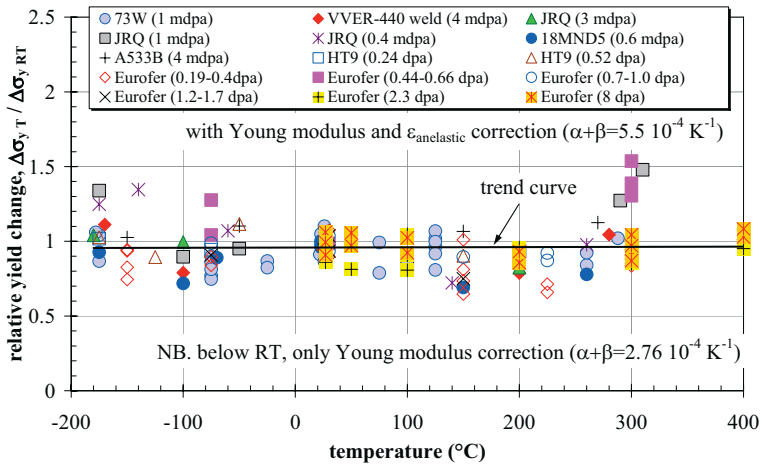

Figure 31. No effect of test temperature on the irradiation hardening after both Young's modulus and anelastic deformation correction.

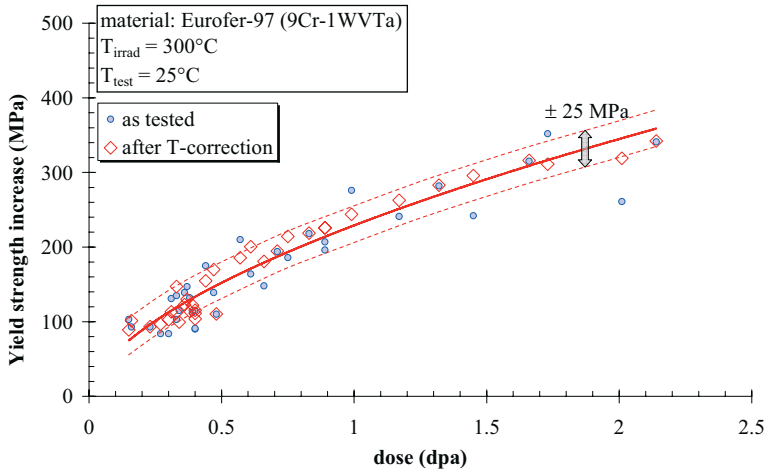

Figure 32. Effect of the test temperature correction on Eurofer-97 irradiated at 300°C showing the reduction of the scatter after temperature correction.

4.4. Conclusion

The following conclusions can be drawn from the available experimental database. First of all, the available data do not allow separating the various 9%Cr–steels as their properties and behavior are quite similar. Moreover, there is not a single material that was investigated from all point of views. In other words, we are obliged to include in the database various 9%Cr–steels (about 30 heats) to have relevant ranges of variables. The database consists essentially of tensile data. The Charpy impact data were discarded because they may bias the actual irradiation effects. Moreover, from a modeling point of view, tensile test data are more appropriate than DBTT data. Because all tensile tests were not performed at the same temperature, a normalization procedure was used to estimate the radiation hardening at any temperature by taking into account the variation of the Young's modulus with temperature and the anelastic deformation that occurs at high temperature.

Note that yield strength increase data shown in this report were all normalized to room temperature using equation (15). This means that small differences are expected with published data as the latter correspond to the value at the test temperature.

V. RADIATION DAMAGE MODELING

5.1. Description of the model

It is important to emphasize here that the model is first kept relatively simple given the large number of parameters and variables that should normally be taken into account. The model should be step by step updated only when necessary. Basically, only two distinct damage mechanisms related to atomic displacement damage and transmutation [288] will be considered:

1. The dpa–related damage associated with defects involved in atomic displacements during neutron bombardment. This includes mainly point defect clusters (enriched with solute atoms) and loops (mainly interstitial–type loops [6, 12, 251]).
2. the He–related damage due to helium generation. This includes mainly bubbles primarily filled with He.

For both components, we will consider the dispersed barrier hardening model to begin with as it can be easily related to the irradiation–induced features that are responsible of the observed hardening. The model assumes randomly distributed obstacles to dislocation motion and assumes that the increase of the stress required to overcome these obstacles is a function of their density (number density), their size (average obstacle size) and their strength, as schematically illustrated in Figure 33.

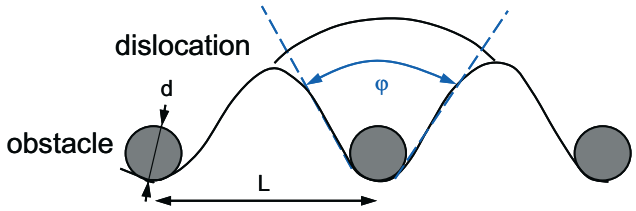

Figure 33. Dislocation – obstacle interaction.

The yield strength increase can be written as:

$$\Delta\sigma_y^d = \alpha_d \, M \, G \, b \sqrt{N_d \, d_d} \tag{17}$$

where α_d is the obstacle strength equal to 0.1 – 1 [14, 17, 20, 97, 243, 289-290], M is the Taylor factor ($M \approx 3.06$ [291]), G is the shear modulus, b is the Burgers vector, d_d and N_d are the size and number density of the obstacles, respectively.

Contrary to the dispersed hardening model which is more appropriate for strong obstacles, according to Zinkle et al. [292], an alternative model due to Friedel-Koupa-Hirch was more appropriate for weak obstacles.

$$\Delta\sigma_y^d = \frac{1}{8} M\ G\ b\ d_d \sqrt{N_d} \qquad (18)$$

However, inserting numerical values (M = 3.06, G = 85 GPa, b = 0.254 nm) together with microstructural data ($d_d \approx 1 - 10$ nm and $N_d \approx 1\ 10^{21} - 5\ 10^{22}$ m^{-3}) and comparing with measured yield strength increases does not support such an equation. Therefore, most of the irradiation defects can probably be considered as strong obstacles.

The dispersed barrier hardening model was used by many investigators when microstructural data were available [20, 77, 246, 293-294]

5.1.1. dpa–component

First of all, the change of the mechanical properties (hardening and embrittlement) is the result of the microstructural changes that occur in the material under neutron exposure. Under high energy neutron irradiation, the vacancies and interstitials that are formed have the major effect on these steels [83]. Ideally, to reliably assess the change of the mechanical properties of structural materials under both dpa and helium damage, it is essential to characterize the microstructural changes and determine their evolution with neutron fluence. If the nature, the size and the number density of the various irradiation defects are known as a function of the irradiation conditions, it would have been possible to model the combined effect on the mechanical properties using for example the dispersed barrier hardening theory. Unfortunately, availability of such data is illusive, as it was for other materials (ferritic steels for example). Moreover, some of the microstructural features are too small to be resolved. Therefore, the very few microstructural data found in literature will be used only as a support. Another alternative, pioneered by Pachur [295-297] uses annealing studies to derive the various irradiation mechanisms that are classified according to their activation energy [297-299]. Unfortunately, such annealing studies are not available to perform such an evaluation. Therefore, another route that will be detailed here after should be taken to build the model.

There are a number of features reported in literature on the nature and sometimes on their distribution (size, number density) of radiation defects. However, a clear identification of all the defects responsible of the observed change of the mechanical properties is still lacking. The difficulty stems mainly from the defect resolution related to their nano size level. Actually, only a combination of multiple examination techniques can overcome this difficulty. Nevertheless, so–called black dots, point defect clusters, small interstitial loops, cavities (voids, bubbles), radiation–induced precipitates are usually reported in literature [12, 97, 117, 142, 174, 222, 251, 300-301]. We cannot reasonably develop a model if all these defects are considered because the number of parameters to be determined would drastically increase and consequently additional empirical constants will be required. This is the reason why in a first stage, only one dpa – component is considered.

The dpa–component is due to dpa damage, consisting of point defect clusters evolving into small loops, probably interstitial loops at higher dpa levels. Their size and number

density that are reported in literature are in the range of 1 – 10 nm or larger and ~10^{21} – few 10^{22} m^{-3}. Their density decreases with increasing irradiation temperature.

The parameter that primarily governs the radiation hardening is the number density of the defects. Therefore, from equation (17), the yield strength increase can be approximated by:

$$\Delta\sigma_y^d \approx C\sqrt{N_d} \approx C\sqrt{\Phi} \tag{19}$$

where the constant C depends on the material and the irradiation conditions, more specifically, the irradiation temperature. The number density of defects is taken proportional to the neutron fluence. Such a relation, equation 5, would lead to a tremendous hardening for high dpa levels which is not observed experimentally. Indeed, before irradiation, the vacancy concentration is usually in thermal equilibrium with the lattice. Radiation hardening cannot increase indefinitely but reaches a saturation value when the rate of defect production is balanced by the annihilation rate reaching a steady state defect concentration. Consequently, another form of fluence dependence due to Whapham and Makin [302] can be used:

$$\Delta\sigma_y^d \approx C\sqrt{1-\exp\left(-\frac{\Phi}{\Phi_0}\right)} \tag{20}$$

where Φ_0 is a constant.
Note that at low dpa – levels, both preceding equations are equivalent.

To define the kinetics that controls the temperature dependence of the radiation damage (dpa–component), the annealing (recovery) will be used. If the recovery mechanism is assumed to be mainly driven by the escape of vacancies from the zones, an Arrhenius law type of kinetic can be expected [303-305]. It is known that annealing studies are the appropriate test to investigate the main defects responsible for hardening and embrittlement [297]. As a result, the defects are classified according to their activation energies for annealing. Unfortunately, such studies are missing for the 9%Cr-steels. However, it is possible to provide a physically–based trend curve that accounts for the temperature dependence. So, an approximation can be obtained by combining the various mechanisms to obtain a single effective mechanism as illustrated in Figure 34. An example of application is illustrated in Figure 35, where four annealing mechanism kinetics can be described by a single effective activation energy which represents the total annealing behavior [305].

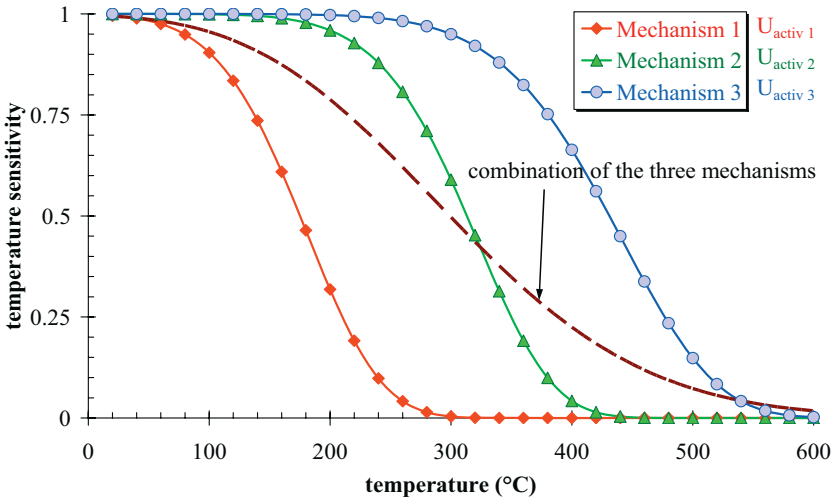

Figure 34. Illustration of combining three annealing mechanisms to obtain an effective one.

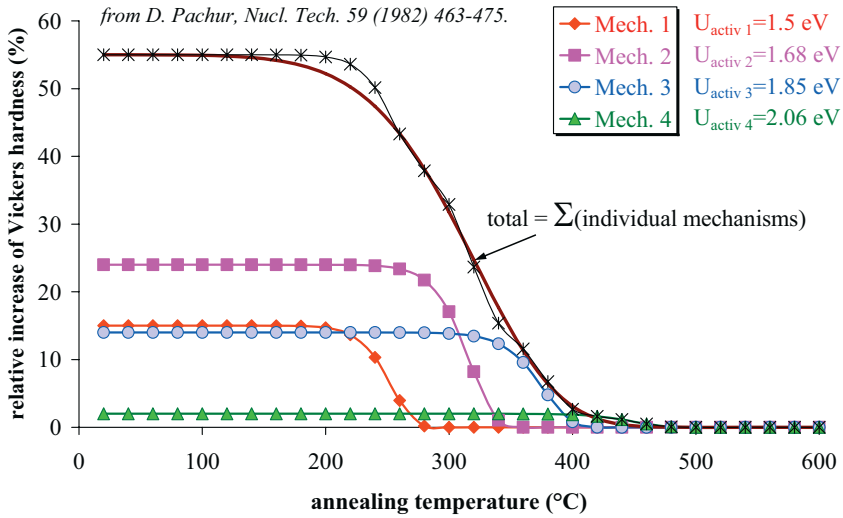

Figure 35. Annealing mechanisms according to their activation energy. Data were taken from [297].

It is known that removal of defects upon post–irradiation annealing follows a simple activation or Arrhenius type law [305]:

$$\frac{1}{\tau} = A \exp\left(-\frac{\Gamma}{k\,T}\right) \tag{21}$$

where Γ is the activation energy for recovery, τ is the recovery time, k is the Boltzman constant and T is the absolute temperature. The lower the temperature the higher is the lifetime of a vacancy. This means that at low temperature, the steady-state vacancy concentration is higher and therefore leads to a higher hardening and embrittlement [306].

It is usually assumed that the fractional variation of the hardening recovery, f, follows a differential equation of the type [303-304, 307]:

$$\frac{df}{dt} = -k_T\, f^n \tag{22}$$

where:

$$k_T = k_0 \exp\left(-\frac{\Gamma}{k\,T_{irrad}}\right) \tag{23}$$

For a first–order kinetics, $n=1$, simple integration leads to the following equation:

$$\frac{f}{f_0} = \exp\left[-k_0\, t \exp\left(-\frac{\Gamma}{k\,T_{irrad}}\right)\right] \tag{24}$$

The irradiation temperature sensitivity factor, F_T, can be written as:

$$F_T \approx \exp\left[-\nu \exp\left(-\frac{\Gamma}{k\,T_{irrad}}\right)\right] \tag{25}$$

where Γ is the activation energy and ν is a frequency factor [308]. A number of tensile test data, shown in Figure 36, were selected to determine these constants. Three types of data were selected:

1. specimens irradiated at low temperature (≤60°C) and tested at increasingly higher temperatures (the annealing time corresponds to the holding time at constant temperature before testing [144, 158, 279];
2. specimens implanted with He at constant dpa and He–content where only the implantation temperature is varied [164, 309];
3. specimens irradiated and further annealed [174, 281].

The annealing data are shown on Figure 36 where the relative temperature sensitivity factor, F_T, is calculated by normalizing the observed relative irradiation hardening with respect to its initial as–irradiated condition. For example, if a specimen irradiated at 25°C exhibits a hardening of 150 MPa, after annealing at increasingly higher temperatures, the measured hardening is divided by 150 to obtain the relative temperature sensitivity, F_T. This way, the sensitivity factor is between 0 and 1. The average value is used as a reference when several specimens are available; this explains why some data points lie above 1 or below 0 (not indicated). Above about 450°C, the temperature sensitivity is negligibly small and this is supported by literature data [21, 289]. As it can be seen,

despite the large scatter, the data can be reasonably well fitted with equation (25). However, as will be seen later, this fit (T1–dependence) is not consistent with the database which suggests a dependence according to the dashed curve (T2–dependence) shown in Figure 36.

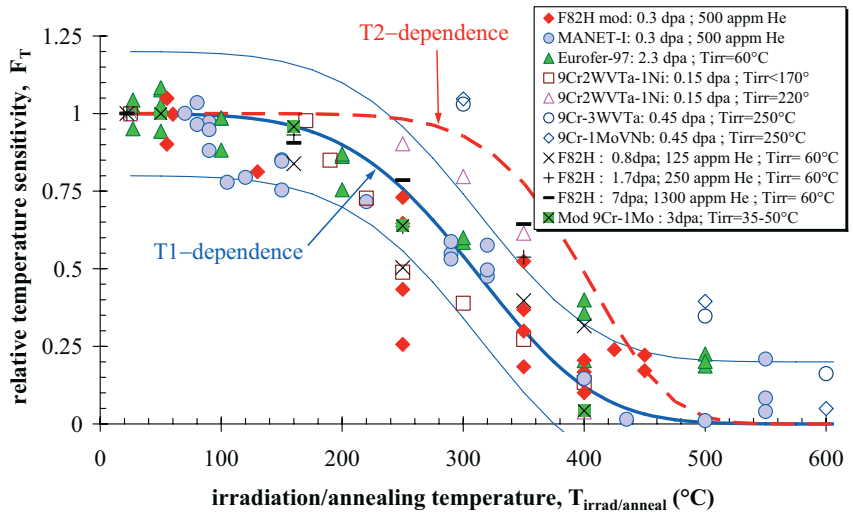

Figure 36. Irradiation temperature dependence of dpa–damage. The dashed curve is more consistent with the experimental database (see later). Experimental data taken from [144, 164, 174, 279, 281, 309].

Other data such as those of Alamo et al. [310] agree with such a T2–dependence trend curve. However, some literature data are also in disagreement with Figure 36 such as [311] where proton irradiation data indicated an important hardening around room temperature (126 and 246 MPa for 0.37 and 0.93 dpa, respectively) and negligibly small when irradiated at 250°C (7 and 27 MPa for 0.30 and 0.75 dpa).

Actually, during annealing, one can distinguish between various activation energies corresponding to the various mechanisms. However, given the large uncertainties inherent to the available experimental data, only one activation energy is considered.

So, the yield strength increase due to displacement damage can be written as:

$$\Delta\sigma_y^{dpa} \approx C_{dpa} \times \exp\left[-\nu \exp\left(-\frac{\Gamma}{k\,T_{irrad}}\right)\right] \times \sqrt{1-\exp\left(-\frac{\Phi}{\Phi_0^{dpa}}\right)} \qquad (26)$$

The constant C_{dpa} can be fixed on one single experimental condition and should remain constant for all other situations.

5.1.2. He–component modeling

The second damage component that is considered is the He–component. In literature, He–bubbles induced by transmutation (n,α) reactions indicate bubble size and number density that are in the range of 1 – 3 nm or larger at higher temperatures and ~10^{21} – few 10^{23} m^{-3}.

To model the hardening induced by He–bubbles, we considered the work of Trinkaus [312] on the kinetics of bubble formation at intermediate temperatures ($0.2<T/T_m<0.5$ corresponding roughly to 50–600°C, T_m being the melting point in K). Actually, the re–solution of gas from bubbles during irradiation was first postulated and further experimentally verified to explain the fission gas release behavior in UO_2 nuclear fuel [313]. Experimental evidence of irradiation–induced re–solution of gas atoms from bubbles in other solids was given by Evans as well [313]. Trinkaus [312] developed an analytical description of both the nucleation of bubbles under internal He–generation (primary He–bubbles) and the gas re–solution from existing bubbles (secondary bubbles). A number of simplifications were considered in developing this analytical description. In particular, it was assumed that the di–He clusters form already a stable bubble nucleus. Moreover, it was assumed that a certain fraction of He–atoms in a bubble is re–solved per dpa. The derived bubble density and size representing the upper and lower bound estimates are:

$$N = \left(\frac{\Omega}{48\pi^2 v}\right)^{2/m} \times \left(\frac{aP}{\Omega D}\right)^{3/m} \times \left(\frac{P}{\kappa K}\right)^{1/m} \kappa K t \tag{27}$$

and

$$R = \left(\frac{27 v^3 D P}{4\pi\Omega^2 a \kappa^2 K^2}\right)^{1/m} \tag{28}$$

where N is the number density of He–bubbles (m^{-3})

R is the bubble radius (m)

P is the helium production rate (s^{-1})

K is the displacement rate, or dpa rate (s^{-1})

κ is the resolution efficiency factor (-)

v is the volume per atom gas in the bubbles (m^3)

Ω is the volume per matrix atom (m^3)

$a = \frac{8\pi r_0}{\Omega} \approx 10^{21} m^{-2}$ where $r_0 \approx 0.5$ nm is the clustering radius

D is the diffusion coefficient ($m^2 s^{-1}$)

m is a constant (m=7) characterizing the time dependence of N ($N \sim t^{1/7}$).

Details can be found in [312] and therefore the same notations were taken.

As for the dpa component, by using the dispersed barrier hardening model, the following He–induced yield strength increase component can be obtained:

$$\Delta\sigma_y^{He} \approx C_{He} \times \left\{\beta\left(\dot{\phi} \times \left(He/dpa\right)\right)^{m-2} / \dot{\phi}^3\ D^2\right\}^{\left(\frac{1}{2m}\right)} \sqrt{\Phi - \Phi_{He}^{threshold}} \qquad (29)$$

where $\dot{\phi}$ is the dpa rate (K), (He/dpa) is the Helium–to–dpa rate (=K/P), $\Phi_{He}^{threshold}$ is the threshold dose below which no He–effect is observed, D is the diffusion coefficient ($D = D_0 \exp\left(-\frac{U_a}{kT_{irrad}}\right)$, U_a=0.93 eV is the He–migration energy, $D_0 \approx 10^{-5}$ m^{2}s^{-1} is a temperature independent constant) and β and m are constant ($\beta \approx 10^{-30}$ m^4, m=7). This equation was simplified leaving only the most important input parameters. As for the dpa–component, the amplitude, characterized by the constant C_{He} is experimentally fitted on one single condition and kept constant for all other experimental conditions.

The threshold value of $\Phi_{He}^{threshold}$ was fixed to 500 appm He. Below this threshold, the contribution of helium into hardening is marginal, in agreement with literature data [237].

It is important to note that the approximations used above and the derived equation (29) are valid only in the temperature range mentioned above, namely ~50 – ~600°C. Indeed, below ~50°C, the He–diffusion changes from the replacement mechanism to the cascade mixing mechanism [314] leading essentially to a population very small He–vacancy clusters. Above ~600°C, re–absorption of re–solved gas atoms reduces the gas resolution efficiency and thermal dissociation of gas atoms from bubbles becomes important.

5.1.3. Superposition law

In the presence of various obstacle types with different size, number density (obstacle spacing) and strength, the total hardening will be a superposition of the individual types of hardening obstacles. A realistic model should take all this information into account. However, this is practically impossible from an analytical point of view and therefore a number of simplifying approximations should be considered. Foreman and Makin [315] developed computer calculations of a dislocation moving across a random array of obstacles of different strengths that can help for estimating the appropriate superposition law to be used. A good overview of the various effects of size, density and strength distributions can be found in [316]. For simplicity, we will consider here only two simple cases that are usually used, the linear and the quadratic superposition laws. This means that the total contribution of both dpa and He to hardening can be written as [316]:

$$\Delta\sigma_{total} = \left(\Delta\sigma_{dpa}^p + \Delta\sigma_{He}^p\right)^{1/p} \qquad (30)$$

where p characterizes the superposition law that is used, p=1 for a linear superposition and p=2 for a quadratic superposition. Figure 37 illustrates for both superposition laws how the two components vary. For the same total hardening (100%), a linear superposition is suggesting for example 50% of each of the component (50%+50%=100%) while a quadratic superposition results in a higher contribution of the second component ($\sqrt{(50\%^2+86.6\%^2)}$=100%).

The computer simulations performed by Makin and Foreman suggest a better agreement of the numerical results with the quadratic superposition. This was confirmed by other simulations performed by Malerba [317]. In general, it is found that the best agreement is found by combining both laws [318]:

$$\Delta\sigma_{total} = S\times\left(\Delta\sigma_{dpa}+\Delta\sigma_{He}\right)+\left(1-S\right)\times\left(\Delta\sigma_{dpa}^{2}+\Delta\sigma_{He}^{2}\right)^{1/2} \qquad (31)$$

where 0<S<1.

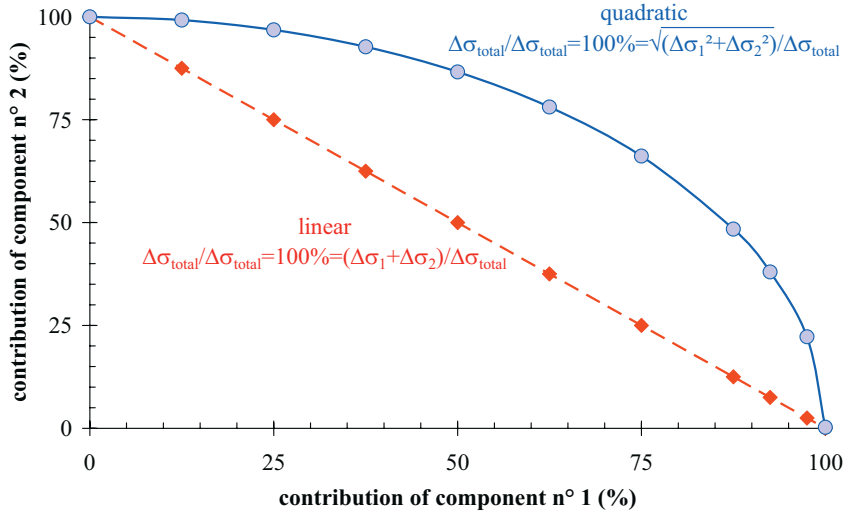

Figure 37. Relative damage component contribution according to the selected superposition law (total hardening = 100%).

This means that the appropriate superposition law lies between linear and quadratic, but probably closer to the latter. For instance, the data of Foreman and Makin [315] suggest an S value close to 0.2 (see Figure 38). From a practical point of view, the choice of the appropriate superposition law should be based on the best agreement to the experimental data. Of course, to make such an assessment of the appropriate superposition law different combinations of the amplitude of the two components are required, which unfortunately are often missing in the available experimental data. Nevertheless, both linear and quadratic superposition laws will be used in our case.

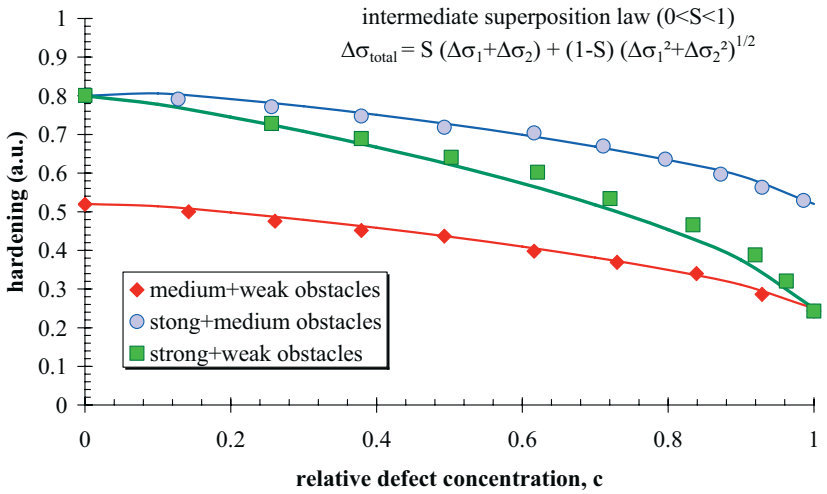

Figure 38. Intermediate superposition law applied to the numerical simulations of Foreman and Makin [315] (S=0.2).

5.2. Application

Equations (26), (29) and (30) allow determining the total yield strength increase as a function of a limited number of variables, namely, the irradiation temperature, dpa–rate, the total dpa and the He–to–dpa rate or He–rate. All other parameters (ν, Γ, λ, Φ_0, T_m, m, C_{dpa}, C_{He}) are constants. Application of this model is presented in the next section.

In the following, application of the model to a number of typical situations is provided as illustrations. First, ignoring the He–contribution, i.e., for data obtained from neutron irradiations, the hardening trend curves are given for different irradiation temperatures in Figure 39. In Figure 40, an example showing both dpa– and He– contributions for a hypothetical situation of proton irradiation at 250°C. As it can be seen, the model assumes a threshold He – content (fixed to 500 appm He) below which He–contribution is ineffective. The effect of He–generation rate on the hardening is illustrated in Figure 41. Finally, for typical fusion conditions, such as ITER, DEMO and IFMIF where the He–generation rate is close to 10, the hardening trend curves are shown in Figure 42 at various temperatures, 200 to 500°C.

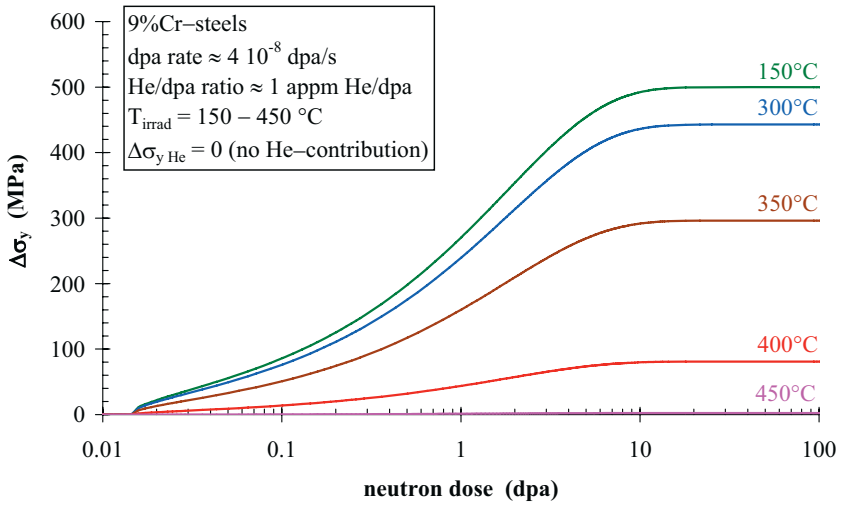

Figure 39. dpa–damage component at various temperatures when He–contribution is negligible.

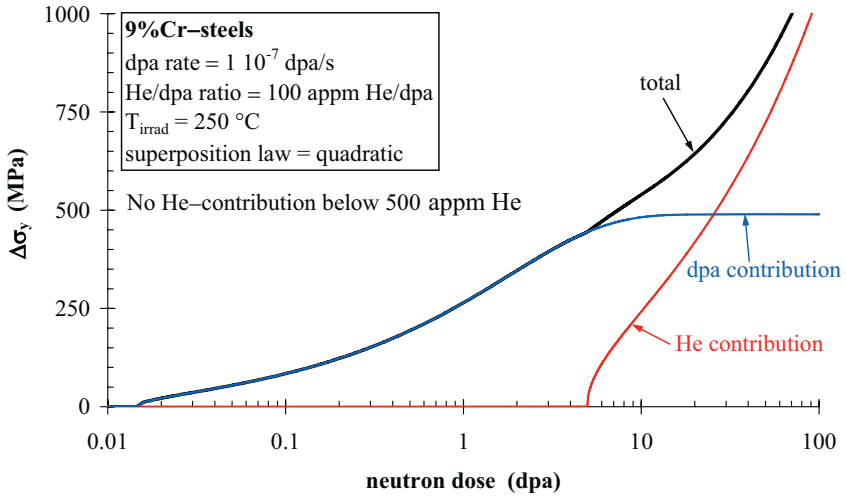

Figure 40. Application of the model to proton irradiation environment.

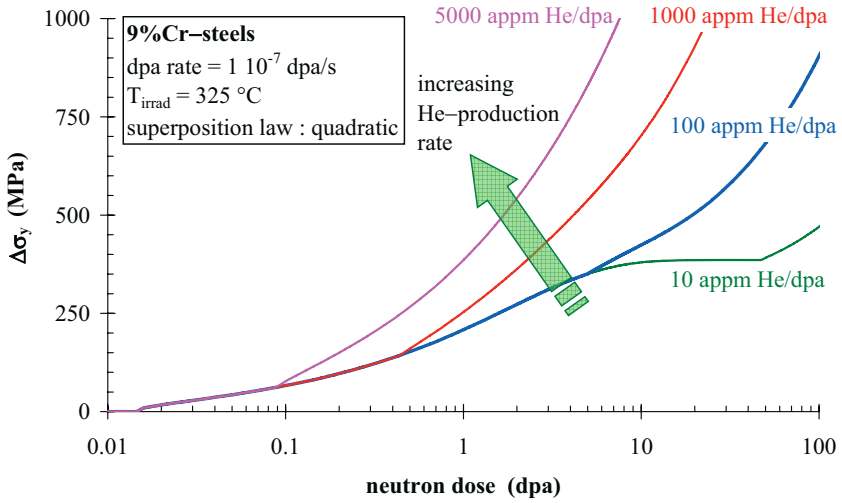

Figure 41. Effect of He–generation rate on the hardening kinetics at 325°C.

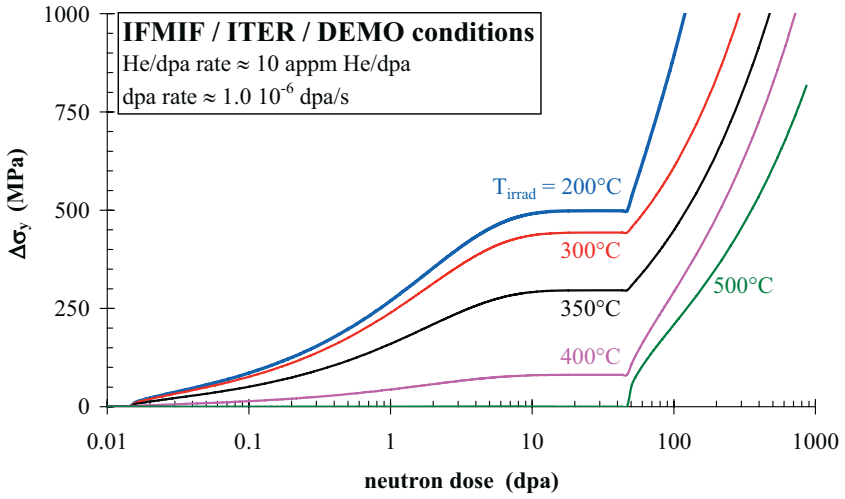

Figure 42. Predictions of the model for fusion–relevant irradiation conditions at various temperatures.

5.3. Conclusion

It is important to emphasize that the model presented in this section was voluntarily kept as simple as reasonably possible to allow an analytical description of radiation hardening including He, of 9%Cr–steels in the temperature range of 50 to 600°C. One of the main reasons for this simplification is to keep the number of model variables to a minimum level. It is a matter of fact that each subsequent model parameter brings additional variables. Therefore, additional variables, such as chemistry, defect nature, … should be incorporated only if the deviations between the model and the experimental data cannot be rationalized.

It is important to note that a saturation of hardening due to He–damage component should also be incorporated into the model in a similar way as for the dpa–damage component. Experimlental evidence was given by Klueh et al. [83, 161] on the saturation of hardening caused by He. This saturation phenomenon was not taken into account in the version presented in this report because of the experimental data limitation. As a result, the hardening due to He will be overestimated at high dpa doses.

VI. RESULTS AND ANALYSIS

6.1. Introduction

Before analyzing the results of application of the preceding model, it is interesting to point out a few comments. It is known that one of the methods used to generate helium is through the Ni–doping. Very often, the 9%Cr–steels are doped with 1 to 2%Ni [157, 159, 194, 232, 234-236, 238, 253, 274]. Many investigators [125, 157, 161-162, 180, 194, 205, 215, 232, 234, 238, 253, 319] have extensively used this procedure to promote helium generation in 9–12 %Cr steels. However, in the temperature range below ~300°C, while indeed helium is created through the interaction of the thermal neutrons with Ni–atoms, the effect of Ni–addition on the dpa–damage is much more significant than the hardening resulting from helium [156, 164, 231, 236]. At high temperature, say above about 400°C, the Ni–contribution to hardening becomes negligible [232, 320].

To better illustrate the difficulty of using Ni for He–generation, we collected experimental data published by Klueh and co-authors [156, 159, 161, 180,205, 320-321] on the effect of Ni–doping. Figures 43, 44 and 45 show the results in terms of hardening as a function of neutron dose and He–content of 9%Cr–steels irradiated at 50°C but tested at 25°C, at 300°C tested at 300°C and at ~400°C tested at 400°C, respectively. There is no evidence of intrinsic He–induced hardening effect for the three temperatures considered here. Ando et al [235] reported data on their Figure 4 that clearly show the detrimental effect of Ni–addition on the displacement damage component. On the other hand, Ni itself could have an intrinsic effect on displacement hardening as it does in ferritic steels. Finally, Tanigawa et al. [146] suggested the possibility of Ni–enhanced M_6C phase precipitation under irradiation. Also large microstructural changes arising from Ni–precipitation complicate the interpretation of the results [274]. Therefore, all Ni–doped steels were removed from the databank.

Nickel–doping was one of the procedures that were used to increase helium–content in 9%Cr–steels. However, the observed increase of hardening and embrittlement after irradiation is believed to be attributable to displacement damage rather than helium, in particular at low temperature [156, 194, 230-231, 236]. Conclusions such as those reported by Klueh et al. [319] might be wrong. In a recent paper, Klueh et al. [156] reported microstructural observations by TEM which indicate that the irradiation–induced dislocation loops were denser and finer in the 1%Ni–doped steel with respect to the undoped steel.

Klueh et al. [232] reported no effect of helium on Ni–doped 9%Cr– and 12%Cr–steels irradiated to ~16 dpa at 390, 450, 500 and 550°C. Klueh et al. [180, 205, 319] reported data that indicate an effect of helium at 400 and 300°C but not at 500°C. This was attributed wrongly to helium and is thought to be due to enhanced displacement damage by nickel addition, as it does in ferritic steels. However, in the low temperature range, say below ~300°C, nickel is expected to play a significant role in enhancing radiation hardening [270].

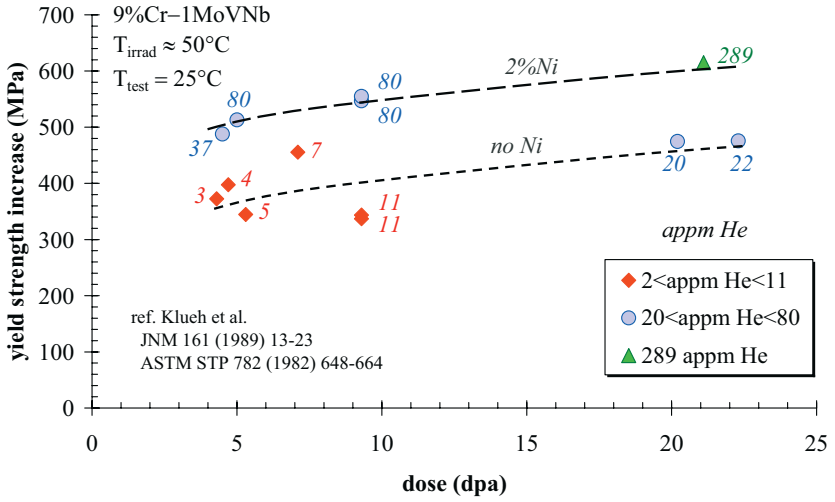

Figure 43. Helium effect (through Ni–addition) on irradiation hardening. T_{irrad} = 50°C and T_{test} = 25°C.

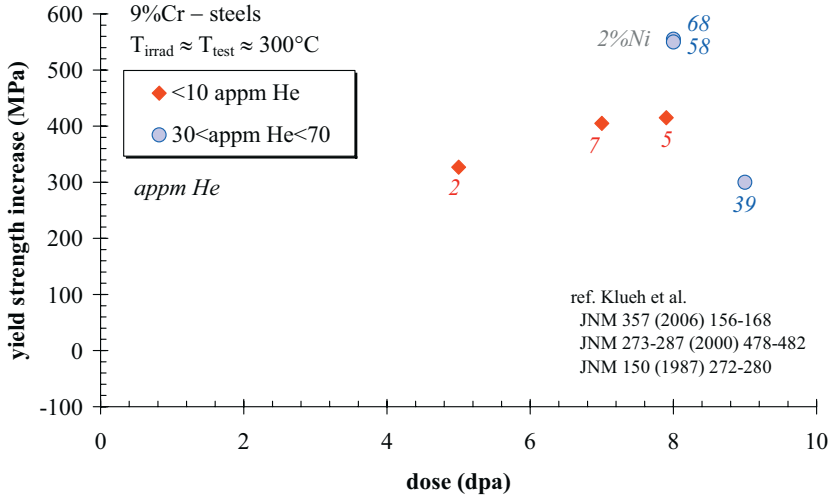

Figure 44. Helium effect (through Ni–addition) on irradiation hardening. T_{irrad} = 300°C and T_{test} = 300°C.

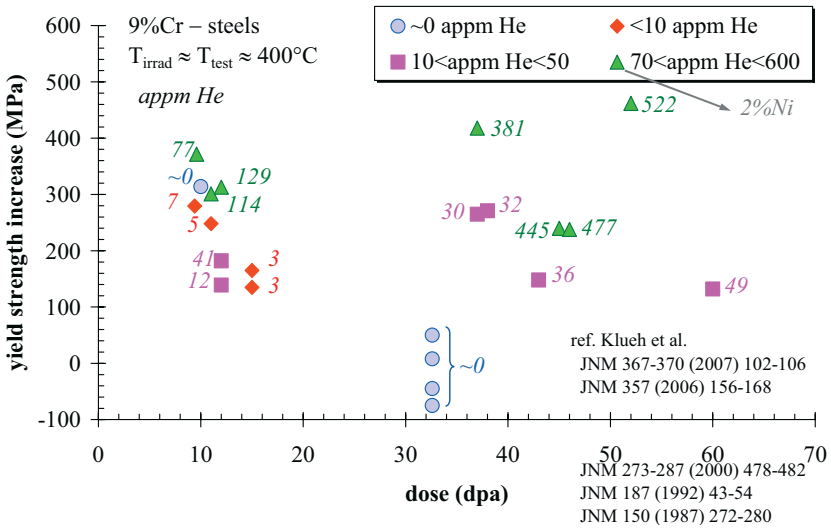

Figure 45. Helium effect (through Ni–addition) on irradiation hardening. $T_{irrad} \approx 400°C$ and $T_{test} = 400°C$.

6.2. Application of the model to the database

All experimental data were normalized to room temperature testing using equation (15). The yield strength increase as a function of the displacement damage ($\Delta\sigma_y$–dpa) taken from the database where He–content is below 1000 appm (0.1%) are shown in Figure 46. As it can be seen, despite the large scatter, there is no significant effect of temperature in the range 50 – 325 °C. A significant hardening decrease is noticed at 365°C and higher. Above about 430°C, no hardening occurs and even some softening is evidenced, in agreement with [19, 21, 99-100, 281]. The results shown on Figure 46 are not consistent with the data shown in Figure 36 (*T1–dependence*) on the irradiation temperature dependence. The reasons of this disagreement are at this stage unknown. Details on the testing conditions are necessary to identify the possible reasons. Nevertheless, if the negligible effect of irradiation temperature in the range 50 – 325°C is taken into account, the temperature sensitivity factor should be modified according to the dashed curve shown on Figure 36 (*T2–dependence*).

In Figure 47, the data where the He–production rate is about ~100 appm He/dpa are shown for various temperatures. This Figure is consistent with Figure 46 on the negligibly small effect of irradiation temperature below about 300°C. Finally, for the He–implanted specimens, the data are shown on Figure 48 confirming the absence or negligible effect of irradiation temperature effect below about 300°C.

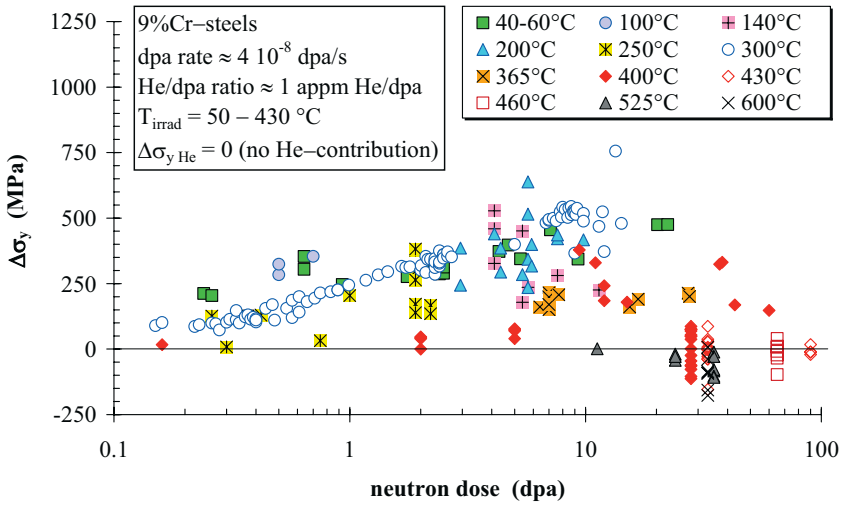

Figure 46. Experimental data for low He–content specimens (<1 appm He/dpa) for different irradiation temperatures.

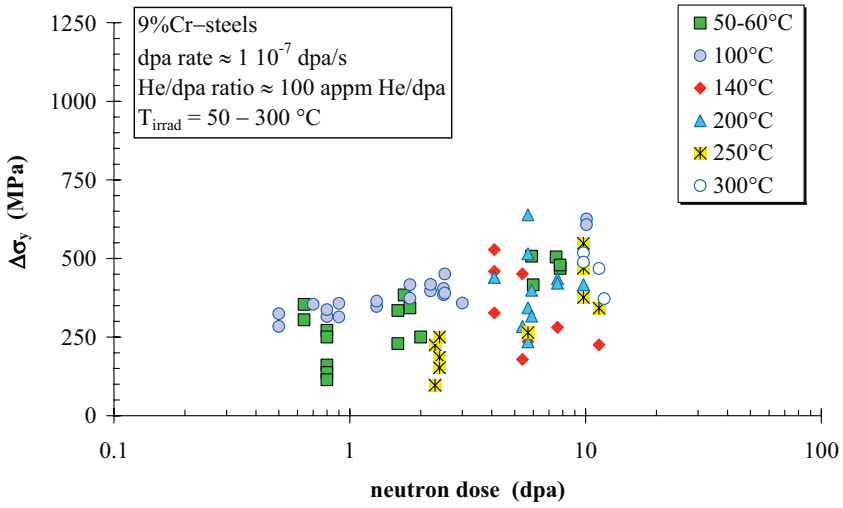

Figure 47. Experimental data for medium He–content specimens (~100 appm He/dpa) for different irradiation temperatures.

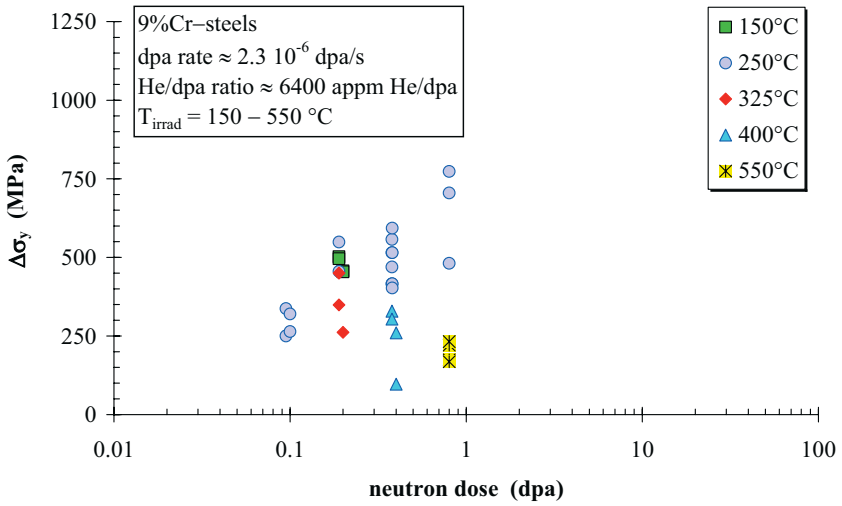

Figure 48. Experimental data for high He–content specimens (~6400 appm He/dpa) for different implantation temperatures.

It is important to notice that the experimental data where the yield strength after irradiation has decreased rather than increased cannot be correctly modeled. Irradiation softening, which occurs in the high temperature range (450 – 600°C), was indeed not incorporated in the model. Actually, an additional temperature–dependent component which reduces the yield strength should be added to account for the irradiation softening. Unfortunately, well dedicated experimental data are required to accurately account for this phenomenon. So the temperature sensitivity remains an open issue and it will be necessary to correctly take this key parameter into account before being able to reliably model irradiation effects on the whole temperature range.

Assuming a quadratic superposition law, application of the model to the database are shown in Figures 49 and 50, for the two temperature sensitivity trends shown in Figure 36. These two Figures compare the experimentally–measured yield strength increase to the predicted one using equations (26), (29) and (30). At high dpa and high He–content, the predicted hardening is significantly overestimating the experimental one (see Figure 51 for an extended scale). This was expected from the He–contribution to hardening that does not saturate. Unfortunately, the available data do not allow yet the determination of the saturation value. If the linear superposition law is adopted the whole picture does not significantly change: the scatter is too high to clearly identify possible changes.

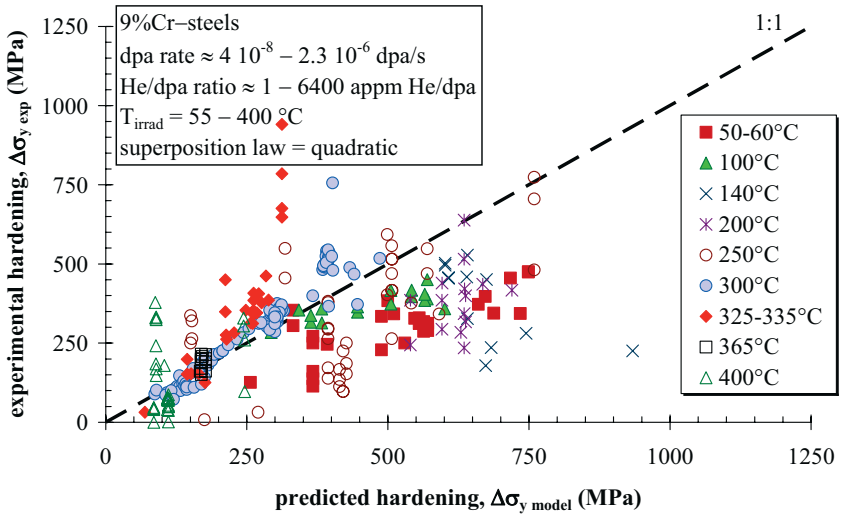

Figure 49. Comparison between experimental data and model prediction considering the irradiation temperature sensitivity dependence of the full curve (*T1*–dependence) shown in Figure 36.

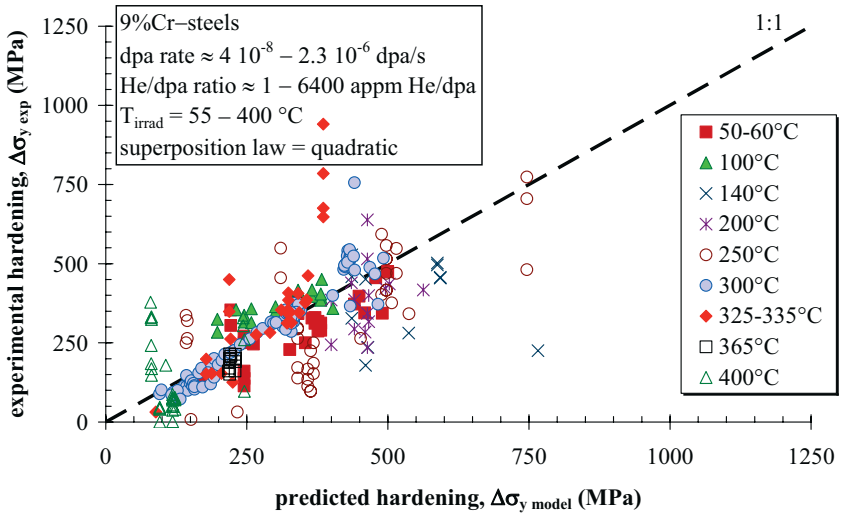

Figure 50. Comparison between experimental data and model prediction considering the irradiation temperature sensitivity dependence of the dashed curve (*T2*–dependence) shown in Figure 36.

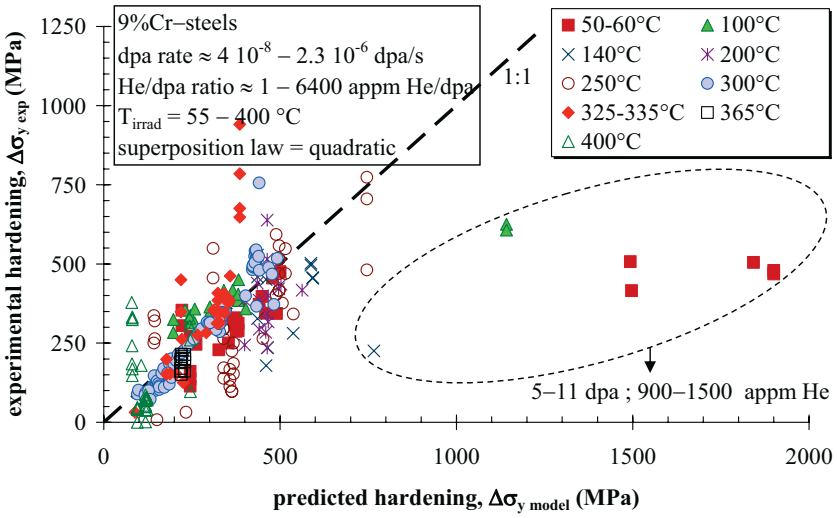

Figure 51. Similar to Figure 50, with X–axis extended. At high dpa, the model overestimates the hardening as no saturation of He–component was assumed.

It is interesting to examine the data according to the irradiation temperature and to the He–production rate. The results are shown in Figure 52 for the neutron irradiation data (where He–production rate is about 1 appm He/dpa), Figure 53 for the proton irradiation data (He–production rate is about 100 appm He/dpa) and Figure 54 for the He–implanted data (He–production rate is about 6400 appm He/dpa). As it can be seen, the model predictions are in reasonable agreement with the experimental data. These data demonstrate the possibility to extract useful information from ion irradiation, in a similar way as neutron irradiation [322-323].

Two remarks can be made on the application of the model to the available database. First, the model cannot accurately predict the hardening of 9%Cr–steels when both dpa and He–content are high. Indeed, the square root dependence of hardening as a function of dpa overestimates the actual hardening and should normally saturate above a certain He–level. Second, for high He–contents obtained by He–implantation, the concurrent dpa level does not exceed 1 dpa. It is therefore clear that the database should be updated to include data which are not considered in the present version.

Globally, the agreement between experimental and predicted hardening is reasonable if all uncertainties and adopted assumptions are taken into consideration. It should be emphasized that from an engineering point of view, a mean curve is not a must but lower/upper bounds would offer a frame for designers that they can evaluate their safety margins.

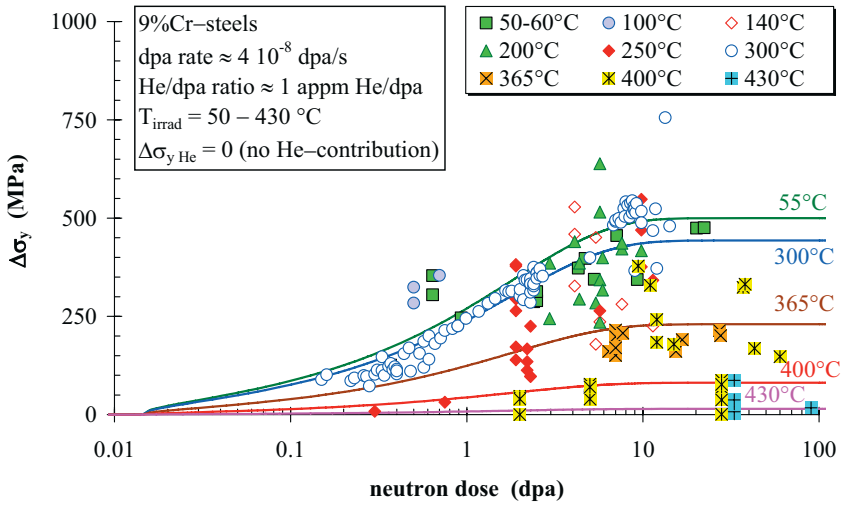

Figure 52. Application of the model to experimental data obtained from neutron irradiations in test reactors.

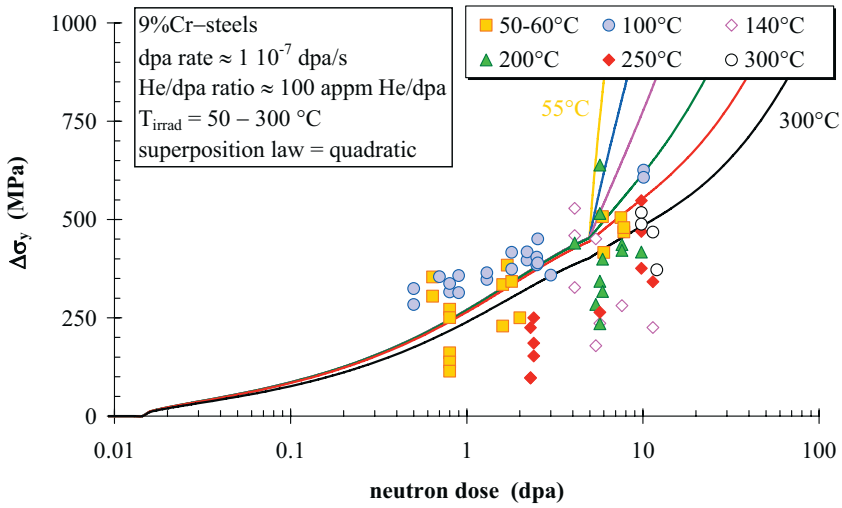

Figure 53. Application of the model to experimental data obtained from proton irradiation (He–production rate ~100 appm He/dpa).

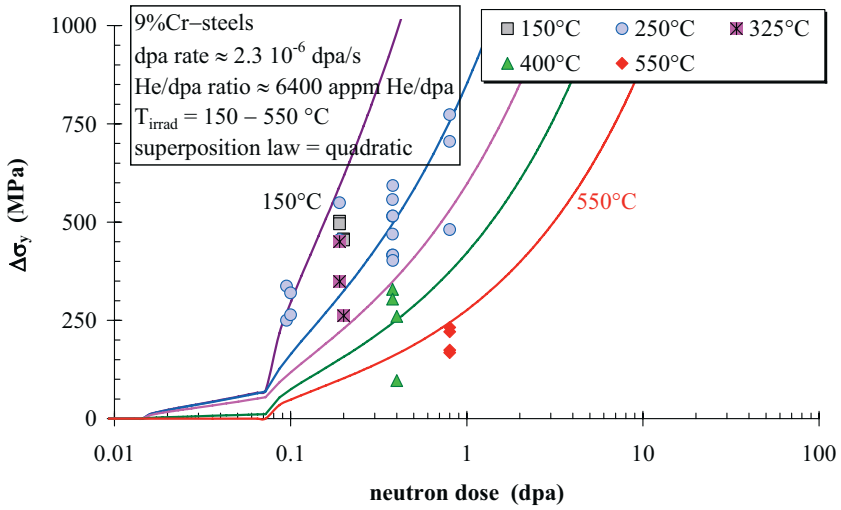

Figure 54. Application of the model to experimental data obtained from He–implantation (~6400 appm He/dpa).

It is important to mention that Ullmaier and Camus [251] attributed their hardening mainly to the displacement damage for He–concentration below 5000 appm He. This is in contradiction with the data shown in Figure 54. Some other authors attributed hardening and embrittlement to helium although the He–content was significantly lower, below 100 appm He [108]. This illustrates the still open question of the actual role of Helium in hardening and embrittlement of 9%Cr–steels.

6.3. Conclusion

Application of the proposed model to the experimental database is very promising given all the uncertainties related to the database itself and the assumptions of the model. It is clear that additional experimental data are required to better define the He–contribution. As already pointed out by Trinkaus [312], specimens should be pre-implanted before irradiation to high dose levels. It is also clear that the yield strength increase cannot indefinitely rise with He–generation and ultimately should saturate. It should also be kept in mind that it is possible that such saturation could be accompanied by a reduction of the microcleavage fracture strength which would affect thereby the relationship between hardening and embrittlement.

VII. DISCUSSION

This section has as a primary objective to try to answer a number of questions that inevitably can be raised because of the difficulty to take all parameters into account. Indeed, the engineering modeling that was developed in this document is not aiming to account for all the physical mechanisms involved during irradiation. As already clearly stated in the introduction, the main objective is to provide trend curves to engineers that are responsible of designing nuclear components. These trend curves, rather than to establish them empirically, some physical background was put in the model to describe the hardening/embrittlement kinetics. The model was deliberately (actually, there was no other choice) simplified to reduce the number of model parameters that have to be determined. The adequacy of modeling is measured by the performances that it allows in representing the experimental data. It is clear that, at this stage, we cannot pretend that all the data will be well described by the model. However, the model might (should) be improved each time additional evidence is available. For example, the precipitate component should be added as this damage mechanism was experimentally evidenced. However, to correctly describe this phenomenon, it is clear that specific experimental data should be produced. But given the experimental database that is available to date, adding damage mechanisms and therefore damage components would certainly not improve the model performance as we would rely on additional speculation which we tried to reduce as much as reasonably possible.

In the following, we will examine to which extent a number of assumptions that were made are relevant or not. In particular, the effects of material (chemical composition, heat treatments) and irradiation conditions (temperature, neutron versus proton) will be examined.

7.1. Effect of chemical composition and heat treatment

Throughout all this report, no distinction was made between the various 9%Cr – steels although their chemical compositions vary quite substantially. It is interesting to examine to what extend such an assumption is valid. Therefore, we've gathered in Figure 55 the experimental results obtained on various 9%Cr – steels neutron–irradiated at about 55°C. As it can be seen, within the experimental uncertainties, the small differences can hardly be attributed to the material heat. Other examples are given on Figure 56 and Figure 57 for neutron–irradiation data at 300 and 400°C, respectively. So, the assumption on the lack of influence of material heat (chemical composition) is acceptable. This assumption is also supported by other data such as [112, 172-173]. Note that in Figure 57, the data lying significantly above the trend curve are different from the others. Indeed, the former, taken from Klueh and co–authors [87, 156, 161, 180, 199, 205, 324] exhibit a significantly higher initial yield strength (in the range of 700 MPa at 400°C) than the latter (in the range of 500 MPa at 25–386°C). It is believed or suspected that these materials are senstive to temperature, or in other words, these steels are probably not thermally stable. Nevertheless, other mechanisms enter into play, that are out of the scope of the present report.

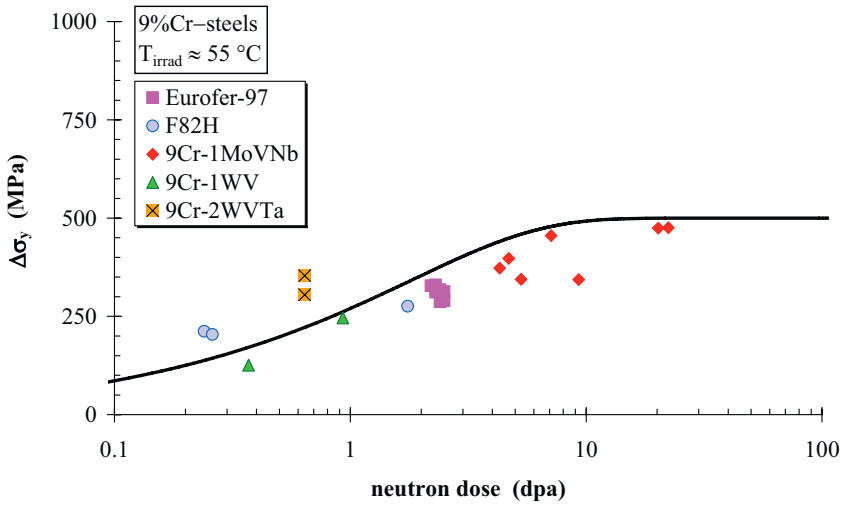

Figure 55. Effect of material heat on irradiation hardening ($T_{irrad} \approx 55°C$).

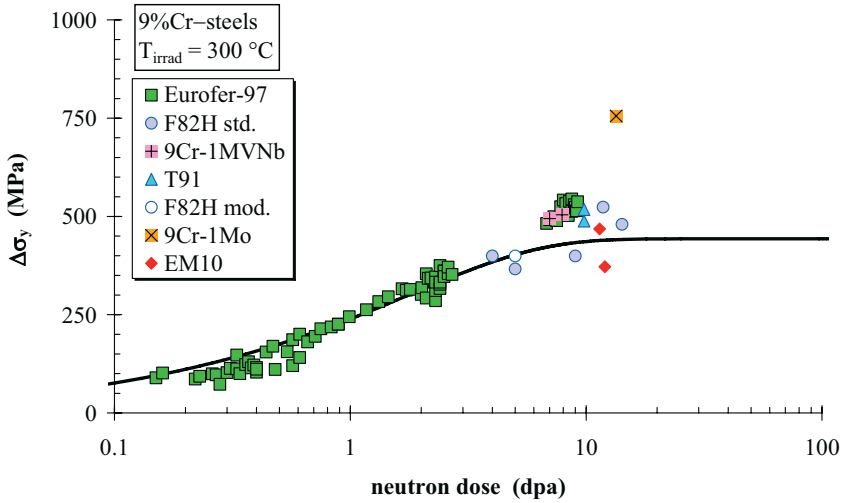

Figure 56. Effect of material heat on irradiation hardening ($T_{irrad} = 300°C$).

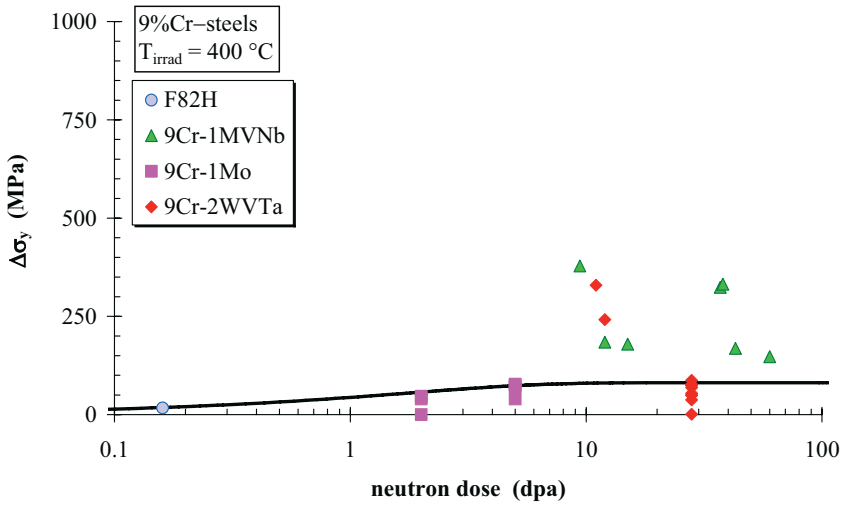

Figure 57. Effect of material heat on irradiation hardening ($T_{irrad} \approx 400°C$).

We developed in the previous section the reasons why the Ni–doping data promoting He–generation were excluded from the experimental database. What about B–doping? It is known that addition of Boron allows during irradiation the formation of He through the ^{10}B (n,α) ^{7}Li reaction. However, this Li–element affects also the microstructure of the steel [108, 230, 234, 236, 270]. Moreover, the quick transformation of Boron into Helium leads to a He–production rate that is much higher than under a typical fusion environment [270]. However, the B–concentrations that were considered in literature are so small that the generated He–content does not exceed few hundreds appm He. In Figure 58, we gathered a number of experimental data obtained by Wakai and co-authors [142-143, 148] which does not unambiguously indicate an effect of He. In [108, 152, 154, 171, 278] the differences on the measured hardening and embrittlement of various 9%Cr–steels were attributed to helium (resp. B–content). However, the helium content is so small that it is doubtful that the observed differences are due to He. As also suggested by Klueh et al. [230], the interpretation of such results could present a source of confusion.

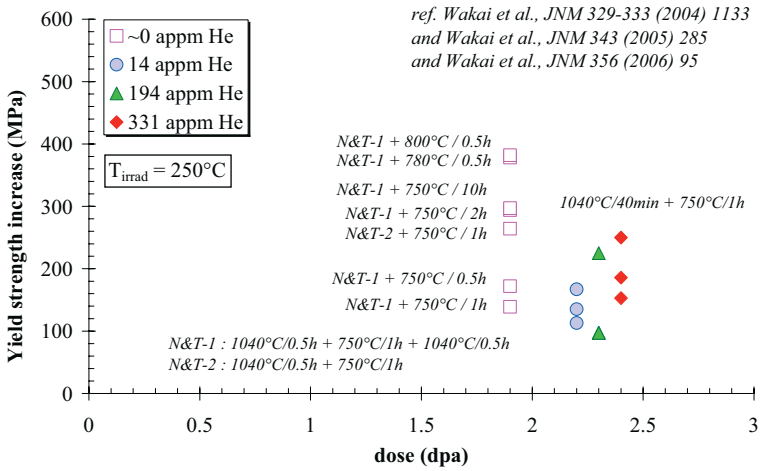

Figure 58. Effect of heat treatment on F82H. Significant effect of heat treatment but not of He–content obtained with B–doped steel.

We included in Figure 58 also the effect of heat treatment that shows the large influence of the heat treatment on the post–irradiation hardening. Unfortunately, such data are not systematically available and microstructural examinations are lacking to allow a more systematic assessment.

7.2. Temperature effects

First, it is interesting to examine the effect of irradiation temperature on the material behavior. We have already indicated that some major conflicts are apparent from the available data, in particular in the transition range before the recovery mechanism starts to effectively operate. We will first examine the general trend of the effect of irradiation temperature and then more details will be given on the effect of irradiation temperature on the post–irradiation behavior of the 9%Cr–steels, including annealing effects.

Examination of the data shows that above ~430 °C, some softening is observed after irradiation. As it was suggested by [83] and [154], this might be due to irradiation–enhanced thermal ageing effects that probably induce precipitate coarsening. According to Bae et al. [99], softening is caused by the reduction of the dislocation density induced by radiation–enhanced dislocation climb and mutual annihilation. Also Möslang and Preininger [100] attribute softening to the radiation–enhanced dislocation recovery and subgrain formation within the martensitic laths. Tamura et al. [325] reported $M_{23}C_6$–precipitate growth and precipitation of Laves phase after thermal ageing. However, the effects of thermal ageing become significant only above ~600°C (for 1000 h exposition). Interesting results were reported by Kimura et al. [31] which indicate the difficulty of interpreting post–irradiation data when the material is sensitive to temperature (thermal ageing). Aging phenomena can harden the material without neutrons. Maziasz and Klueh [222] reported long term thermal aging data on 9%Cr–steels in the temperature range of

482 to 704°C during 25000 h. They clearly established that the evolution of the microstructure is significantly different from the 600°C–irradiated one. Moreover, the microstructure remains stable below ~600°C but coarsened above. Schäfer [214] reported significant degradation of the mechanical properties of F82H-mod steel resulting from precipitation of Laves phase $(Cr, Fe)_2W$ upon thermal aging at 600 and 650°C.

In our model, we considered that above 450–500°C, the irradiation hardening due to displacement damage reduces to zero. Of course, this is not correct but it is expected that even if taken into account, its contribution will be small if the temperature remains below ~600°C, which is the case of our database. For higher temperatures, thermal ageing effects might become significant, as suggested by the thermal aging data.

Below ~430°C, only partial recovery is usually observed. The amount of recovery as a function of temperature is, at this stage, quit ambiguous; the available experimental data do not show a unique picture. We considered three types of data:

Data where irradiation temperature is systematically varied

First, the experimental data obtained by [129, 172-173, 217, 283, 326-327] on various 9%Cr–steels irradiated in a range of 0.2 to ~16 dpa in a temperature range of 250 – 450°C show that irradiation embrittlement remains quasi–constant between 250 and 300°C and onset of annealing recovery occurs above 300°C. Their results are shown in Figures 59 and 60 for embrittlement and hardening, respectively. These results are confirmed on other materials with a more significant recovery rate between 300 and 350°C (see Figure 61) [326-327]. On the other hand, according to Spätig et al. [328], irradiation hardening of F82H irradiated to 0.16 to ~0.5 dpa in a temperature range of 25 – 400°C shows a monotonic decrease from ambient to 400°C. These data are supported by Rensman [279] data on irradiated Eurofer–97 at two temperatures, 60 and 300°C to approximately the same neutron dose level of ~2.4 dpa and the measured irradiation hardening level for the two temperatures were 308 and 335 MPa, respectively. So, it is believed that below 300°C, irradiation hardening dependence on temperature is negligible. Kimura et al. [329] gathered a number of data in the range of 350 – 550°C and high dpa (up to 36 dpa) showing the decrease of embrittlement in this range. Effective annealing recovery of irradiation hardening was shown to occur between 300 – 400°C by Kimura et al. [289]. However, radiation embrittlement measured either with Charpy impact or fracture toughness tests in the range 250 – 500°C shows a monotonic decrease with increasing temperature [276, 289]. But this conclusion is moderated by additional data taken from [47, 330] (see Figure 62). Softening is observed when temperature exceeds about 430°C. Daum and Lindau [164, 309] reported data on two steels, F82H mod and MANET–I, which were He–implanted to 500 appm He and a displacement damage level of 0.3 dpa in a range of temperatures of 50 – 550°C indicating a monotonic irradiation hardening decrease with increasing temperature. However, two important points should be mentioned. First, the various specimens were tested at a temperature equal to the irradiation temperature ($T_{test} = T_{irrad}$). Because the irradiation hardening decreases with increasing test temperature, the slope of the decrease is actually smaller. Second, there is a significant difference of hardening rate between F82H mod and MANET–I, this difference is most probably caused by the high Ni–content of MANET–I.

We collected a number of DBTT shifts published by Klueh and his co–authors on various 9%Cr–steels but as it can be seen from Figure 63, the scatter is such that it is difficult to reliably assess the irradiation temperature effect.
Finally, it appears that for most of the data analyzed in this report, a full recovery is observed around ~450°C.

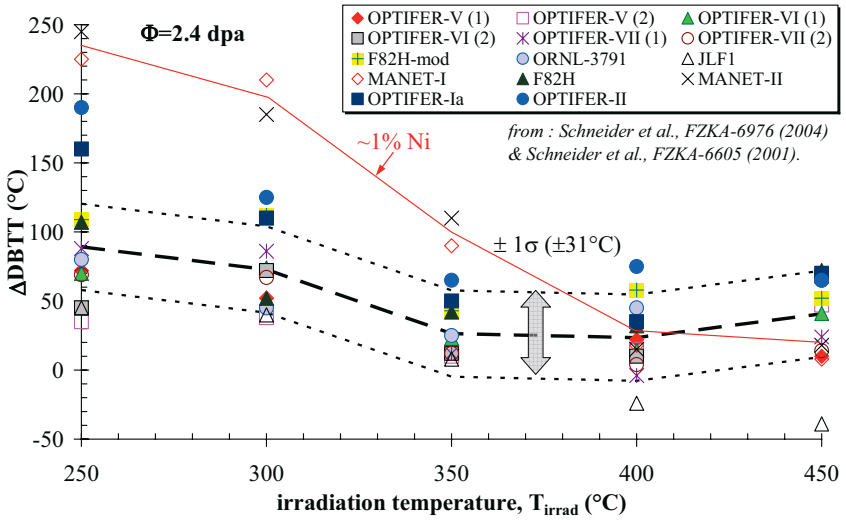

Figure 59. Effect of irradiation temperature on irradiation embrittlement [172-173].

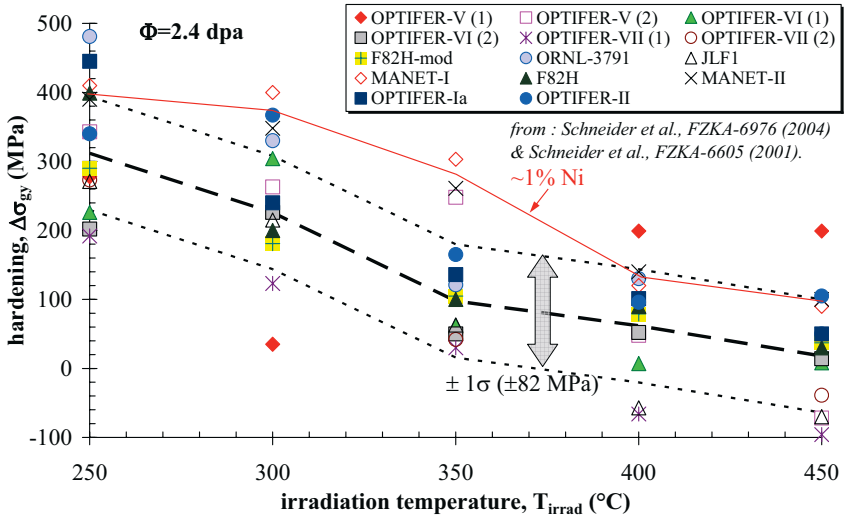

Figure 60. Effect of irradiation temperature on irradiation hardening [172-173].

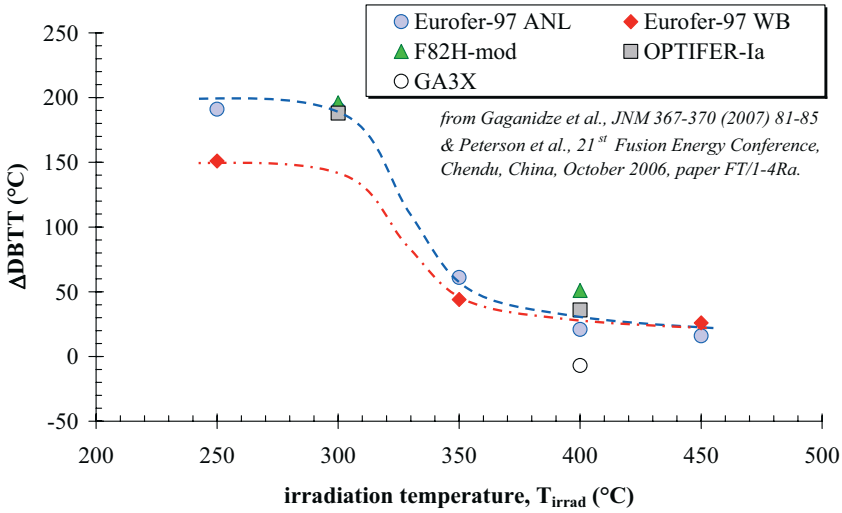

Figure 61. Effect of irradiation on the DBTT–shift of 9%Cr–steels.

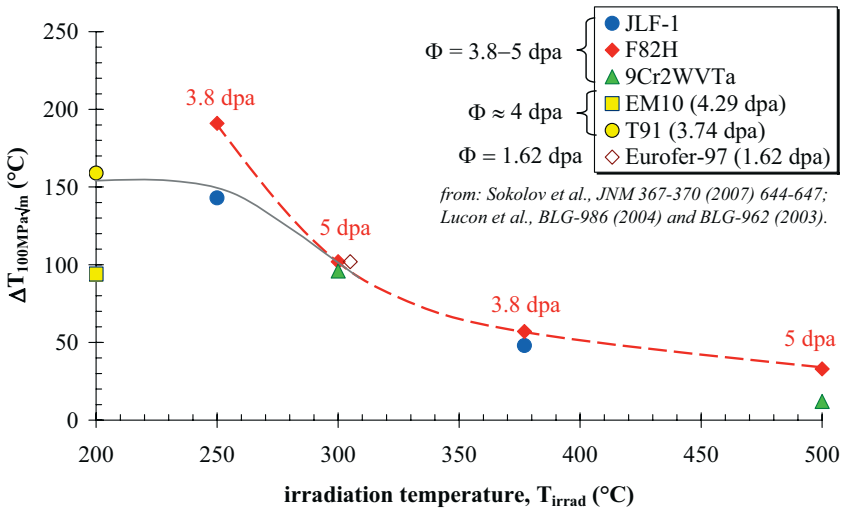

Figure 62. Effect of irradiation on the fracture toughness transition temperature–shift of 9%Cr–steels.

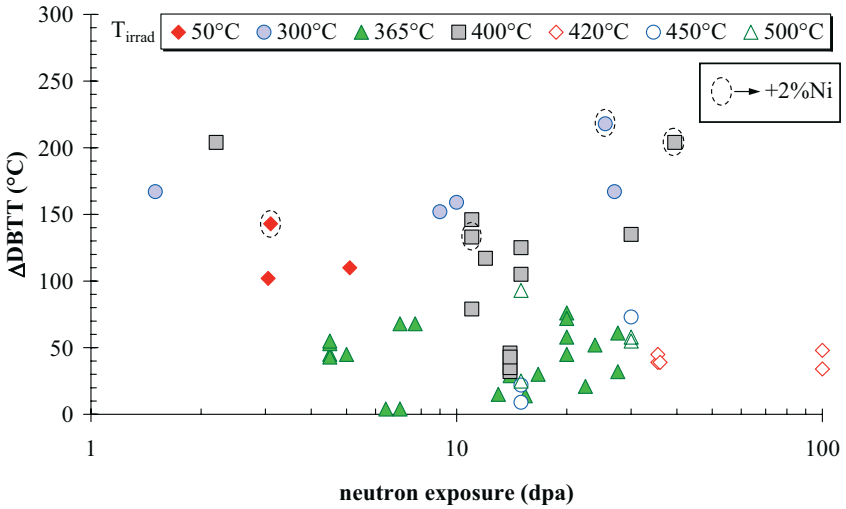

Figure 63. The DBTT–shift as a radiation embrittlement monitor does not allow to consistently differenciate between the various data sets. All data from Klueh et al. [32, 35, 87-88, 91, 159-160, 162, 319] and Lechtenberg [331].

Data irradiated at T_{irrad} and tested at higher temperatures

Rensman and al. [139, 279] irradiated tensile specimens of Eurofer–97 at 60°C to ~2.3 dpa and tested them at increasingly higher temperatures. Unfortunately, the holding time before testing was not reported. The yield strength increase decreases continuously with increasing testing temperature, in agreement with other data published by Horsten et al. [332] on a mod. 9%Cr–steel (see Figure 64). Similar results were obtained by Dai et al. [144] on F82H irradiated with 800 MeV protons at 60°C and tensile tested at higher temperatures after 15–20 min temperature stabilization (see Figure 65). Helium content was ranging between 125 and ~1400 appm He. The results shown on Figure 65 indicate that the yield strength is only partially recovered. Moreover, the recovery amplitude does not seem to depend on the dose level. Finally, the recovery of the proton irradiated samples is clearly lower than the recovery of the neutron irradiated samples. The role of He is unfortunately not clear. Indeed, Maloy et al. [158] reported data on a mod 9%Cr-1Mo steel irradiated to 3 dpa in a spallation environment at 35–50°C that show a full recovery at 400°C. Unfortunately, the amount of generated He was not reported. Finally, it is interesting to examine the data reported by Abe et al. [178, 281] on three 9%Cr–steels, namely 9Cr-1WVTa, 9Cr-3WVTa and 9Cr-1MoVNb, irradiated at about 265°C up to 0.03 and 0.45 dpa in the JMTR reactor. Tensile tests were performed on these steels at room temperature, 200, 300, 400, 500 and 600°C. Very surprisingly, a maximum hardening was observed for the 9%Cr–WVTa steels when tested at ~300°C but not for 9Cr-1MoVNb [178, 281] (see Figure 66). As it can be seen, the 9Cr–WVTa steels exhibit a significant increase of the yield strength at about 300°C followed by a monotonic decrease with increasing temperature. This behavior was associated with carbon, more specifically carbon–vacancy complexes. However, this is not systematically observed on other materials and irradiation, annealing or testing conditions. For example,

the data reported by Schneider et al. [172-173, 233] do not exhibit any hardening or embrittlement peak around 300°C (see Figures 59-60). Other data are not supporting such peak hardening occurrence around 300°C [129, 198, 276, 279, 326, 328-329]. However, as it will be seen next, despite these differences, post–irradiation tests performed by Abe et al. [178, 281] confirmed their observations.

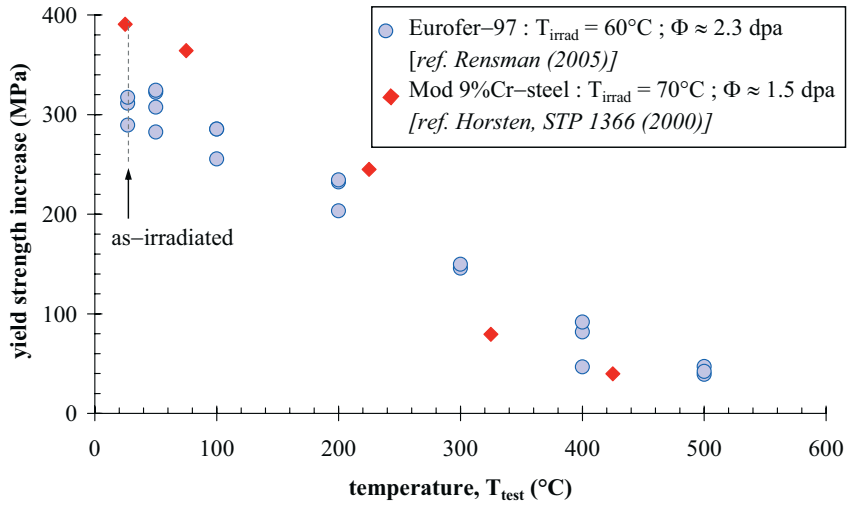

Figure 64. Effect of testing temperature on irradiation hardening of Eurofer – 97 irradiated to ~2.3 dpa at 60°C and Mod 9%Cr – steel irradiated to 1.5 dpa at 70°C [139, 279, 332].

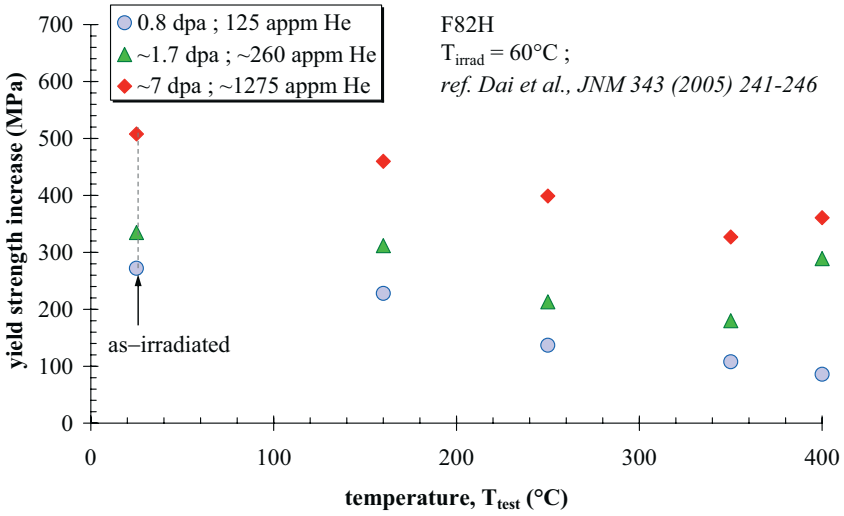

Figure 65. Effect of testing temperature on irradiation hardening of F82H irradiated at 60°C to 0.8, ~1.7 and ~7 dpa [144].

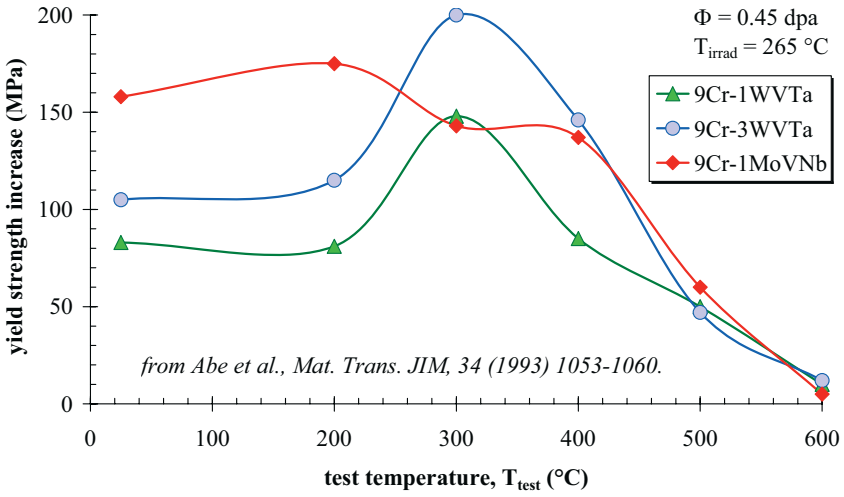

Figure 66. Effect of test temperature on irradiation hardening [178].

Data where post–irradiation annealing is performed

The peak hardening at about ~300°C suggested by the data of Abe et al. [178, 281] were confirmed with post – irradiation annealing experiments. The experimental data shown in Figure 67 exhibit trend curves that are in qualitative agreement with the data shown in Figure 66. Despite this confirmation, this observation cannot be generalized and therefore

some additional hardening mechanisms are suspected but cannot be identified with the available information.

Kimura et al. [333] compared isochronal (1h) post–implantation annealing with neutron irradiated/annealing and reported that the recovery was retarded when helium is present. They suggested that this is due to the suppression of the annealing out of the defect clusters by the presence of helium or by the He–bubble growth that occurs at high temperature. However, it should be mentioned that the two situations were not exactly similar, 156°C/0.048 dpa/120 appm He for the He–implanted samples and 220°C/0.15 dpa for the neutron irradiated samples. Unfortunately, this comparison suffers from the differences in the irradiation conditions in terms of dpa and irradiation temperature although the effect of the latter is assumed to have a negligible effect (156 versus 220°C). Hardness data on 9Cr–steels helium–implanted at <150°C up to 580 appm He and 0.223 dpa and annealed for 1 h in a temperature range of 200–600°C were also reported by Kimura et al. [333-334]. They show a slight hardness decrease below 400°C followed by an increasingly significant recovery above. However, according to these authors, retardation of the thermal recovery is observed on the helium–implanted steel in comparison to the irradiated (helium free) steel which fully recovers at or above 400°C. The residual small hardening observed on helium–implanted specimens after annealing at high temperature (>400°C) is supposed to be due to the thermally stable helium bubbles. Zvezdin et al. [335] reported Charpy impact data on a 9Cr-2MoVNb and 10Cr-1MoVNb irradiated to ~25 dpa at ~350°C in the BOR60 reactor that indicate a significant recovery after annealing at 550°C/4h. This significant recovery was also reported by Petersen et al. [327] on Charpy impact data on Eurofer-97 which indicate that a significant recovery of the transition curve is obtained after irradiation at 330°C to 15 dpa (BOR60) and annealing at 550°C/3h. Moreover, the tensile properties show a nearly full recovery of the yield strength and uniform elongation upon the same annealing. Note that at a lower annealing temperature, namely 450°C, the efficiency of the recovery was much smaller. Kimura et al. [31] showed that upon neutron irradiation in FFTF/MOTA up to 10 dpa at 373°C of two 9Cr–2W steels (JLM-0 and JLM-1), annealing at 500°C/2h resulted in partial recovery of the tensile properties and full recovery (or even over–recovery or softening) at 600°C/2h. These results are partially confirmed on another steel, mod JLF-1, irradiated also in FFTF/MOTA up to 10 dpa at 370°C and annealed at 400, 500 and 600°C/1h [289]. The recovery is complete at and above 500°C. Finally, Marmy [179] obtained a good recovery by annealing the MANET steel at 450°C/6.5h after irradiation to 0.4 dpa at 190°C.

To summarize the effect of temperature on radiation hardening and embrittlement based on the examination of the literature data mentioned above, three main conclusions can be brought out:

1. A full recovery is expected to occur in the range of 450 – 600°C, depending mainly on the irradiation conditions;
2. the major change of the recovery rate occurs in the range between 300 and 450°C;
3. below ~300°C, it is not yet clear how the temperature affects radiation hardening and embrittlement. The lack of experimental data in this range of temperature is also obvious.

Before closing this discussion of the temperature effect, it is important to mention some additional complications on the temperature effect. For example, Chen et al., [336] reported post–irradiation annealing experiments on various structural materials including a Ni-alloy (Inconel 718), a refractory metal (Ta), an austenitic stainless steel (AISI 304L) and a 9%Cr-ferritic/martensitic steel (DIN 1.4926) taken from a spallation target irradiated at 400, 200, 250 and 250°C, respectively and found no significant change of the yield strength but a significant recovery of the ductility. The irradiation temperature was between 200 and 400°C and the annealing temperature was varied between 300°C and 700°C for 1h to 10h. The dpa dose and He–content amount to 20 dpa/3300 appm He, 8.4 dpa/440 appm He, 6.7 dpa/1300 appm He and 5.8 dpa/1300 appm He, respectively. Annealing at 500 and 700°C for 1h of Inconel 718 does not modify the hardening neither the ductility. At 700°C, a significant increase of hardening is observed but not explained. Intergranular fracture is suspected in all specimens. The annealed Ta-sample (400°C/1h) exhibited a significant increase of the yield strength and reduction of the ductility in comparison to the as-irradiated sample. The 304L stainless steel annealed at 700°C/1h shows that the yield strength remains unaffected while the tensile strength (work hardening) and ductility increase. For the DIN 1.4926 steel, upon annealing at 300, 350, 400 and 700°C for 1h, the yield strength is only slightly decreased but the ductility significantly increases with the annealing temperature. Tentative explanation was provided by the authors but remains exploratory and incomplete. These results contradict with those reported by Marmy and Victoria [179] indicating a good recovery of both strength and ductility of the DIN 1.4914 (MANET) irradiated at 190°C and annealed at 450°C/6.5h. On the other hand, the ductility recovery with only very limited hardening recovery was confirmed by Jung et al. [165] who performed post–implantation annealing at 550 and 750°C for 10 h on helium pre–implanted tensile specimens of Eurofer–97 at 250°C up to 2500 appm He and 0.38 dpa. Their microstructural examination revealed that the post–irradiation defects, black dots and small loops, were not observed after annealing but instead, a high density of dislocations is found [165]. Unfortunately, the samples were punched from the deformed tensile specimens and therefore these dislocations might also be attributed to plastic deformation. Again, this phenomenon of post–annealing ductility recovery but strength retention is not understood and requires more investigations.

All the experimental investigations presented here above on the temperature effects show the difficulty to rationalize all these data (see Table 4). There is clearly an urgent need to resolve these experimental conflicts and provide a consistent picture on how actually the temperature affects hardening and embrittlement.

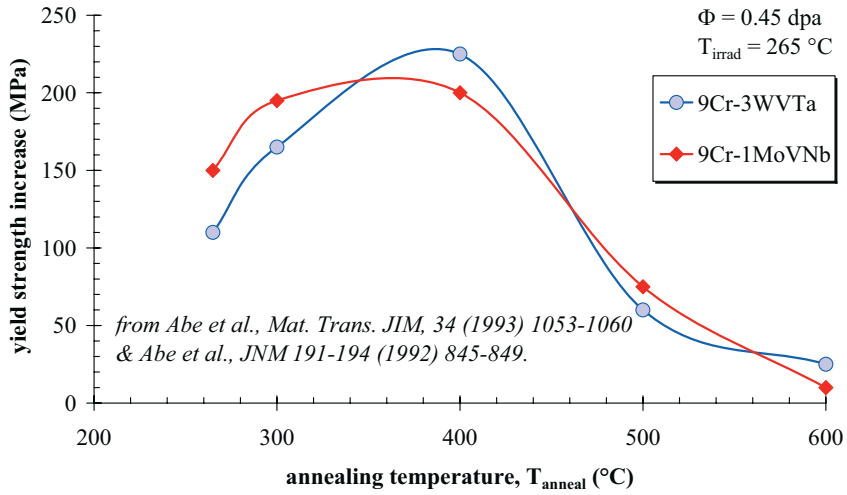

Figure 67. Effect of annealing temperature on irradiation hardening [178, 281].

Table 4. Summary of the results found in literature on temperature effects.

reference	material	T_{irrad} (°C)	dose (dpa)	He–content (appm)	post–irrad	$T_{anneal/test}$ (°C)	t_{anneal} (h)	main outcome
Gaganidze [129, 326]; Petersen [327]	Eurofer–97	250; 300; 350; 400; 450	15	--	Charpy impact tests (DBTT)	--	--	Constant ΔDBTT between 250 and 300°C followed by a significant decrease of embrittlement around 400°C
Kimura [289]	F82H	250 – 500	4 – 5	--	DBTT (Charpy impact and fracture toughness)	--	--	Monotonous decrease of irradiation embrittlement with increasing irradiation temperature. Only partial recovery up to 550°C.
Petersen [327]	Eurofer–97	330	15	--	annealing; DBTT	550	3	Good recovery of the transition curve with a small residual embrittlement.
Jung [165]	Eurofer–97	250	0.38	2500	annealing ; tensile tests at RT & 250°C	550 ; 750	10	Only partial (20 – 50%) recovery of the yield strength. On the other hand, superior ductility's were found after implantation and annealing.
Chen [336]	DIN–1.4926	250	5.8	1300	annealing; tensile tests at 25 & 250°C	300 – 700	1 – 10	Strength retention but remarkable ductility recovery.
Dai [144]	F82H	60	0.8; ~1.7; ~7	125; ~250; ~1250	tensile tests at higher temp.	160; 250; 350; 400	--	Below 350°C, only partial recovery of strength and ductility. At 400°C, partial recovery of the strength and better recovery of ductility. Residual hardening increases with dose.
FZKA-5848 [309] Lindau [164]	F82H mod	50 – 550	0.30	500	tensile tests at irrad temp	T_{test}=T_{irrad}	--	Monotonous decrease of irradiation hardening with increasing irradiation temperature.
	MANET–I							
Rieth [283]; FZKA-6976 [172]; FZKA-6605 [173]	OPTIFER–Ia	250; 300; 350; 400; 450	0.2; 0.8 & 2.4	--	Charpy impact tests (DBTT)	--	--	Monotonous decrease of irradiation hardening with increasing irradiation temperature. Between 250 and 300°C, the difference is not so evident. At 450°C, an small Increase of embrittlement is noticed.
	OPTIFER–II							
	OPTIFER–IV							
	OPTIFER–V							
	OPTIFER–VI							
	OPTIFER–VII							
	MANET–I							
	MANET–II							
	F82H							
	ORNL							
	JLF–1							
Spätig [328]	F82H	25; 250; 350; 400	0.15 – 2	--	tensile tests at RT	--	--	Monotonous decrease of irradiation hardening with increasing irradiation temperature.
Kimura [31]	JLM–0	373; 390; 430; 520; 600	15 – 44	--	tensile tests at RT	--	--	Annealing recovery below ~430°C and softening above.
	JLM–1							
Kimura [31]	JLM–0	373; 390; 430; 520; 600	15 – 44	--	tensile tests at irrad temp	T_{test}=T_{irrad}	--	Annealing recovery below ~430°C and softening above.
	JLM–1							
Kimura [31]	JLM–0	373	10	--	annealing; tensile tests at RT	500 – 600	2	Annealing recovery below ~430°C and softening above.
	JLM–1							
Abe [178, 281]	9Cr-1WVTa	265	0.03 & 0.45	--	annealing; hardness tests	300 – 600	1	9Cr-1WVTa and 9Cr-3WVTa exhibited a hardening peak around 400°C and fast recovery above ~430°C.
	9Cr-3WVTa							
Abe [178, 281]	9Cr-1WVTa	265	0.03 & 0.45	--	tensile testing at higher T	265 – 600	--	9Cr-1WVTa and 9Cr-3WVTa exhibited a hardening peak around 300°C but not for 9Cr-1MoVNb. Full recovery around 600°C.
	9Cr-3WVTa							
	9Cr-1MoVNb							
Kimura [289]	Mod JLF-1	370	10	--	annealing; tensile tests	400, 500, 600	1	Small recovery at 400°C and full recovery at 500 and 600°C.
Kimura [334]; Kasada [231]	9Cr-2W	150 - 220	0.05 – 0.22	~0-580	annealing; hardness tests	150 – 600	1	Recovery kinetics different between neutron irradiated and implanted steels. At 400°C, full recovery for the neutron irradiated steel while onset of annealing for the implanted steel.
Zvezdin [335]	9Cr-2MoVNb	350	25	--	annealing; DBTT	550	4	Significant recovery.
	10Cr-1MoVNb							
Rensman [139, 279]	Eurofer-97	60	2.5	--	tensile tests at higher temp.	160; 250; 350; 400	--	Increasingly significant recovery with test temperature up to about 500°C (full recovery).
Maloy [337]	Mod 9Cr-1Mo	35-50	3	n.a.	tensile tests at higher temp.	160; 250; 350; 400	--	Increasingly significant recovery with test temperature up to 400°C (full recovery).

7.3. Effect of bombarding particles (neutron, proton, ion)

To the authors' knowledge, there were no systematic studies devoted to investigate the effect of the nature of bombarding particles, namely neutron versus protons versus ions. Schäublin and Victoria [248] compared the microstructure of F82H after neutron and proton irradiation and their main conclusions suggest that upon neutron irradiation, the carbides remain crystalline while they are amorphized after proton irradiation (1.7 dpa). Farrell and Byun [112] compared irradiation hardening of few 9Cr–steels irradiated with neutrons in HFIR (high flux isotope reactor) at 60–100 °C to irradiation with 800 MeV proton and spallation neutron irradiation in the LANSCE facility at 60–164 °C. No significant difference was observed between the two irradiations. According to Henry et al. [113], the uniform elongation is significantly reduced under proton irradiation in comparison to neutron irradiation. But Farrell and Byun [170] found no significant difference between proton irradiation (LANSCE) and neutron irradiation (HFIR reactor).

The overall examination of the database reported herein does not suggest a major effect of the bombarding particle–type. Of course, the He–generation rate can be very different but from the displacement damage point of view similar effects seem to occur, independent of the bombarding particle.

7.3.1. Effect of helium content below 1000 appm He

It was already shown that for high He–concentrations, the helium effect on hardening (and embrittlement) is obvious. However, below about 1000 appm He, the effect of He is still debatable. We selected hereafter data which support the low effect of He in the low concentration range (see Figures 68 to 70).

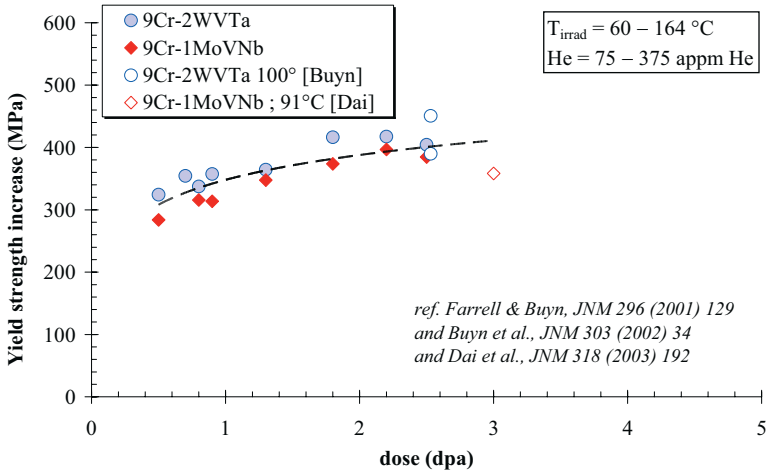

Figure 68. Low temperature (60–164°C) irradiation effect on various 9%Cr–steels. No obvious effect of steel composition and no He–content.

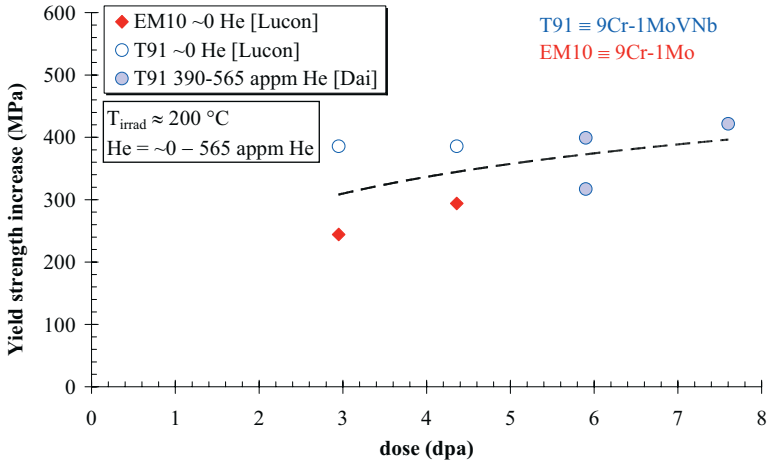

Figure 69. Irradiation effect on various 9%Cr–steels irradiated at ~200°C. No obvious effect of steel composition and no He–content.

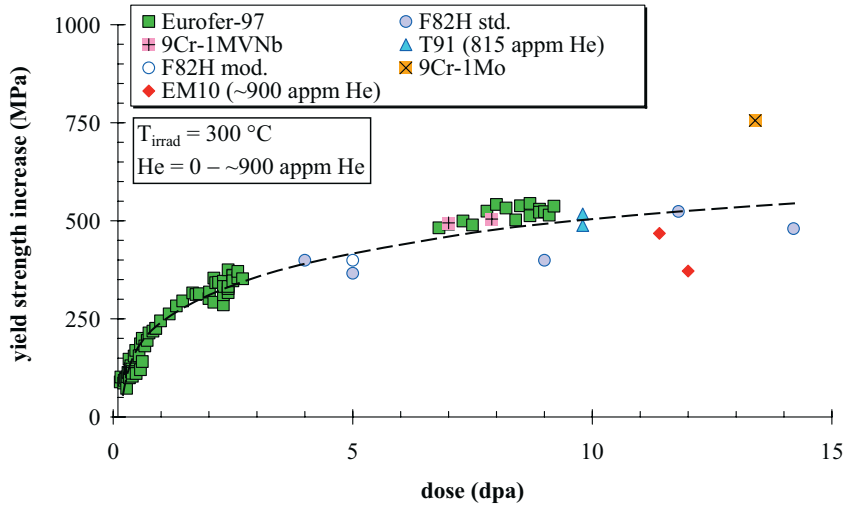

Figure 70. Effect of irradiation (300°C) on various 9%Cr–steels. No obvious effect of steel composition.

As it can be seen from these three figures (Fugures 68 to 70), the presence of He does not seem to affect hardening and therefore, for such low He–contents, the dpa (displacement damage) component is dominating.

7.3.2. On the 500 appm He threshold

In the model, the hardening due to Helium is neglected for He–content below 500 appm He. Dai et al. [193] performed microstructural examination of proton irradiated 9%Cr–steel and did not observed He–bubbles or voids although He–concentration was estimated to be 600 appm.

In literature, hardening and embrittlement is often attributed to helium already at low He–content (<500 appm He). For example, Klueh et al. [159] used Ni–doping to produce helium in a 9Cr-2WVTa steel irradiated at 400°C up to 11 dpa. The observed additional hardening and embrittlement was attributed to helium (115 appm He). However, it is believed that it is the effect of nickel rather than of helium itself. Other data reported in [83, 161] on a 9Cr–1MoVNb show a significant difference between <3 appm He and 7 appm He where the measured yield increase was 93 and 274 MPa, respectively; the specimens were irradiated in HFIR (8-11 dpa) and EBR-II (16 dpa) at 400°C. However, these results are not supported by many other data. The limited available information does not allow understanding this outlier behavior.

It is interesting to rise the question on whether this threshold remain temperature and dose independent. It is clear that more experimental data are needed. At present, it seems that a fixed threshold value of 500 appm does not disagree with most of the results except those indicated above.

7.4. Test temperature effect

Because of the variety of the testing conditions, a procedure allowing for test temperature normalization to ambient (25°C) was developed in section 3. However, this procedure may introduce additional scatter. To evaluate to what extend such a procedure might bias the results, we reproduced in Figure 71 the data of Figure 70 by keeping only tests performed at 300°C. As it can be seen, indeed the scatter is only marginally reduced. This clearly supports the test temperature normalization procedure as presented in section 3.

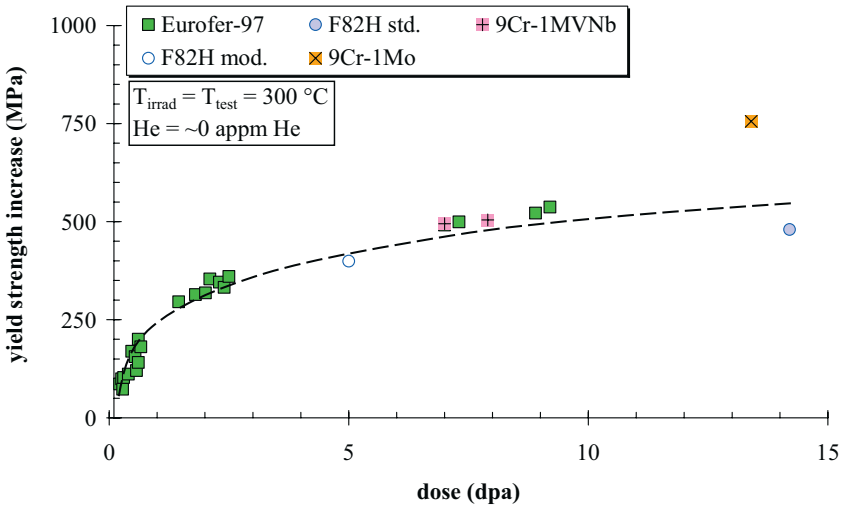

Figure 71. Comparison with Figure 70 indicates that the effect of test temperature correction on the scatter is very small (only slight decrease of the scatter).

7.5. On the appropriate parameter to monitor irradiation effects of 9%Cr–steels

In this report, the parameter that was selected to monitor the radiation effects on the 9%Cr–steels is the yield strength. However, other parameters could be used as well but it was indicated that the yield strength seems to be the best parameter mainly for two reasons, it has a better link to the underlying physical mechanisms and the database is the largest. One important advantage of the tensile test is also the amount of material that is needed. The determination of the DBTT requires much more material and drastic size effects can be expected while tensile data are relatively size/geometry independent except in extreme cases of miniaturized specimens (see later).

In literature, it is sometimes suggested to use, for example, the ductility [338]. Based on a number of experimental data on high Cr–steels, Igata and Kayano [339] suggested also a relationship between ductility and radiation hardening. However, ductility is not an adequate parameter because it has a poor correlation to other properties. Moreover, the total ductility depends on the specimen size and configuration and as a result should be discarded for quantitative assessment.

7.6. Effect of specimen size and configuration

Because of the limited space and the inherent high costs of irradiation, miniaturized specimens are usually used in the fusion community. The size and the shape of these small samples vary in large proportions. In particular, for helium-implanted samples, the

thickness is relatively small, of the order of ~100 µm. The miniaturized tensile geometry is nowadays well accepted in particular to investigate irradiation effects although some size effects were observed when the specimen thickness is below about 0.1–0.2 mm [340]. Hence, despite many investigations dedicated to miniaturized tensile testing, the available data do not allow to provide a satisfactory answer whether size effects are significant or negligible [341-344]. However, for 9%Cr–steels, a typical example is given in Figure 72 for the Eurofer–97. Significant differences can be seen on the same material, the 100 µm thick samples were taken from [167] while other data were taken from [279, 330]. The difference due to specimen size is as high as 100 MPa.

Another important aspect is not treated in literature, namely the statistics or the scatter associated with the material variability and testing procedure. Indeed, most of the reported data are based on a single specimen. There are unfortunately no data to effectively estimate the scatter band around these single values. By contrast, some data taken on an unirradiated A508-type weld show that while the average value is little affected by the specimen size, the scatter significantly increases. This can be seen from Figure 73 which clearly shows the increase of scatter with the reduction of the specimen size. By extrapolating to a cross section of 1 mm², the scatter band can reach ± 50 MPa. This example emphasizes the difficulties of analyzing experimental databanks when based on single specimen values.

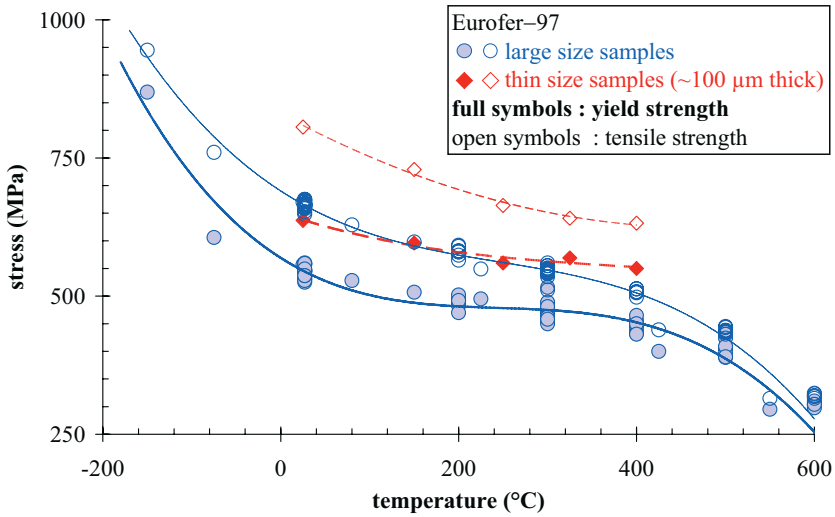

Figure 72. Discrepancies in the tensile properties of Eurofer–97 with large specimen size differences.

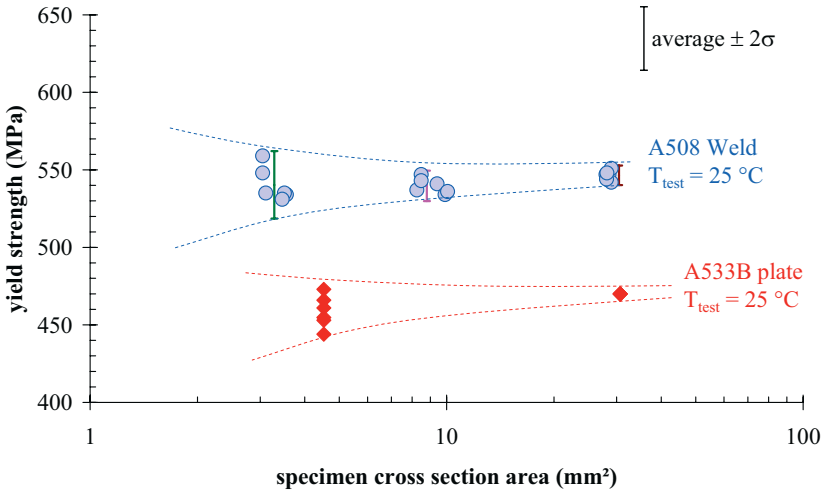

Figure 73. Specimen size effect on the yield strength of an A508 Weld.

A number of geometrical specimen size requirements were given in [345] to provide size independent tensile properties but the statistical aspect is not taken into account. Although not in agreement with Panayotou et al. [346] data, it is believed that the scatter will increase with decreasing specimen size, in particular for miniaturized samples. An example is shown on Figure 73 for a 508 weld. Nevertheless, a minimum size of an acceptable tensile specimen was recommended by Jung et al. [345] should have a gauge length of 5 mm with a rectangular cross section of 1 × 0.4 mm².

As already mentioned, the DBTT parameter plays an important role in structural integrity assessment when it can be correlated to the fracture toughness transition temperature. However, fracture toughness rather than Charpy impact tests are required. Because of the limited space usually available for irradiation, only small size specimens are often accepted. However, small specimens do not provide size and specimen configuration independent properties that can further be used in structural calculations. Indeed, small specimen geometries and some crack configurations exhibit a significant loss of constraint that affects fracture toughness. Therefore, a size correction procedure is usually used. More details can be found in literature on fracture toughness characterization in the transition regime [347-348]. Because of the reduced specimen size, in order to get valid results according to prevailing standards [349], the small specimens are usually tested at much lower temperatures, in other words in the lower shelf regime. As a consequence, the size correction validated in the transition regime is not anymore valid. So it is important to figure out the difficulty to assess such data and therefore they should be substantiated with additional properties such as tensile data.

7.7. Effect of cold working

Alamo et al. [310] reported some tensile data on 10%–cold worked 9%Cr–steels. These materials were not systematically compared in their as–received (normalized+tempered) and cold worked condition except one, the 9Cr–1Mo steel (see Figure 74). At 325°C after 3.4 dpa irradiation, the cold worked material exhibited a higher irradiation hardening in comparison to the as–received steel (326 versus 279 MPa). This was not expected and examination of the data indicates some inconsistency.

The higher radiation hardening for cold worked steels was confirmed by Henry et al. [113] who tested EM10 in both tempered and 20% cold worked condition. Actually, the data are not reliable as the temperature was increased during irradiation but for a comparison purpose, these data can still be used. The results are shown in Figure 75 and systematically, the cold worked samples exhibit a significantly higher hardening. However, de Carlan et al. [338] found no major difference in terms of irradiation hardening (9 dpa / 325°C) between tempered and cold worked ferritic/martensitic steels.

Given the limited data and their conflicting conclusions, the effect of work hardening cannot be reliably assessed. However, it should be stated that even if cold working would reduce the irradiation hardening, it does not mean that it will behave better than the as–received material. Indeed, the absolute values of the strength and not only their change upon irradiation should also be considered. This will be illustrated later, for the oxide dispersion strengthened (ODS) steels.

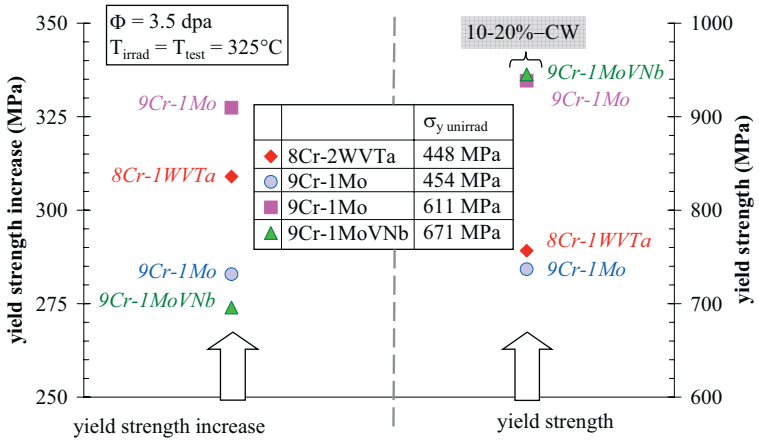

Figure 74. Effect of cold working on irradiation hardening of various 9%Cr–steels. The inbeded table indicates the initial yiel strength of the various steels (~450 MPa in the as–received condition and above 600 MPa for the cold–worked steels).

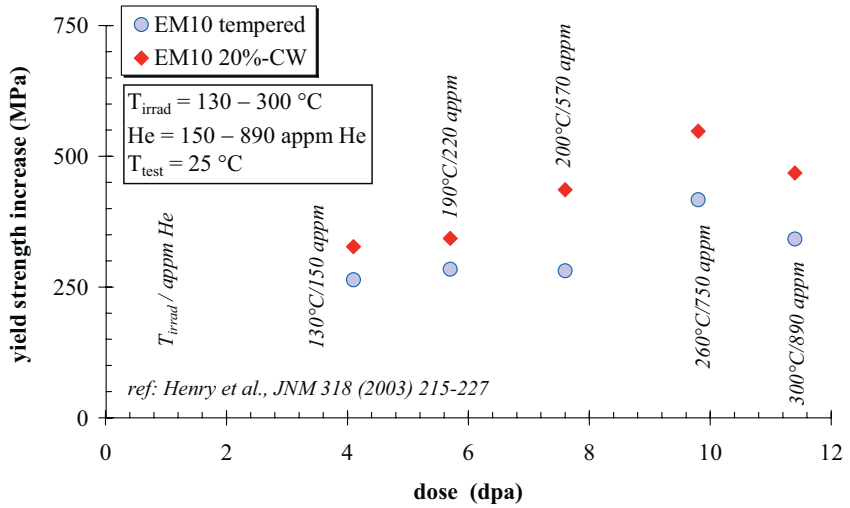

Figure 75. Effect of cold working on irradiation hardening of EM10. Irradiation hardening is systematically higher for the 20%–cold worked EM10 steel.

7.8. On the data inconsistency

We have given a number of inconsistencies that were found in the data used throughout this report. It is important to mention some of these inconsistencies or incoherencies for illustration only. For instance, Baluc et al. [311] reported tensile data on OPTIMAX A steel proton irradiated in PIREX to less than 1 dpa at 25°C and 250°C. The irradiation hardening at 25°C was significantly higher than at 250°C (almost one order of magnitude, see Table 5). Microstructural studies did not reveal major differences except that the carbides were amorphized when irradiated at room temperature but remain crystalline at 250°C. Possible hydrogen effect was not mentioned. Nevertheless, these data are not supported by other available data on similar steels.

Table 5. Data inconsistency between 25 and 250°C [311], OPTIMAX steel.

dose (dpa)	$\mathbf{T_{irrad}}$=$\mathbf{T_{test}}$ (°C)	σ_y (MPa)	σ_u (MPa)	$\Delta\sigma_y$ (MPa)	$\Delta\sigma_u$ (MPa)
0	25	416	610		
0.37	25	542	631	126	21
0.93	25	662	701	246	91
0	250	385	480		
0.3	250	392	529	7	49
0.75	250	412	521	27	41

Henry and co-authors [79, 350] tested KLST Charpy type specimens that were homogeneously He–implanted to a depth of ~240 μm below the V–notch. The He–

implantation, performed at 250°C resulted in about 2500 appm He and 0.4 dpa and an increase of the yield strength measured on tensile specimens at 25°C from ~650 MPa to ~1200 MPa. The KLST specimens tested quasi–statically at 25°C indicated a brittle fracture in the implanted region, the test records indicating a pop–in behavior that was associated by these authors to the brittle fracture. However, examination of the test records indicates that these data are not consistent with the values derived from the tensile data as well as the values of the fracture stress.

Also, Tanigawa et al. [77] reported cleavage fracture stress values of three irradiated 9%Cr–steels, F82H, JLF–1 and ORNL9Cr that are significantly higher than usual values. For instance, in the case of ORNL9Cr, the cleavage fracture stress increased from 2090 MPa to 3380 MPa, which is not reasonable at all. The reason of these incoherent data is that the fracture stress is calculated by multiplying the yield strength measured at the DBTT by a factor 3, the latter accounts of the stress concentration. However, this factor is too high and the DBTT is not well defined and this leads to inaccurate results.

These few examples, together with the other inconsistencies related to the effect of irradiation temperature, illustrate the difficulty of accurate modeling. Of course, these experimental results are intrinsically not wrong; it is our interpretation that is not correct.

7.9. On the advantageous use of oxide dispersion strengthened (ODS) steels

There is a tendency in the scientific community to advocate the use of oxide dispersion hardened (ODS) steels [109, 203, 351-361] as they are associated with a better resistance to irradiation, in particular the creep strength properties. This statement should be a little bit moderated. Indeed, the introduction of nano–features, the oxide dispersion, can be assimilated as irradiation defects (introduced in a controlled manner). Therefore, these oxide dispersion features also impede dislocation motion increasing thereby the yield strength. As a result, fracture toughness is also degraded. So, it is important to keep in mind that ODS–steels are already in the unirradiated condition less crack resistant than the non–ODS type of steels. For illustration, an example is given in Figures 76 and 77 taken from [141]. In Figure 76 the increase of yield strength plotted as a function of neutron exposure shows clearly that the ODS–steel irradiation hardening rate is significantly lower than for standard 9%Cr–steels. However, the ODS–steel can be assimilated to an irradiated material in which the defects (oxide dispersion nano–features) were voluntarily introduced. As a result, the initial (unirradiated) yield strength is significantly higher, something like 450 MPa higher that in non–ODS steels. By plotting the absolute value of the yield strength rather than its change, Figure 77 shows that the ODS–steel exhibits much higher yield strength than the non–ODS steels which will affect the fracture toughness as well. By shifting the ODS–steel trend curve as indicated on Figure 77 the difference in hardening rate between ODS and non–ODS steels shows that no benefit is obtained by the ODS–mechanism.

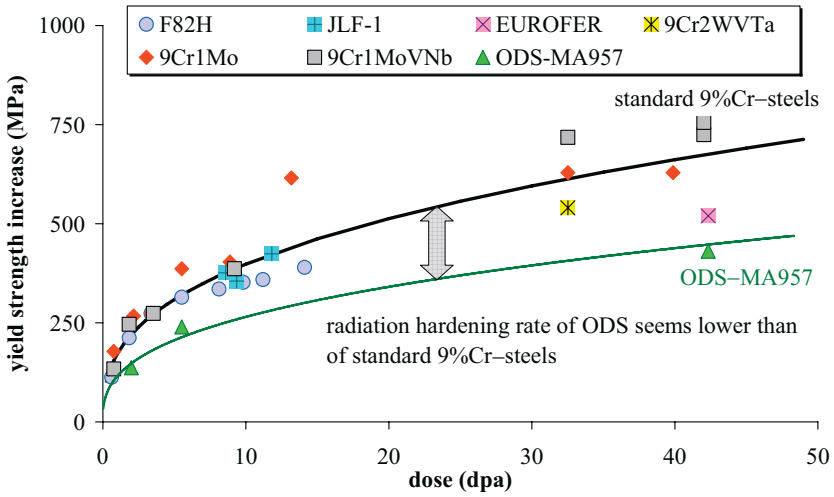

Data from Alamo et al., JNM 367-370 (2007) 54-59.

Figure 76. Irradiation hardening of standard 9%Cr–steels and ODS–MA957–steel. Such a figure is suggesting that ODS hardening rate is significantly lower in comparison to standard 9%Cr–steels.

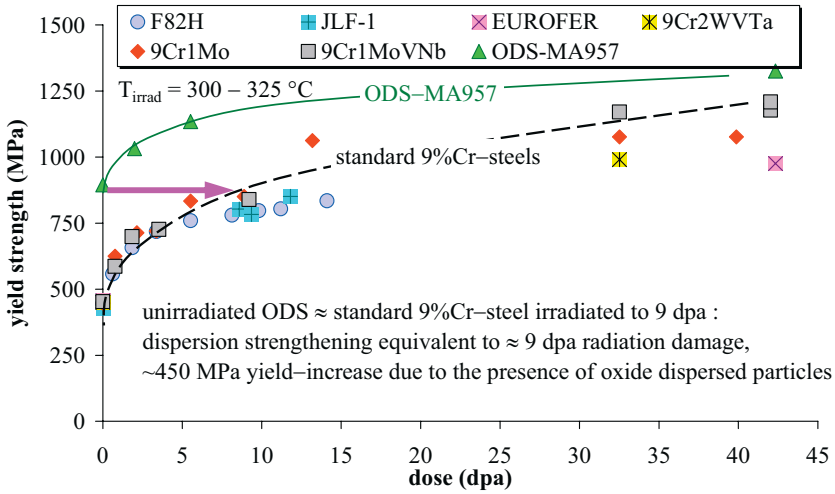

Data from Alamo et al., JNM 367-370 (2007) 54-59.

Figure 77. Yield strength of standard 9%Cr–steels and ODS–MA957–steel as a function of neutron exposure. The lower radiation hardening rate is concealing that the absolute yield strength of ODS–steel is significantly higher.

Unfortunately, most of the experimental data on fracture behavior of ODS–steels are based on the Charpy impact test. There are only very few fracture toughness data, in

particular in the high temperature range. If we examine the available data in literature, we can easily see that the fracture toughness properties of ODS–steels are critically low, before as well as after irradiation. The example shown on Figure 78 clearly shows the drastic change of ductile initiation and tearing resistance of ODS–type steels. The oxide dispersion particles offer an easy path requiring little energy for crack propagation.

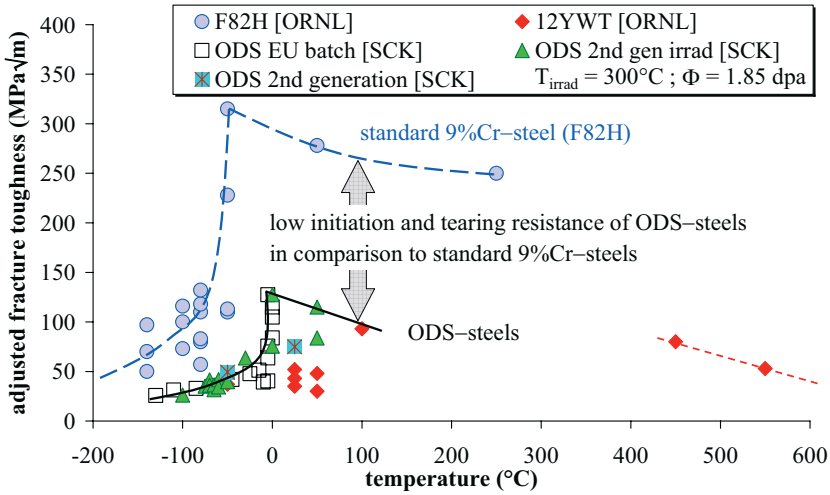

Data from Sokolov JNM 367-370 (2007) 213-216 and Lucon BLG-1024 & BLG-1028 (2006).

Figure 78. Fracture toughness of ODS–MA957–steel is significantly lower than the standard 9%Cr–steels in both the transition and ductile regions.

The main advantage of ODS–type–steels can be defendable at high temperature, above 600°C. The strength of standard 9%Cr–steels decreases to very low values above this temperature while ODS–steels lie some 100 MPa higher. The creep properties are also better in this range of temperature. Finally, from the helium embrittlement point of view, the ODS–steels offer a better resistance to helium as the oxide dispersion fine particles offer traps to helium avoiding therefore coalescence of helium and formation of large bubbles that can be detrimental to the material resistance.

7.10. Overall performance of the model and possible improvements

The model proposed in this report was developed having in mind two main objectives:

1) it should be as simple as possible with a limited number of variables;
2) it should provide a rationale to the available experimental data.

The "as simple as possible" objective does not exclude a more sophisticated model but the number of variables should also be taken into account. Indeed, it is logically possible to consider multiple damage components associated to black dots, dislocation loops, precipitates (including phases such as α'–, G–, χ–, Laves phases) and He–bubbles. Also, for the He–bubble kinetics, rather than assuming a constant He–bubble size and a linear

dependence of the bubble density with exposure, other formalisms could be considered. However, this is not an easy task because each additional component brings new parameters that should be identified and determined. Moreover, the situation is complicated by the appropriate superposition law to consider. And unfortunately, our database does not allow performing such an assessment and this is the reason why we voluntarily kept the model quite simple.

For the second point related to the database, it is important that the model captures the observations that are made on the available data. Having faced a number of experimental incoherencies, it was unfortunately not possible to propose a more sophisticated model taking into account other mechanisms, such as softening and He–saturation, for example, without speculation.

7.11. Closure

We considered in this section a number of questions but it is clear that many other questions can still be raised. Unfortunately, with the available information, additional questions and tentative explanations would be speculative. Definitely, additional more controlled and reliable experimental data are needed before any improvement could be expected.

VIII. SUMMARY AND CONCLUSIONS

Design of nuclear components requires knowing how the environmental conditions such as neutron exposure and temperature would affect the long term behavior of the materials. This is important not only for the operation aspect but also from the safety point of view. An important effort was worldwide devoted to 9%Cr–ferritic/martensitic steels for many nuclear applications including thermonuclear fusion systems, generation–IV fission reactors and accelerator driven systems. Many engineers and researchers are now working on designing such advanced nuclear systems. The material selection is a critical issue to guarantee the safe operation of such machines in normal, abnormal and accidental conditions. For the material selection and the estimation of critical components, , one should rely therefore on trend curves describing the evolution of the material properties with environmental conditions (time, dose, helium,…) . For all these applications, the expected dpa levels but also the neutron induced He–generation levels will be much higher than nowadays components. Experimental data covering such conditions became necessary for safety assessment. Unfortunately, while high dpa levels can be reached in several material research reactors, the generation of helium remains problematic and is still an open debate. Indeed, the available neutron spectra do not allow simulation of the helium generation. In addition, the He/dpa ratio is also often not representative. So, a number of simulation methods were developed to generate helium together with displacement damage. These methods include Ni–and B–doping, proton irradiation and helium implantation. Examination of literature data published during the last three decades allowed to build a database which can be used to develop a model able to rationalize these data. The objective of the HELENA project is to gather all these experimental data in a unique framework where the known or accepted physical mechanisms are taken into account to provide analytical tools to design engineers for estimating the resistance of these steels to irradiation.

The approach is basically simple and relies essentially on the dispersed barrier hardening model. The main damage features that are induced under irradiation were separated into displacement damage (dpa) and He–bubbles. The displacement damage mainly consists of point defect clusters that include the so–called black dots and small dislocation (mainly interstitial–type) loops. These types of defects are very sensitive to the irradiation temperature. The higher the temperature, the lower the number of surviving defects. To establish the irradiation temperature dependence of hardening, we used the radiation annealing kinetics. It is known that several mechanisms coexist during annealing, each of them having its activation energy. However, in absence of well dedicated annealing experiments, it is not possible to assess all these energies. Therefore, a first–order annealing kinetics with an effective activation energy was assumed and fitted on the available data where irradiation temperature was changed. Other data taken from specimens irradiated at a low temperature and tested at increasingly higher temperatures were also used. The law of variation of the temperature dependence was then derived from annealing data. This function follows an Arrhenius–type law and the parameters can be fitted to the available data. The amplitude of radiation hardening is fitted on a single experimental condition. Furthermore, the saturation level above which no additional hardening is observed was also experimentally defined.

For the helium bubbles, the He–component is based on the Trinkaus [J. Nucl. Mater. 318 (2003) 234–240] description of dynamic re–solution of helium bubbles under displacement cascades in the temperature range of interest (50 – 600°C). However, because of lack of data, the He–saturation level could not be reliably determined and therefore a square root dependence with exposition was assumed.

Both linear and quadratic superposition laws were considered to combine the dpa– and He– components but all results were presented assuming a quadratic superposition law. At this stage, it is difficult to prefer one or the other law.

This work has shown the possibility of providing engineering tools to evaluate irradiation effects on hardening and embrittlement including both dpa and helium damage of 9%Cr–ferritic/martensitic steels. It is clear that the performance of such an engineering modeling depends very much on the input data, namely the experimental data on which a number of parameters are based. Of course, all underlying mechanisms are not taken into account, at this stage, in order to limit the number of variables. Instead, only two major components were considered, dpa–damage on one hand and He–damage on the other hand.

One of the main difficulties encountered in this work is the lack of detailed information on the experimental conditions. Indeed, we did not have access to the raw data but only to "manipulated" or "treated" results. The data analysis and interpretation would have been significantly improved if raw data were available, such as the whole tensile test records, the Charpy impact test records including all detailed information on the irradiation and testing conditions.

This difficulty was illustrated by the major conflict observed on the effect of irradiation temperature. Other difficulties are related to the large number of variables considered in the database. Actually there are no or negligibly few experiments with single–isolated variable. Materials are not all similar, from both chemical composition and heat treatment, the irradiation conditions (reactor type, neutron spectrum) are not the same and testing conditions are not similar as well. So, it is not surprising that some inconsistencies can be observed and therefore the model capabilities should be taken with large uncertainties. A number of data are also missing, for instance both high dpa high He–content data are desirable. It is clear that an urgent call for a reliable database with well defined variables becomes obvious to improve modeling performances.

Given the restrictions that are given above, one can refer to G.E.P. Box quotation: "*All models are wrong but some are useful*".

IX. RECOMMENDATIONS

The recommendations given herein are believed to be very helpful in improving the modeling performances of irradiation effects on 9%Cr–steels in presence of both dpa and helium. These are not classified in their order of importance but rather arbitrary.

Monitor material
Given the multiplicity of irradiation programs carried out all over the world, it becomes desirable to incorporate a monitor steel that should be used in each irradiation campaign. Such monitor material is usually used in surveillance programs offers an additional quality assurance to the experimental results. Small amount of material, necessary for few tensile tests on sub–sized specimens, should become a requirement.

Irradiation effects monitoring
There is variety of mechanical properties that are measured on 9%Cr–steels including tensile properties, hardness, DBTT, …. However, from a modeling point of view, the tensile test is the most appropriate parameter that can be used for modeling. Therefore, it is essential to systematically perform tensile tests, preferably at room temperature and to test two to three samples per condition. For specific conditions, other properties can be also evaluated. Moreover, modeling tools can be used to correlate the various properties.

Re–consider the DBTT definition
For historical reasons, the DBTT based on Charpy impact tests was used to monitor irradiation effects of reactor pressure vessel materials and was extended to other materials and components without any further verification and validation. Thus, many investigator use the DBTT measured at 50% of the energy absorbed at upper shelf. This DBTT definition is quiet approximate and it can lead to unconservative results. Therefore, it is important to use the whole information that is available including the instrumented test records. Tensile tests at static loading are also required. In any case one should rely only on this parameter.

Fracture toughness tests
Nowadays, fracture toughness testing has reached a very good degree of confidence and standardization. It is time to move directly towards measured fracture toughness rather than deriving it through approximate correlations with Charpy impact data. It is also essential to perform fracture toughness tests at the operation temperatures.

Use of sub–sized or miniaturized specimens
The space that is usually available for irradiation is often limited and the worldwide tendency is reduce the size of the specimens. Some miniaturized specimen testing has reached a good degree of confidence and acceptance in the scientific community. However, this should be done carefully because, while size effects can be well taken into account for some properties, they may reduce the accuracy of the measured property and needlessly increase the scatter. Moreover, one should clearly look how we can get one good property rather than obtaining three approximate properties.

A typical example is given by fracture toughness tests in the transition regime using sub–sized specimens. Because of their inherent substantial loss of constraint, tests are usually performed at lower temperatures than usually. As a result, the transition temperature, $T_{100MPa\sqrt{m}}$, is determined in the lower rather than transition regime. As a consequence, size correction could become inappropriate. So, it is important to clarify the way the transition behavior could be characterized with specimens tested in the lower shelf regime.

Effect of irradiation temperature

Irradiation temperature plays an important role on the survival of point defects and their evolution, and on the precipitation and helium kinetics. The data examined here show inconsistent data and therefore a more reliable assessment of the effect of temperature should be undertaken considering not only the effect of irradiation temperature on hardening and embrittlement but also on post–annealing behavior.

Effect of radiation–induced plastic flow localization

Under increasingly higher dose levels, radiation–induced plastic flow localization tends to occur reducing significantly the material resistance to fracture. It is important to investigate this topic very carefully and should be taken into account for safety analysis of nuclear components.

Irradiation of He–implanted samples

Examination of the available data including neutron irradiation, proton irradiation and He–implantation show that they do not cover a large range of desirable conditions. For example, for high He–content, the dpa dose is usually lower than 1 dpa. In general, the available data cover mainly two ranges, a range where the He–to–dpa ratio is between ~0 and 200 appm He/dpa (neutron and proton irradiations) and range where the He–to–dpa ratio is around 6000 appm He/dpa (implantation). Therefore, gaps in the database should be filled by performing for example He–implantation followed by irradiation.

Dose rate effects

One of the major difficulties in simulating operation conditions is related to time–dependent phenomena. Thus, long time aging would play a crucial role. At this stage, the time scale that is considered for most of the irradiation studies are those of material test reactors, namely few cycles of operation generally not exceeding one year of operation. In a real component, few decades of time scale are expected. The model, in particular the dpa–component at this stage does not take the dose rate effect into account. Again, experimental data are needed to develop a model where all these effects are accurately taken into account.

He–saturation

In the proposed model, the dpa–component was assumed to saturate with neutron exposure but not the He–component. Saturation of the He–component is also expected as hardening cannot increase indefinitely with He–content. However, the data that were available here do not allow a reliable evaluation of this saturation and additional data are obviously required.

Microstructural examination

One of major missing that is found in literature is the examination of single variable experiments to trace the single parameter effect. Damage accumulation under overall similar condition is also not available. In most cases, multi variable experiments are reported and the microstructural information is therefore very often of limited impact in terms of quantitative analysis. Therefore, it is recommended to perform more systematic microstructural analyses to be able to support modeling.

As it can be see, there is enough room for improving the performances of modeling but this clearly requires not only analytical work but also reliable experimental work.

REFERENCES

[1] K. Ehrlich, Phil. Trans. Roy. Soc. Lond. A 357 (1999) 595–632.

[2] A.A.F. Tavassoli, J. Nucl. Mater. 302 (2002) 73–88.

[3] A.A.F. Tavassoli, J. Nucl. Mater. 258–263 (1998) 85–96.

[4] E.E. Bloom, S. J. Zinkle and F. W. Wiffen, J. Nucl. Mater. 329–333 (2004) 12–19.

[5] K. Ehrlich, E. E. Bloom and T. Kondoal, J. Nucl. Mater. 283–287 (2000) 79–88.

[6] G.R. Odette, Rad. Eff. 101 (1981) 55–71.

[7] A. Fabry, Modeling-based embrittlement trend curve for KWO vessel submerged-arc weld, SCK•CEN report R–3090, December 1995

[8] T.J. Williams and D. Ellis, in: Effects of Radiation on Materials: 20th International Symposium, ASTM STP 1405, S.T. Rosinski, M.L. Grossbeck, T.R. Allen, and A.S. Kumar, Eds., American Society for Testing and Materials, 2001, pp. 8–27.

[9] T.J. Williams, P.R. Burch, C.A. English and P.H.N. de la cour Ray, in: Proceedings of the 3rd International Symposium on Environmental Degradation of Materials in Nuclear Power Systems – Water Reactors, G.J. Theus and J.R. Weeks, Eds., The Metallurgical Society, Inc., 1988, pp. 121–131.

[10] E.D. Eason, J.E. Wright, and G.R. Odette, Improved embrittlement correlations for reactor pressure vessel steels, NUREG/CR-6551, November, 1998.

[11] S.B. Fisher and T.J. Busswell, Int. J. Pres. Ves. & Piping 27 (1987) 91–135.

[12] G.E. Lucas, J. Nucl. Mater. 206 (1993) 287–305.

[13] G.R. Odette, J. Nucl. Mater. 85 & 86 (1979) 533–545.

[14] G.D. Johnson, F.A. Garner, H.R. Brager and R.L. Fish, in: Effects of Radiation on Materials: 10th Conference, ASTM STP 725, D. Kramer, H.R. Brager, and J.S. Perrin, Eds., American Society for Testing and Materials, 1981, pp. 393–412.

[15] F.A. Garner, M.L. Hamilton, N.F. Panayotou, and G.D. Johnson, J. Nucl. Mater. 103 & 104 (1981) 803–808.

[16] K. Ehrlich, J. Nucl. Mater., 133 & 134 (1985) 119–126.

[17] M.L. Grossbeck, P.J. Maziasz, and A.F. Rowcliffe, J. Nucl. Mater. 191–194 (1992) 808–812.

[18] G.R. Odette and D. Frey, J. Nucl. Mater. 85 & 86 (1979) 817–822.

[19] J.L. Séran, A. Alamo, A. Maillard, H. Touron, J.C. Brachet, P. Dubuisson and O. Rabouille, J. Nucl. Mater. 212–215 (1994) 588–593.

[20] N. Hashimoto, R.L. Klueh, M. Ando, H. Tanigawa, T. Sawai and K. Shiba, Fus. Sci. Techno. 44 (2003) 490–494 .

[21] W.L. Hu and D.S. Gelles, in: Influence of Radiation on Material Properties: 13th International Symposium, ASTM STP 956, Part II, F.A. Garner, C.H. Henager, Jr., and N. Igata, Eds., American Society for Testing and Materials, 1987, pp. 83–97.

[22] M. Victoria et al., Fus. Eng. Des. 82 (2007) 2413–2421.

[23] D. Terentyev, P. Olsson, L. Malerba and A.V. Barashev, J. Nucl. Mater. 362 (2007) 167–173.

[24] L. Malerba, D. Terentyev, P. Olsson, R. Chakarova and J. Wallenius, J. Nucl. Mater. 329–333 (2004) 1156–1160.

[25] J. Wallenius, P. Olsson, L. Malerba and D. Terentyev, Nucl. Instr. Meth. Phys. Res. B255 (2007) 68–74.

[26] B.D. Wirth, G. R. Odette, J. Marian, L. Ventelon, J. A. Young-Vandersall and L. A. Zepeda-Ruiz, J. Nucl. Mater. 329-333 (2004) 103–111.

[27] D.J. Bacon and Y.N. Osetsky, Mat. Sci. Eng. A365 (2004) 46–56.

[28] B.D. Wirth, M. J. Caturla, T. Diaz de la Rubia, T. Khraishi and H. Zbib, Nucl. Instr. Meth. Phys. Res. B180 (2001) 23–31.

[29] R. Kemp, G.A. Cottrell, H.K.D.H. Bhadeshia, G.R. Odette, T. Yamamoto and H. Kishimoto, J. Nucl. Mater. 348 (2006) 311–328.

[30] T. Yamamoto, G.R. Odette, H. Kishimoto, J.W. Rensman and P. Miao, J. Nucl. Mater. 356 (2006) 27–49.

[31] A. Kimura, T. Morimura, M. Narui and H. Matsui, J. Nucl. Mater. 233–237 (1996) 319–325.

[32] R.L. Klueh, D. J. Alexander and M. Rieth, J. Nucl. Mater. 273 (1999) 146–154.

[33] G.R. Odette, J. Nucl. Mater. 212–215 (1994) 45–51.

[34] G.E. Lucas, G.R. Odette, K. Edsinger, B. Wirth and J.W. Sheckherd, Effects of Radiation on Materials: 17th International Symposium, ASTM STP 1270, D.S. Gelles, R.K. Nanstad, A.S. Kumar, and E.A. Little, Eds., American Society for Testing and Materials, 1996, pp. 790–814.

[35] R.L. Klueh and D.J. Alexander, J. Nucl. Mater. 218 (1995) 151–160.

[36] R. Chaouadi, J. Nucl. Mater. 360 (2007) 75–91.

[37] R.O. Ritchie, J.F. Knott and J.R. Rice, J. Mech. Phys. Solids, 21 (1973) 395–410.

[38] M.S. Wechsler, R.G. Berggner, N.E. Hinkle and W.J. Stelzman, in: Irradiation Effects in Structural Alloys for Thermal and Fast Reactors, ASTM STP 457, American Society for Testing and Materials, 1969, pp. 242–260.

[39] J.F. Knott, Fundamentals of Fracture Mechanics, Butterworths, 1973.

[40] A.S. Tetelman and A.J. McEvily, Jr., Fracture of Structural Materials, John Wiley & Sons, Inc., 1967.

[41] X.Z. Zhang and J.F. Knott, Acta Mater. 47 (1999) 3483–3495.

[42] R. Maiti, G.E. Lucas, G.R. Odette and J.W. Sheckherd, J. Nucl. Mater. 141–143 (1986) 527–531.

[43] G.R. Odette, G.E. Lucas and R. Maiti, J. Nucl. Mater. 148 (1987) 22–27.

[44] G.R. Odette, G.E. Lucas, R. Maiti and J.W. Sheckherd, J. Nucl. Mater. 122 & 123 (1984) 442–447.

[45] R.A. Wullaert, D.R. Ireland and A.S. Tetelman, in: Irradiation Effects on Structural Alloys for Nuclear Reactor Applications, ASTM STP 484, American Society for Testing and Materials, 1970, pp. 20–41.

[46] B.S. Louden, A.S. Kumar, F.A. Garner, M.L. Hamilton and W.L. Hu, J. Nucl. Mater. 155–157 (1988) 662–667.

[47] E. Lucon and A. Almazouzi, Mechanical response to irradation at 200°C for EM10, T91 and HT9 – Final Report: Specimens Irradiated to 2.6 and 3.9 dpa, SCK•CEN Report BLG-986, 2004.

[48] N. Hashimoto, S.J. Zinkle, R.L. Klueh, A.F. Rowcliffe and K. Shiba, Mat. Res. Soc. Symp. Proc., Vol. 650, 2001, pp. R1.10.1–6.

[49] R.L. Fish, J.L. Straalsund, C.W. Hunter and J.J. Holmes, in: Effects of Radiation on Substructure and Mechanical Properties of Metals and Alloys, ASTM STP 529, American Society for Testing and Materials, 1973, pp. 149–164.

[50] C.W. Hunter, R.L. Fish and J.J. Holmes, Trans. Amer. Nucl. Soc. 15 (1972) 254–255.

[51] R.L. Fish and C.W. Hunter, in: Irradiation Effects on the Microstructure and Properties of Metals, ASTM STP 611, American Society for Testing and Materials, 1976, pp. 119–138.

[52] K. Onizawa and M. Suzuki, in: Effect of Radiation on Materials: 20th International Symposium, ASTM STP 1405, S.T. Rosinski, M.L. Grossbeck, T.R. Allen, and A.S. Kumar, Eds., American Society for Testing and Materials, 2001, pp. 79–96.

[53] M. Kirk and M. Natishan, Shift in toughness transition temperature due to irradiation: DT0 vs. DT41J, a comparison and rationalization of differences, Proceedings of the IAEA Specialists Meeting on Master Curve Technology, Prague, Czech Republic, 2001

[54] A.L. Hiser, in: Influence of Radiation on Material Properties: 13th International Symposium, , ASTM STP 956, Part II, F.A. Garner, C.H. Henager, Jr., and N. Igata, Eds., American Society for Testing and Materials, 1987, pp. 333–357.

[55] F.J. Schmitt, in: Effect of Radiation on Materials: 14th International Symposium, ASTM STP 1046, Vol. II, N.H. Packan, R.E. Stoller, and A.S. Kumar, Eds., American Society for Testing and Materials, 1990, pp. 373–384.

[56] D.R. Olander, Fundamentals aspects of nuclear reactor fuel elements, TI-26711-P1, 1976.

[57] A.L. Bement, Jr., in: Second International Conference on the Strength of Metals and Alloys, Vol. 3, The American Society for Metals, 1970, pp. 693–728.

[58] L.M. Brown, Proc. 5th Int. Conf. Str. Met. Alloys 3 (1979) 1551–1560.

[59] U.F. Kocks Mat. Sci. Eng. 27 (1977) 291–298.

[60] G.R. Odette, P.M. Lombrozo and R.A. Wullaert, in: Effect of Radiation on Materials: 12th International Symposium, ASTM STP 870, F.A. Garner and J.S. Perrin, Eds., American Society for Testing and Materials, 1985, pp. 840–860.

[61] G.E. Lucas, G.R. Odette, P.M. Lombrozo, and J.W. Sheckherd, in: Effect of Radiation on Materials: 12th International Symposium, ASTM STP 870, F.A. Garner and J.S. Perrin, Eds., American Society for Testing and Materials, 1985, pp. 900–930.

[62] R.J. Amodeo and N.M. Ghoniem, Nucl. Eng. Des. / Fus. 2 (1985) 97–110.

[63] W.L. Server, J. Test. Eval. 6 (1978) 29–34.

[64] A. Fabry, E. van Walle, R. Chaouadi, J.P. Wannijn, A. Verstrepen, J.L. Puzzolante, T. Van Ransbeeck and J. Van de Velde, in: IAEA/OECD Specialists Meeting on Irradiation Embrittlement and Optimization of Annealing, 1993, Paris, and SCK•CEN Report BLG–649, 1993.

[65] G.D. Fearnehough, In: Physical Basis of Yield and Fracture, Institute of Physics and Physical Society, Oxford, 1966, pp. 88–99.

[66] R. Chaouadi, in: From Charpy to Present Impact Testing, D. François and A. Pineau, Eds., Elsevier, 2002, pp. 103–117.

[67] H. Conrad, J. Met. 67 (1964) 582–588.

[68] J. Böhmert and G. Müller, J. Nucl. Mater. 301 (2002) 227–232.

[69] E.A. Little, Phys. Stat. Sol. A 3 (1970) 983–994.

[70] P. Soo, Trans. Met. Soc. AIME 245 (1969) 985–990.

[71] F.A. Smidt, Jr., Acta Met. 17 (1969) 381–392.

[72] K. Ono, J. Appl. Phys. 39 (1968) 1803–1806.

[73] R.J. Arsenault, Acta Met. 15 (1967) 1853–1859.

[74] A. Seeger, Zeitsch.. Metallk. 72 (1981) 369–380.

[75] G.E. Lucas and G.R. Odette, Nucl. Eng. Des. / Fus. 2 (1985) 145–173.

[76] R. Chaouadi, Work hardening evaluation of polycrystalline materials, SCK•CEN Report R–4102, 2005.

[77] H. Tanigawa, H. Sakasegawa, N. Hashimoto, R.L. Klueh, M. Ando and M.A. Sokolov, J. Nucl. Mater. 367–370 (2007) 42–47.

[78] H. Tanigawa, N. Hashimoto, H. Sakasegawa, R.L. Klueh, M.A. Sokolov, K. Shiba, S. Jitsukawa and A. Kohyama, J. Nucl. Mater. 329–333 (2004) 283–288.

[79] J. Henry, L. Vincent, X. Averty, B. Marini and P. Jung, J. Nucl. Mater. 367–370 (2007) 411–416.

[80] S.B. McRickard, Acta Met. 16 (1968) 969–974.

[81] R.L. Klueh and D.J. Alexander, J. Nucl. Mater. 212–215 (1994) 736–740.

[82] G.E. Lucas and D.S. Gelles, J. Nucl. Mater. 155–157 (1988) 164–177.

[83] R.L. Klueh, K. Ehrlich and F. Abe, J. Nucl. Mater. 191–194 (1992) 116–124.

[84] R.E. Clausing, L. Heatherly, R.G. Faulkner, A.F. Rowcliffe and K. Farrell, J. Nucl. Mater. 141–143 (1986) 978–981.

[85] N.S. Cannon and D.S. Gelles, J. Nucl. Mater. 186 (1991) 68–76.

[86] G.R. Odette and G.E. Lucas, J. Nucl. Mater. 117 (1983) 264–275.

[87] R.L. Klueh, J.J. Kai and D.J. Alexander, J. Nucl. Mater. 225 (1995) 175–186.

[88] R.L. Klueh and D.J. Alexander, J. Nucl. Mater. 187 (1992) 60–69.

[89] R.L. Klueh, D.J. Alexander and P.J. Maziasz, J. Nucl. Mater. 186 (1992) 185–195.

[90] R.L. Klueh and D.J. Alexander, J. Nucl. Mater. 265 (1999) 262–272.

[91] R.L. Klueh and D.J. Alexander, J. Nucl. Mater. 233–237 (1996) 336–341.

[92] R.L. Klueh and D.J. Alexander, in: Effect of Radiation on Materials: 18th International Symposium, ASTM STP 1325, R.K. Nanstad, M.L. Hamilton, F.A. Garner, and A.S. Kumar, Eds., American Society for Testing and Materials, 1999, pp. 911–930.

[93] R. Chaouadi, J. Nucl. Mater. 372 (2008) 379–390

[94] M.S. Wechsler, Radiation effects, diffusion and body–centered cubic metals, in: Diffucion in Body–Centered Cubic Metals, American Society for Metals, 1965, pp. 291–315.

[95] G.J. Dienes and A.C. Damask, Radiation enhanced diffusion in solids, in: Metallurgy and Fuels, Vol. 3, H.M. Finniston and J.P. Howe, Eds., 1961, pp. 161–177.

[96] P. Jung, Production of atomic defects in metals, in Atomic Defects in Metals, Vol. 25, H. Ullmaier, Ed., Landolt–Börnstein, 1991, 1–87.

[97] L.K. Mansur and M.L. Grossbeck, J. Nucl. Mater. 155–157 (1988) 130–147.

[98] A. Alamo, J.L. Séran, O. Rabouille, J.C. Brachet, A. Maillard, H. Touron and J. Royer, in: Effect of Radiation on Materials: 17th International Symposium, ASTM STP 1270, D.S. Gelles, R.K. Nanstad, and A.S. Kumar, Eds., American Society for Testing and Materials, 1996, pp. 761–774.

[99] K.K. Bae, K. Ehrlich and A. Möslang, J. Nucl. Mater. 191–194 (1992) 905–909.

[100] A. Möslang and D. Preininger, J. Nucl. Mater. 155–157 (1988) 1064–1068.

[101] G.R. Odette, J. Nucl. Mater. 133–134 (1985) 127–133.

[102] R.L. Klueh and D.R. Harries, High–chromium ferritic and martensitic steels for nuclear applications, American Society for Testing and Materials, 2001.

[103] D. Gilbon, J.L. Séran, R. Cauvin, A. Fissolo, A. Alamo, F. Le Naour and V. Lévy, in: Effect of Radiation on Materials: 14th International Symposium, ASTM STP 1046, N.H. Packan, R.E. Stoller, and A.S. Kumar, Eds., American Society for Testing and Materials, 1989, pp. 5–34.

[104] R.L. Klueh, Elevated–temperature ferritic and martensitic steels and their application to future nuclear reactors, ORNL/TM-2004/176, 2004.

[105] J.L. Séran, V. Lévy, P. Dubuisson, D. Gilbon, A. Maillard, A. Fissolo, H. Touron, R. Cauvin, A. Chalony and E. Le Boulbin, in: Effect of Radiation on Materials: 15th International Symposium, ASTM STP 1125, R.E. Stoller, A.S. Kumar, and D.S. Gelles, Eds., American Society for Testing and Materials, 1992, pp. 1209–1233.

[106] P. Dubuisson, D. Gilbon and J.L. Séran, J. Nucl. Mater. 205 (1993) 178–189.

[107] J.C. Brachet, X. Averty, P. Lamagnère, A. Alamo, F. Rozenblum, O. Raquet and J.L. Bertin, in: Effect of Radiation on Materials: 20th International Symposium, ASTM STP 1405, S.T. Rosinski, M.L. Grossbeck, T.R. Allen, and A.S. Kumar, Eds., American Society for Testing and Materials, 2001, pp. 500–520.

[108] E.I. Materna-Morris, M. Rieth and K. Ehrlich, in: Effect of Radiation on Materials: 19th International Symposium, ASTM STP 1366, M.L. Hamilton, A.S. Kumar, S.T. Rosinski, and M.L. Grossbeck, Eds., American Society for Testing and Materials, 2000, pp. 597–611.

[109] X. Averty, J.C. Brachet, J.P. Pizzanelli and A. Castaing, in International Symposium on the Contribution of Materials Investigation to the Resolution of Problems Encountered in Pressurized Water Reactors, Fontevraud–IV, Vol. 1, 1998, pp. 293–306.

[110] J. Gan, T.R. Allen, J.I. Cole, S. Ukai, S. Shutthanandan and S. Thevuthasan, Mat. Res. Soc. Symp. Proc. Vol. 792, 2004, pp. R1.7.1–6.

[111] Y. Dai, X.J. Jia and K. Farrell, J. Nucl. Mater. 318 (2003) 192–199.

[112] K. Farrell and T.S. Byun, J. Nucl. Mater. 318 (2003) 274–282.

[113] J. Henry, X. Averty, Y. Dai, P. Lamagnère, J.P. Pizzanelli, J.J. Espinas and P. Wident, J. Nucl. Mater. 318 (2003) 215–227.

[114] X. Jia and Y. Dai, J. Nucl. Mater. 318 (2003) 207–214.

[115] Y. Jia and X. Jia, J. Nucl. Mater. 323 (2003) 360–367.

[116] T.S. Byun, K. Farrell, E.H. Lee, L.K. Mansur, S.A. Maloy, M.R. James and W.R. Johnson, J. Nucl. Mater. 303 (2002) 34–43.

[117] X. Jia, Y. Dai and M. Victoria, J. Nucl. Mater. 305 (2002) 1–7.

[118] R.L. Klueh and A.T. Nelson, J. Nucl. Mater. 371 (2007) 37–52.

[119] P. Vladimirov and A. Möslang, J. Nucl. Mater. 283–333 (2004) 233–237.

[120] D.R. Harries, G.J. Butterworth, A. Hishinuma and F.W. Wiffen, J. Nucl. Mater. 191–194 (1992) 92–99.

[121] M.L. Hamilton, L.E. Schubert and D.S. Gelles, in: Effect of Radiation on Materials: 18th International Symposium, ASTM STP 1325, R.K. Nanstad, M.L. Hamilton, F.A. Garner, and A.S. Kumar, Eds., American Society for Testing and Materials, 1999, pp. 931–944.

[122] D.S. Gelles and M.L. Hamilton, J. Nucl. Mater. 148 (1987) 272–278.

[123] A. Kimura, H. Kayano, T. Misawa and H. Matsui, J. Nucl. Mater. 212–215 (1994) 690–694.

[124] F. Abe, T. Noda, H. Araki and S. Nakazawa, J. Nucl. Mater. 179–181 (1991) 663–666.

[125] R.L. Klueh, D.S. Gelles and T.A. Lechtenberg, J. Nucl. Mater. 141–143 (1986) 1081–1087.

[126] B. van der Schaaf, F. Tavassoli, C. Fazio, E. Rigal, E. Diegele, R. Lindau and G. LeMarois, Fus. Eng. Des. 69 (2003) 197–203.

[127] A. Hishinuma, A. Kohyama, R.L. Klueh, D.S. Gelles, W. Dietz and K. Ehrlich, J. Nucl. Mater. 258–263 (1998) 193–204.

[128] A. Kohyama, A. Hishinuma, D.S. Gelles, R.L. Klueh, W. Dietz and K. Ehrlich, J. Nucl. Mater. 233–237 (1996) 138–147.

[129] E. Gaganidze, H.C. Schneider, B. Dafferner and J. Aktaa, J. Nucl. Mater. 355 (2006) 83–88.

[130] E. Lucon, R. Chaouadi and M. Decréton, J. Nucl. Mater. 329–333 (2004) 1078–1082.

[131] J. Rensman, E. Lucon, J. Boskeljon, J. van Hoepen, R. den Boef and P ten Pierick, J. Nucl. Mater. 329–333 (2004) 1113–1116.

[132] A.A. Tavassoli et al., J. Nucl. Mater. 329–333 (2004) 257–262.

[133] E. Lucon et al., Fus. Eng. Des. 81 (2006) 917–923.

[134] A.A. Tavassoli, Fus. Eng. Des. 61 (2002) 617–628.

[135] A. Kohyama, A. Hishinuma, Y. Kohno, K Shiba and A. Sagara, Fus. Eng. Des. 41 (1998) 1–6.

[136] R. Andreani, E. Diegele, R. Laesser and B. van der Schaaf, J. Nucl. Mater. 329–333 (2004) 20–30.

[137] S. Jitsukawa, A. Kimura, A. Kohyama, R. L. Klueh, A. A. Tavassoli, B. van der Schaaf, G. R. Odette, J. W. Rensman, M. Victoria and C. Petersen, J. Nucl. Mater. 329–333 (2004) 39–46.

[138] R. Lindau, A. Möslang and M. Schirra, Fus. Eng. Des. 61–62 (2002) 659–664.

[139] J. Rensman, H. E. Hofmans, E. W. Schuring, J. van Hoepen, J. B. M. Bakker, R. den Boef, F. P. van den Broek and E. D. L. van Essen, J. Nucl. Mater. 307–311 (2002) 250–255.

[140] R. Lindau and M. Schirra, Fus. Eng. Des. 58–59 (2001) 781–785.

[141] A. Alamo, J.L. Bertin, V.K. Shamardin and P. Wident, J. Nucl. Mater. 367–370 (2007) 54–59.

[142] E. Wakai, M. Ando, T. Sawai, K. Kikuchi, K. Furuya, M. Sato, K. Oka, S. Ohnuki, H. Tomita, T. Tomita, Y. Kato and F. Takada, J. Nucl. Mater. 356 (2006) 95–104.

[143] E. Wakai, S. Jitsukawa, H. Tomita, K. Furuya, M. Sato, K. Oka, T. Tanaka, F. Takada, T. Yamamoto, Y. Kato, Y. Tayama, K. Shiba and S. Ohnuki, J. Nucl. Mater. 343 (2005) 285–296.

[144] Y. Dai, X. Jia and S.A. Maloy, J. Nucl. Mater. 343 (2005) 241–246.

[145] A. Kimura, Mat. Trans. 46 (2005) 394–404.

[146] H. Tanigawa, H. Sakasegawa and R.L. Klueh, Mat. Trans. 46 (2005) 469–474.

[147] K. Shiba, M. Enoeda and S. Jitsukawa, J. Nucl. Mater. 329–333 (2004) 243–247.

[148] E. Wakai, T. Taguchi, T. Yamamoto and F. Takada, J. Nucl. Mater. 329–333 (2004) 1133–1136.

[149] H. Tanigawa, K. Shiba, M.A. Sokolov and R.L. Klueh, Fus. Sci. Techno. 44 (2003) 206–210.

[150] S. Jitsukawa, M. Tamura, B. van der Schaaf, R. L. Klueh, A. Alamo, C. Petersen, M. Schirra, P. Spaetig, G. R. Odette, A. A. Tavassoli, K. Shiba, A. Kohyama and A. Kimura, J. Nucl. Mater. 307–311 (2002) 179–186.

[151] A. Kimura, T. Sawai, K. Shiba, A. Hishinuma, S. Jitsukawa, S. Ukai and A. Kohyama, 19th Fusion Energy Conference, IAEA-CN-94 (2002) FT1/1–5.

[152] K. Shiba and A. Hishinuma, J. Nucl. Mater. 283–287 (2000) 474–477.

[153] K. Shiba, R. L. Klueh, Y. Miwa, J. P. Robertson and A. Hishinuma, J. Nucl. Mater. 283–287 (2000) 358–361.

[154] K. Shiba, M. Suzuki and A. Hishinuma, J. Nucl. Mater. 233–237 (1996) 309–312.

[155] Y. Kohno, D. S. Gelles, A. Kohyama, M. Tamura and A. Hishinuma, J. Nucl. Mater. 191–194 (1992) 868–873.

[156] R.L. Klueh, N. Hashimoto, M.A. Sokolov, K. Shiba and S. Jitsukawa, J. Nucl. Mater. 357 (2006) 156–168.

[157] N. Hashimoto, S.J. Zinkle, R.L. Klueh, A.F. Rowcliffe and K. Shiba, Mat. Res. Soc. Sympo. Proc. Vol. 650 (2001) R3.6.1–6.

[158] S.A. Maloy, M.R. James, G. Willcutt, W.F. Sommer, M. Sokolov, L.L. Snead, M.L. Hamilton and F. Garner, J. Nucl. Mater. 296 (2001) 119–128.

[159] R.L. Klueh, M.A. Sokolov, K. Shiba, Y. Miwa and J.P. Robertson, J. Nucl. Mater. 283–287 (2000) 478–482.

[160] R.L. Klueh and D.J. Alexander, J. Nucl. Mater. 258–263 (1998) 1269–1274.

[161] R.L. Klueh and P.J. Maziasz, J. Nucl. Mater. 187 (1992) 43–54.

[162] R.L. Klueh and D.J. Alexander, J. Nucl. Mater. 179–181 (1991) 733–736.

[163] R.L. Klueh and J.M. Vitek, J. Nucl. Mater. 182 (1991) 230–239.

[164] R. Lindau, A. Möslang, D. Preininger, M. Rieth and H. D. Röhrig, J. Nucl. Mater. 271–272 (1999) 450–454.

[165] P. Jung, J. Chen and H. Klein, J. Nucl. Mater. 356 (2006) 88–94.

[166] S.A. Maloy, M.B. Toloczko, K.J. McClellan, T. Romero, Y. Kohno, F.A. Garner, R.J. Kurtz and A. Kimura J. Nucl. Mater. 356 (2006) 62–69.

[167] P. Jung, J. Henry and J. Chen, J. Nucl. Mater. 343 (2005) 275–284.

[168] P. Jung, J. Henry, J. Chen nad J.C. Brachet, J. Nucl. Mater. 318 (2001) 241–248.

[169] V.K. Shamardin, V.N. Golovanov, T.M. Bulanova, A.V. Povstyanko, A.E. Fedoseev, Z.E. Ostrovsky and Y.D. Goncharenko, J. Nucl. Mater. 307–311 (2002) 229–235.

[170] K. Farrell and T.S. Byun, J. Nucl. Mater. 296 (2001) 129–138.

[171] H.C. Schneider, B. Dafferner and J. Aktaa, J. Nucl. Mater. 295 (2001) 16–20.

[172] H.C. Schneider, B. Dafferner, H. Ries and O. Romer, Bestrahlungsprogramm MANITU: Ergebnisse der Kerbschlagbiegeversuche mit den bis 2.4 dpa bestrahlten Werkstoffen, FZKA–6605, 2001.

[173] H.C. Schneider, B. Dafferner, H. Ries, S. Lautensack and O. Romer, Bestrahlungsprogramm HFR: Ergebnisse der Kerbschlagbiegeversuche mit den bis 2.4 dpa bestrahlten Werkstoffen, FZKA–6976, 2004.

[174] R. Kasada, A. Kimura, H. Matsui, M. Hasegawa and M. Narui, J. Nucl. Mater. 271–272 (1999) 360–364.

[175] Y. Kohno, A. Kohyama, T. Hirose, M.L. Hamilton and M. Narui, J. Nucl. Mater. 271–272 (1999) 145–150.

[176] I. Belianov and P. Marmy, J. Nucl. Mater. 258–263 (1998) 1259–1263.

[177] H. Kurishita, H. Kayano, M. Narui, A. Kimura, M.L. Hamilton and D.S. Gelles, J. Nucl. Mater. 212–215 (1994) 730–735.

[178] F. Abe, M. Narui and H. Kayano, Mat. Trans. JIM 34 (1993) 1053–1060.

[179] P. Marmy and M. Victoria, J. Nucl. Mater. 191–194 (1992) 862–867.

[180] R.L. Klueh and J.M. Vitek, J. Nucl. Mater. 161 (1989) 13–23.

[181] C. Fazio, A. Alamo, A. Almazouzi, D. Gomez-Briceno, F. Groeschel, F. Roelofs, P. Turroni and J. Knebel, in: Proc. Of GLOBAL, Tsukuba, Japan, 2005, Paper N°39.

[182] L.K. Mansur, A.F. Rowcliffe, R.K. Nanstad, S.J. Zinkle, W.R. Corwin and R.E. Stoller, J. Nucl. Mater. 329–333 (2004) 166–172.

[183] M. Samaras, W. Hoffelner and M. Victoria, J. Nucl. Mater. 371 (2007) 28–36.

[184] G. Benamati, P. Buttol, V. Imbeni, C. Martini and G. Palombarini, J. Nucl. Mater. 279 (2000) 308–316.

[185] Y. Dai, S. A. Maloy, G. S. Bauer and W. F. Sommer, J. Nucl. Mater. 283–287 (2000) 513–517.

[186] K.L. Murty and I. Charit, J. Nucl. Mater. (2008) (doi:10.1016/j.jnucmat.2007.09.029).

[187] F. Barbier, G. Benamati, C. Fazio and A. Rusanov, J. Nucl. Mater. 295 (2001) 149–156.

[188] V.K. Shamardin, V.N. Golovanov, T.M. Bulanova, A.V. Povstianko, A.E. Fedoseev, Y.D. Goncharenko and Z.E. Ostrovsky, J. Nucl. Mater. 271–272 (1999) 155–161.

[189] T. Noda, F. Abe, H. Araki and M. Okada, J. Nucl. Mater. 141–143 (1986) 1102–1106.

[190] P. Fernández, A. M. Lancha, J. Lapeña, M. Serrano and M. Hernández-Mayoral, J. Nucl. Mater. 307–311 (2002) 495–499.

[191] P. Fernández, A. M. Lancha, J. Lapeña and M. Hernández-Mayoral, Fus. Eng. Des. 58–59 (2001) 787–792.

[192] P. Fernández, M. Hernández-Mayoral, J. Lapeña, A.M. Lancha and G. De Diego, Mater. Sci. Techno. 18 (2002) 1353–1362.

[193] Y. Dai, G.S. Bauer, F. Carsughi, H. Ullmaier, S.A. Maloy and W.F. Sommer, J. Nucl. Mater. 265 (1999) 203–207.

[194] P.J. Maziasz and R.L. Klueh, in: Effect of Radiation on Materials: 14th International Symposium, ASTM STP 1046, Vol. I, N.H. Packan, R.E. Stoller, and A.S. Kumar, Eds., American Society for Testing and Materials, 1990, pp. 35–60.

[195] A. Kimura and H. Matsui, J. Nucl. Mater. 212–215 (1994) 701–706.

[196] F. Abe, T. Noda and M. Okada, J. Nucl. Mater. 195 (1992) 51–67.

[197] T. Shibayama, A. Kimura and H. Kayano, J. Nucl. Mater. 233 (1996) 270–275.

[198] H. Kayano, A. Kimura, M. Narui, T. Kikuchi and S. Ohta, J. Nucl. Mater. 179–181 (1991) 671–674.

[199] R.L. Klueh, J. Nucl. Mater. 179–181 (1991) 728–732.

[200] M. Gasparotto, R. Andreani, L. V. Boccaccini, A. Cardella, G. Federici, L. Giancarli, G. Le Marois, D. Maisonnier, S. Malang, A. Moeslang, Y. Poitevin, B. van der Schaaf and M. Victoria, Fus. Eng. Des. 66–68 (2003) 129–137.

[201] E. Daum and U. Fischer, Fus. Eng. Des. 49–50 (2000) 529–533.

[202] R. Lässer, N. Baluc, J.-L. Boutard, E. Diegele, S. Dudarev, M. Gasparotto, A. Möslang, R. Pippan, B. Riccardi and B. van der Schaaf, Fus. Eng. Des. 82 (2007) 511–520.

[203] R. Lindau et al., Fus. Eng. Des. 75–79 (2005) 989–996.

[204] R.L. Klueh and J.M. Vitek, J. Nucl. Mater. 132 (1985) 27–31.

[205] R.L. Klueh and J.M. Vitek, J. Nucl. Mater. 150 (1987) 272–280.

[206] H. Kayano, A. Kimura, M. Narui, Y. Sasaki, Y. Suzuki and S. Ohta, J. Nucl. Mater. 155–157 (1988) 978–981.

[207] J.C. Brachet, A. Castaing and C. Foucher, in: Materials Ageing and Component Life Extension, Vol. I, V. Bicego, A. Nitta, and R. Viswanathan, Eds., Eng. Mater. Adv. Serv. Ltd., 1995, pp. 75–87.

[208] K. Miyahara, Y. Kobayashi, Y. Hosoi and J. Nucl. Mater. 179–181 (1991) 667–670.

[209] F. Abe, H. Araki, T. Noda and M. Okada, J. Nucl. Mater. 155–157 (1991) 656–661.

[210] M.L. Hamilton and D.S. Gelles, in: Effect of Radiation on Materials: 15th International Symposium, ASTM STP 1125, R.E. Stoller, A.S. Kumar, and D.S. Gelles, Eds., American Society for Testing and Materials, 1992, pp. 1234–1242.

[211] T. Misawa, Y. Hamaguchi and M. Saito, J. Nucl. Mater. 155–157 (1988) 749–743.

[212] R.L. Klueh, P.J. Maziasz and D.J. Alexander, J. Nucl. Mater. 179–181 (1991) 679–683.

[213] K.W. Tupholme, D. Dulieu, G.J. Butterworth, J. Nucl. Mater. 179–181 (1991) 684–688.

[214] L. Schäfer, J. Nucl. Mater. 283–287 (2000) 707–710.

[215] R.L. Klueh and P.J. Maziasz, J. Nucl. Mater. 155–157 (1988) 602–607.

[216] L. Schäfer, M. Schirra and R. Lindau, in: Fusion Technology 1996, C. Varandas and F. Serra, Eds., Elsevier Science, 1997, pp. 1363–1366.

[217] M. Rieth, B. Dafferner, H.D. Röhrig and C. Wassilew, Fus. Eng. Des. 29 (1995) 365–370.

[218] L. Schäfer, M. Schirra and K. Ehrlich, J. Nucl. Mater. 233–237 (1996) 264–269.

[219] L. Schäfer, in: Fusion Technology 1996, C. Varandas and F. Serra, Eds., Elsevier Science, 1997, pp. 1367–1369.

[220] E. Wakai, M.Ando, T. Sawai, H. Tanigawa, T. Taguchi, R.E. Stoller, T. Yamamoto, Y. Kato and F. Takada, J. Nucl. Mater. 367–370 (2007) 74–80.

[221] S. Kunimitsu, Y. You, N. Kasuya, Y. Sasaki and Y. Hosoi, J. Nucl. Mater. 179 (1991) 689–692.

[222] P.J. Maziasz and R.L. Klueh, in: Effect of Radiation on Materials: 15th International Symposium, ASTM STP 1125, R.E. Stoller, A.S. Kumar, and D.S. Gelles, Eds., American Society for Testing and Materials, 1992, pp. 1135–1156.

[223] J. Lapeña, M. Garcia-Mazario, P. Fernández and A.M. Lancha, J. Nucl. Mater. 283–287 (2000) 662–666.

[224] R.W. Swindeman, P.J. Maziasz and C.R. Brinkman, in: Proceedings of the 2000 International Joint Power Generation Conférence, IJPGC2000-15050, ASME, 2000.

[225] D.S. Gelles, C.Y. Hsu and T.A. Lechtenberg, J. Nucl. Mater. 155–157 (1988) 902–907.

[226] C.Y. Hsu and T.A. Lechtenberg, J. N Nucl. Mater. 141–143 (1986) 1107–1112.

[227] P. Gondi, R. Montanari, A. Sili and M.E. Tata, J. Nucl. Mater. 233–237 (1996) 248–252.

[228] T. Hirose, K. Shiba, T. Sawai, S. Jitsukawa and M. Akiba, J. Nucl. Mater. 329–333 (2004) 324–327.

[229] G.E. Lucas, H. Yih and G.R. Odette, J. Nucl. Mater. 155–157 (1988) 673–678.

[230] R.L. Klueh, N. Hashimoto, M.A. Sokolov, P.J. Maziasz, K. Shiba and S. Jitsukawa, J. N Nucl. Mater. 357 (2006) 169–182.

[231] R. Kasada, A. Kimura, H. Matsui and M. Narui, J. Nucl. Mater. 258–263 (1998) 1199–1203.

[232] R.L. Klueh, P.J. Maziasz and J.M. Vitek, J. Nucl. Mater. 141–143 (1986) 960–965.

[233] M. Rieth, B. Dafferner, H.D. Röhrig, J. Nucl. Mater. 258–263 (1998) 1147–1152.

[234] A. Kimura, R. Kasada, K. Morishita, R. Sugano, A. Hasegawa, K. Abe, T. Yamamoto, H. Matsui, N. Yoshida, B. D. Wirth and T. D. Rubia, J. Nucl. Mater. 307–311 (2002) 521–526.

[235] M. Ando, H. Tanigawa, S. Jitsukawa, T. Sawai, Y. Katoh, A. Kohyama, K. Nakamura and H. Takeuchi, J. Nucl. Mater. 307–311 (2002) 260–265.

[236] N. Hashimoto, R.L. Klueh and K. Shiba, J. Nucl. Mater. 307–311 (2002) 222–228.

[237] R. Kasada, T. Morimura, A. Hasegawa and A. Kimura, J. Nucl. Mater. 299 (2001) 83–89.

[238] P.J. Maziasz, R.L. Klueh and J.M. Vitek, J. Nucl. Mater. 141–143 (1986) 929–937.

[239] D.S. Gelles, S. Ohnuki, K. Shiba, Y. Kohno, A. Kohyama, J.P. Robertson and M.L. Hamilton, Fusion Materials Semi–Annual Progress Report, DOE/ER-0313/25, 1999, pp. 143–150.

[240] L.R. Greenwood, D.G. Graczyk and D.W. Kneff , J. Nucl. Mater. 155–157 (1988) 1335–1339.

[241] L.R. Greenwood, J. ASTM Int. 3 (2006).

[242] M. Suzuki, A. Hishinuma, N. Yamanouchi, M. Tamura and A.F. Rowcliffe, J. Nucl. Mater. 191–194 (1992) 1056–1059.

[243] D.S. Gelles, M.L. Hamilton, B.M. Oliver, L.R. Greenwood, S. Ohnuki, K. Shiba, Y. Kohno, A. Kohyama and J.P. Robertson, J. Nucl. Mater. 307–311 (2002) 212–216.

[244] M.H. Mathon, Y. de Carlan, G. Geoffroy, X. Averty, A. Alamo and C.H. de Novion, J. Nucl. Mater. 312 (2003) 236–248.

[245] J.J. Kai and R.L. Klueh, J Nucl. Mater. 230 (1996) 116–123.

[246] H. Ogiwara, A. Kohyama, H. Tanigawa and H. Sakasegawa, J. Nucl. Mater. 367–370 (2007) 428–433.

[247] H. Tanigawa, H. Sakasegawa, H. Ogiwara, H. Kishimoto and A. Kohyama, J. Nucl. Mater. 367–370 (2007) 132–136.

[248] R. Schäublin and M. Victoria, J. Nucl. Mater. 283–287 (2000) 339–343.

[249] B.H. Sencer, F.A. Garner, D.S. Gelles, G.M. Bond and S.A. Maloy, J. Nucl. Mater. 307–311 (2002) 266–271.

[250] M. Ando, E. Wakai, T. Sawai, H. Tanigawa, K. Furuya, S. Jitsukawa, H. Takeuchi, K. Oka, S. Ohnuki and A. Kohyama, J. Nucl. Mater. 329–333 (2004) 1137–1141.

[251] H. Ullmaier and E. Camus, J. Nucl. Mater. 251 (1997) 262–268.

[252] X. Jia and Y. Dai, J. Nucl. Mater. 329–333 (2004) 309–313.

[253] N. Hashimoto and R.L. Klueh, J. Nucl. Mater. 305 (2002) 153–158.

[254] H. Trinkaus, J. Nucl. Mater. 133–134 (1985) 105–112.

[255] H. Trinkaus and H. Ullmaier, Phil. Mag. 39 (1979) 563–580.

[256] H. Schröder, Rad. Eff. 78 (1983) 297–314.

[257] N.M. Ghoniem, J. Nucl. Mater. 174 (1990) 168–177.

[258] L.K. Mansur and W.A. Coghlan, J. Nucl. Mater. 119 (1983) 1–25.

[259] R.E. Stoller and G.R. Odette, in: Effects of Radiation on Materials, 11th Conference, ASTM STP 782, H.R. Brager and J.S. Perrin, Eds., (1982) pp. 275–294.

[260] N.M Ghoniem and M.L. Takata, J. Nucl. Mater. 105 (1982) 276–292.

[261] R.E. Stoller and R.G. Odette, in: Radiation Induced Changes in Microstructure: 13th International Symposium (Part I), ASTM STP 955, F.A. Garner, N.H. Packan, and A.S. Kumar, Eds., American Society for Testing and Materials, 1987, pp. 371–392.

[262] L.K. Mansur, Nucl. Techno. 40 (1978) 5–34.

[263] H. Ullmaier, Nucl. Fus. 24 (1984) 1039–1083.

[264] H. Ullmaier, J. Nucl. Mater. 133 (1985) 100–104.

[265] B.N. Singh and H. Trinkaus, J. Nucl. Mater. 186 (1992) 153–165.

[266] D.G. Doran, F.M. Mann and L.R. Greenwood, J. Nucl. Mater. 174 (1990) 125–134.

[267] P. Jung, J. Nucl. Mater. 301 (2002) 15–22.

[268] U. Fischer, S.P. Simakov and P.P.H. Wilson, J. Nucl. Mater. 329–333 (2004) 228–232.

[269] P. Jung, C. Liu and J. Chen, J. Nucl. Mater. 296 (2001) 165–173.

[270] R.L. Klueh, Curr. Opin. Sol. Sta. Mater. Sci. 8 (2004) 239–250.

[271] H. Ullmaier and H. Trinkaus, Mat. Sci. For. 97–99 (1992) 451–472.

[272] H. Ullmaier, Helium in metals, in Atomic Defects in Metals, Vol. 25, H. Ullmaier, Ed., Landolt–Börnstein, 1991, 380–435.

[273] A. Möslang, V. Heinzel, H. Matsui and M. Sugimoto, Fus. Eng. Des. 81 (2006) 863–871.

[274] D.S. Gelles, G.L. Hankin and M.L. Hamilton, J. Nucl. Mater. 251 (1997) 188–199.

[275] T. Yamamoto, G.R. Odette, P. Miao, D.T. Hoelzer, J. Bentley, N. Hashimoto, H. Tanigawa and R.J. Kurtz, J. Nucl. Mater. 367–370 (2007) 399–410.

[276] M.A. Sokolov, A. Kimura, H. Tanigawa and S. Jitsukawa, J. Nucl. Mater. 367–370 (2007) 644–647.

[277] M.A. Sokolov, H. Tanigawa, G.R. Odette, K. Shiba and R.L. Klueh, J. Nucl. Mater. 367–370 (2007) 68–73.

[278] E.V. van Osch, M. Horsten, G.E. Lucas and G.R. Odette, in: Effect of Radiation on Materials: 19th International Symposium, ASTM STP 1366, M.L. Hamilton, A.S. Kumar, S.T. Rosinski, and M.L. Grossbeck, Eds., American Society for Testing and Materials, 2000, pp. 612–625.

[279] J. Rensman, NRG irradiation testing: Report on 300°C and 60°C irradiated RAFM steels, NRG20023/05.68497/P, 2005.

[280] Y. Dai and G.S. Bauer, J. Nucl. Mater. 296 (2001) 43–53.

[281] F. Abe, T. Noda, H. Araki, M. Narui and H. Kayano, J. Nucl. Mater. 191–194 (1992) 845–849.

[282] M. Rieth and B. Dafferner, J. Nucl. Mater. 233–237 (1996) 229–232.

[283] M. Rieth, B. Dafferner and H.D. Röhrig, J. Nucl. Mater. 233–237 (1996) 351–355.

[284] K. Sawada, T. Ohba, H. Kushima and K. Kimura, Mater. Sci. Eng. A394 (2005) 36–42.

[285] M.I. Zakharova, N.A. Artemov and D.V. Petrov, J. Nucl. Mater. 233–237 (1996) 280–284.

[286] K. Shiba, N. Yamanouchi and A. Tohyama, Fusion Materials Semi–Annual Progress Report, DOE/ER-0313/20, 1996, pp. 190–194.

[287] J.R. Davis, Tensile testing, Second Edition, ASM International, 2004.

[288] H. Trinkaus and B.N. Singh, J. Nucl. Mater. 323 (2003) 229–242.

[289] A. Kimura, R. Kasada, A. Kohyama, H. Tanigawa, T. Hirose, K. Shiba, S. Jitsukawa, S. Ohtsuka, S. Ukai, M.A. Sokolov, R.L. Klueh, T. Yamamoto and G.R. Odette, J. Nucl. Mater. 367–370 (2007) 60–67.

[290] J. Moteff, D.J. Michel and V.K. Sikka, in:, Proceedings of the International Conference on Defects and Defect Clusters in BCC Metals and their Alloys, National Bureau of Standards, 1973, pp. 198–215.

[291] R.E. Stoller and S.J. Zinkle, J. Nucl. Mater. 283–287 (2000) 349–352.

[292] S.J. Zinkle and Y. Matsukawa, J. Nucl. Mater. 329–333 (2004) 88–96.

[293] R. Schaüblin, D.S. Gelles and M. Victoria, J. Nucl. Mater. 307–311 (2002) 197–202.

[294] J. Henry, P. Jung, J. Chen and J.C. Brachet, J. Phys. IV France 12 (2002) Pr8-103–120.

[295] D. Pachur, in: Irradiation Embrittlement, Thermal Annealing and Surveillance of Reactor Pressure Vessels, IAEA Meeting, Vienna 26 Feb. – 1 Mar. 1979, pp. 200–205.

[296] D. Pachur, in: Effects of Radiation on Materials, 10th Conference, ASTM STP 725, D. Kramer, H.R. Brager, and J.S. Perrin, Eds., American Society for Testing and Materials, 1981, pp. 5–19

[297] D. Pachur, Nucl. Techno. 59 (1982) 463–475.

[298] A.P. Main and B.L. Shriver, Nucl. Techno. 59 (1982) 456–462.

[299] B.L. Shriver, A.P. Main and D.C. Hicks, in: Effects of Radiation on Materials, 11th Conference, ASTM STP 782, H.R. Brager and J.S. Perrin, Eds., American Society for Testing and Materials, 1982, pp. 492–504.

[300] G. Gupta, Z. Jiao, A.N. Ham, J.T. Busby and G.S. Was, J. Nucl. Mater. 351 (2006) 162–173.

[301] K. Farrell, P.J. Maziasz, E.H. Lee and L.K. Mansur, Rad. Eff. 78 (1983) 277–295.

[302] A. Whapham and M.J. Makin, Phil. Mag. 5 (1960) 237–250.

[303] C.C. Dollins, Rad. Eff. 16 (1972) 271–280.

[304] D.J. Harvey and M.S. Wechsler, in: Effects of Radiation on Materials, 11th Conference, ASTM STP 782, H.R. Brager and J.S. Perrin, Eds., American Society for Testing and Materials, 1982, pp. 505–519.

[305] E.A. Little and D.R. Harries, in: Irradiation Effects in Structural Alloys for Thermal and Fast Reactors, ASTM STP 457, American Society for Testing and Materials, 1969, pp. 215–240.

[306] J.A. Brinkman and H. Wiedersich, in: Flow and Fracture of Metals and Alloys in Nuclear Environments, ASTM STP 380, American Society for Testing and Materials, 1965, pp. 3–39.

[307] G.J. Dienes and G.H. Vineyard, Radiation Effects in Solids, Interscience Pub. Ltd. (1957) 129–181.

[308] R.A. Johnson, in: Proceedings of the International Conference on Defect and Defect Clusters in BCC Metals and Their Alloys, National Bureau of Standards, 1973, pp. 565–580.

[309] E. Daum, K. Ehrlich and M. Schirra, The development of ferritic/martensitic steels for fusion technology, Proceedings of the 2nd Milestone Meeting of European Laboratories, Kalsruhe, FZKA-5848, 1997, pp. 53–56.

[310] A. Alamo, M. Horsten, X. Averty, E. I. Materna-Morris, M. Rieth and J. C. Brachet, J. Nucl. Mater. 283–287 (2000) 353–357.

[311] N. Baluc, R. Schäublin, C. Bailat, F. Paschoud and M. Victoria, J. Nucl. Mater. 283–287 (2000) 731–735.

[312] H. Trinkaus, J. Nucl. Mater. 318 (2003) 234–240.

[313] J.H. Evans, in Fundamental Aspects of Inert Gases in Solids, S.E. Donnelly and J.H. Evans, Eds., NATO ASI Series Vol. 279 (1991) 307–319.

[314] N.M. Ghoniem, S. Sharafat, J.M. Williams and L.K. Mansur, J. Nucl. Mater. 117 (1983) 96–105.

[315] J.E. Foreman and M.J. Makin, Can J Phys 45 (1967) 511–517.

[316] L.M. Brown and R.K. Ham, Dislocation–particle interactions, in: Strengthening Methods in Crystals, A. Kelly and R.B. Nicholson, Eds., Applied Science Publishers Ltd., 1971, pp. 9–135.

[317] L. Malerba, Multi–scale modeling and modeling–oriented experiments, SCK•CEN Report R–3709, (2003).

[318] G.R. Odette and G.E. Lucas, Rad. Eff. Def. Sol. 144 (1998) 189–231.

[319] R.L. Klueh, J.M. Vitek, W.R. Corwin and D.J. Alexander, J. Nucl. Mater. 155–157 (1988) 973–977.

[320] R.L. Klueh and M.A. Sokolov, J. Nucl. Mater. 367–370 (2007) 102–106.

[321] R.L. Klueh, J.M. Vitek and M.L. Grossbeck, in: Effects of Radiation on Materials, 11th Conference, ASTM STP 782, H.R. Brager and J.S. Perrin, Eds., (1982) pp. 648–664.

[322] S. Ishino and N. Sekimura, J. Nucl. Mater. 174 (1990) 158–167.

[323] P. Jung and H. Ullmaier, J. Nucl. Mater. 174 (1990) 253–263.

[324] R.L. Klueh and J.M. Vitek, J. Nucl. Mater. 117 (1983) 295–302.

[325] M. Tamura, H. Hayakawa, M. Tanimura, A. Hishinuma and T. Kondo, J. Nucl. Mater. 141 (1986) 1067–1073.

[326] E. Gaganidze, H.-C. Schneider, B. Dafferner and J. Aktaa, J. Nucl. Mater. 367–370 (2007) 81–85.

[327] C. Petersen et al., 21st IAEA Fusion Energy Conference, FEC 2006, Chengdu, China, 2006, FT/1-4Ra.

[328] P. Spätig, R. Schäublin, S. Gyger and M. Victoria, J. Nucl. Mater. 258–263 (1998) 1345–1349.

[329] A. Kimura, M. Narui, T. Misawa, H. Matsui and A. Kohyama, J. Nucl. Mater. 258–263 (1998) 1340–1344.

[330] E. Lucon, Mechanical properties of the European reference RAFM steel (EUROFER-97) before and after irradiation at 300°C (0.3–2 dpa), SCK•CEN Report BLG-962 (2003).

[331] T. Lechtenberg, J. Nucl. Mater. 133–134 (1985) 149–155.

[332] M.G. Horsten, E.V. van Osch, D.S. Gelles and M.L. Hamilton, in: Effect of Radiation on Materials: 19th International Symposium, ASTM STP 1366, M.L. Hamilton, A.S. Kumar, S.T. Rosinski, and M.L. Grossbeck, Eds., American Society for Testing and Materials, 2000, pp. 579–593.

[333] A. Kimura, T. Morimura, R. Kasada, H. Matsui, A. Hasegawa and K. Abe, , in: Effect of Radiation on Materials: 19th International Symposium, ASTM STP 1366, M.L. Hamilton, A.S. Kumar, S.T. Rosinski, and M.L. Grossbeck, Eds., American Society for Testing and Materials, 2000, pp. 626–641.

[334] A. Kimura, R. Kasada, R. Sugano, A. Hasegawa and H. Matsui, J. Nucl. Mater. 283–287 (2000) 827–831.

[335] Y.I. Zvezdin, O.M. Vishkarev, G.A. Tulyakov, Y.G. Magerya, V.A. Smirnov, I.A. Shenkova, I.V. Altovski, A.A. Grigoryan, V.K. Shamardin and U.M. Pecherin, J. Nucl. Mater. 191–194 (1992) 855–857.

[336] J. Chen, P. Jung, M. Rödig, H. Ullmaier and G.S. Bauer, J. Nucl. Mater. 343 (2005) 227–235.

[337] S.A. Maloy, A. Zubelewicz, T. Romero, M.R. James, W.F. Sommer and Y. Dai, J. Nucl. Mater. 343 (2005) 191–196.

[338] Y. de Carlan, X. Averty, J.C. Brachet, J.L. Bertin, F. Rozenblum, O. Rabouille and A. Bougault, J. ASTM Int. 2 (2005).

[339] N. Igata and H. Kayano, in: Effect of Radiation on Materials: 15th International Symposium, ASTM STP 1125, R.E. Stoller, A.S. Kumar, and D.S. Gelles, Eds., American Society for Testing and Materials, 1992, pp. 1243–1255.

[340] N. Igata, K. Miyahara, T. Uda and S. Asada, in: The Use of Small–Scale Specimens for Testing Irradiated Material, ASTM STP 888, W.R. Corwin and G.E. Lucas, Eds., American Society for Testing and Materials, 1986, pp. 161–170.

[341] F.A. Garner, M.L. Hamilton, H.L. Heinisch and A.S. Kumar, in: Small Specimen Test Techniques Applied to Nuclear Reactor Vessel Thermal Annealing and P¨lant Life Extension, ASTM STP 1204, W.R. Corwin, F.M. Haggag, and W.L. Server, Eds., American Society for Testing and Materials, 1993, pp. 336–355.

[342] A. Kohyama, S. Shato and K. Hamada, in: Small Specimen Test Techniques Applied to Nuclear Reactor Vessel Thermal Annealing and P¨lant Life Extension, ASTM STP 1204, W.R. Corwin,

F.M. Haggag, and W.L. Server, Eds., American Society for Testing and Materials, 1993, pp. 356–366.

[343] M.L. Hamilton, M.A. Blotter and D.J. Edwards, in: Small Specimen Test Techniques Applied to Nuclear Reactor Vessel Thermal Annealing and P¨lant Life Extension, ASTM STP 1204, W.R. Corwin, F.M. Haggag, and W.L. Server, Eds., American Society for Testing and Materials, 1993, pp. 368–381.

[344] W.N. Sharpe, Jr. and R.O. Fowler, in: Small Specimen Test Techniques Applied to Nuclear Reactor Vessel Thermal Annealing and P¨lant Life Extension, ASTM STP 1204, W.R. Corwin, F.M. Haggag, and W.L. Server, Eds., American Society for Testing and Materials, 1993, pp. 386–401.

[345] P. Jung, A. Hishinuma, G.E. Lucas and H. Ullmaier, J. Nucl. Mater. 232 (1996) 186–205.

[346] N.F. Panayotou, S.D. Atkin, R.J. Puigh and B.A. Chin, in: The Use of Small–Scale Specimens for Testing Irradiated Material, ASTM STP 888, W.R. Corwin and G.E. Lucas, Eds., American Society for Testing and Materials, 1986, pp. 201–219.

[347] G.R. Odette, M.Y. He, E.G. Donahue, P. Spätig and T. Yamamoto, J. Nucl. Mater. 307–311 (2002) 1011–1015.

[348] P. Spätig, E. Donahue, G.R. Odette, G.E. Lucas and M. Victoria, Mat. Res. Soc. Symp. Proc. Vol. 653 (2001) Z7.8.1–6.

[349] ASTM E1921, Standard test method for determination of reference temperature, T_0, for ferritic steels in the transition range, Annual Book of ASTM Standards, Section 3, Metals Test Methods and Analytical Procedures, Vol. 03.01, American Society for Testing and Materials, 2002.

[350] J. Henry, L. Vincent, X. Averty, B. Marini and P. Jung, J. Nucl. Mater. 356 (2006) 78–87.

[351] S. Yamashita, N. Akasaka, S. Ukai and S. Ohnuki, J. Nucl. Mater. 367–370 (2007) 202–207.

[352] E. Lucon, Tensile and fracture toughness properties of EUROFER ODS ("EU Batch" - 6 mm plate) in the unirradiated condition, SCK•CEN Report BLG–1024, 2006.

[353] E. Lucon, A. Leenaers and W. Vandermeulen, Post irradiation examination of a thermo-mechanically improved version of EUROFER ODS, SCK•CEN Report BLG–1028, 2006.

[354] E. Lucon, A. Leenaers and W. Vandermeulen, Fus. Eng. Des. 82 (2007) 2348–2443.

[355] A. Alamo, V. Lambard, X. Averty and M.H. Mathon, J. Nucl. Mater. 329–333 (2004) 333–337.

[356] M.A. Sokolov, D.T. Hoelzer, R.E. Stoller and D.A. McClintock, J. Nucl. Mater. 367–370 (2007) 213–216.

[357] R.L. Klueh, N. Hashimoto and P.J. Maziasz, J. Nucl. Mater. 367–370 (2007) 48–53.

[358] S. Ohtsuka, S. Ukai, H. Sakasegawa, M. Fujiwara, T. Kaito and T. Narita, J. Nucl. Mater. 367–370 (2007) 160–165.

[359] K. Yutani, H. Kishimoto, R. Kasada and A. Kimura, J. Nucl. Mater. 367–370 (2007) 423–427.

[360] R. Kasada, N. Toda, K. Yutani, H.S. Cho, H. Kishimoto and A. Kimura, J. Nucl. Mater. 367–370 (2007) 222–228.

[361] R.L. Klueh, N. Hashimoto and P.J. Maziasz , Sripta Mater. 53 (2005) 275–280.

ANNEX

RESULTS

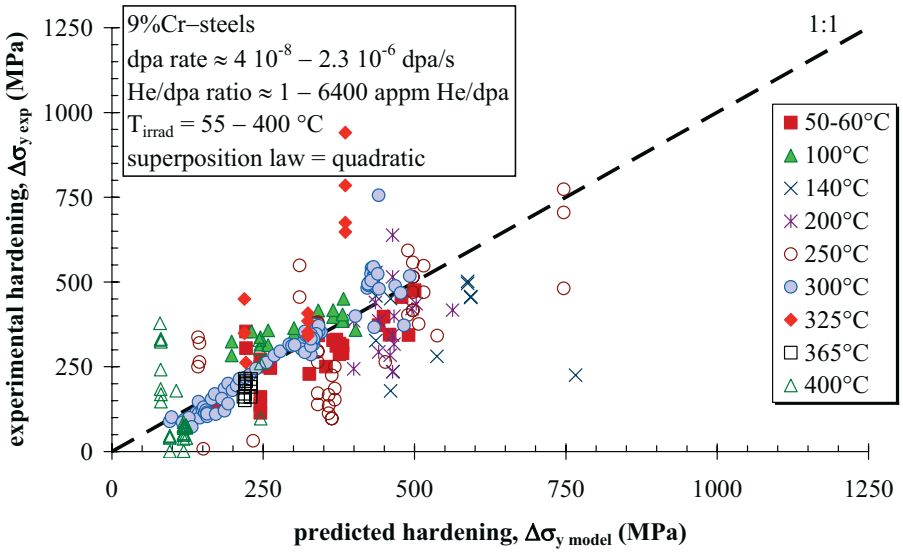
9%Cr–steels
dpa rate ≈ 4 10-8 – 2.3 10-6 dpa/s
He/dpa ratio ≈ 1 – 6400 appm He/dpa
Tirrad = 55 – 400 °C
superposition law = quadratic
1:1
50-60°C
100°C
140°C
200°C
250°C
300°C
325°C
365°C
400°C
experimental hardening, Δσy exp (MPa)
predicted hardening, Δσy model (MPa)
0
250
500
750
1000
1250

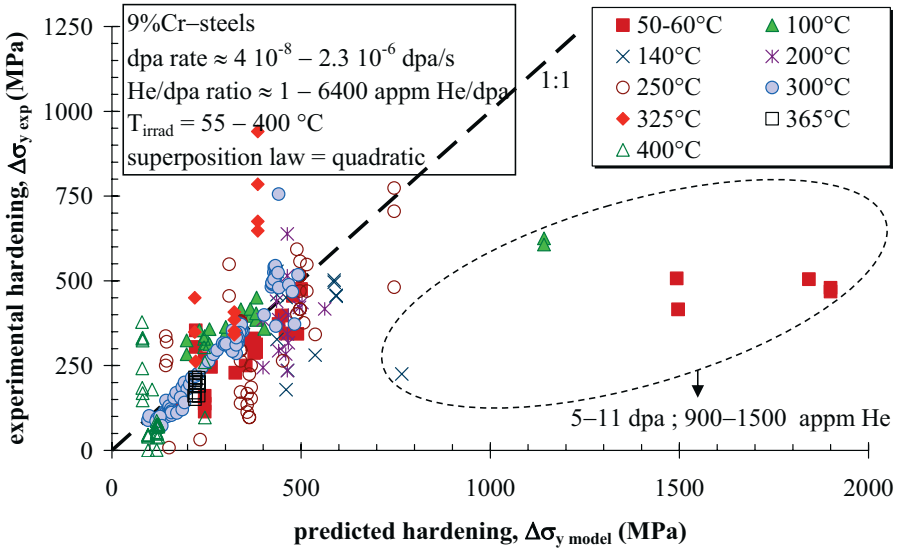
9%Cr–steels
dpa rate ≈ 4 10-8 – 2.3 10-6 dpa/s
He/dpa ratio ≈ 1 – 6400 appm He/dpa
Tirrad = 55 – 400 °C
superposition law = quadratic
1:1
50-60°C
100°C
140°C
200°C
250°C
300°C
325°C
365°C
400°C
5–11 dpa ; 900–1500 appm He
experimental hardening, Δσy exp (MPa)
predicted hardening, Δσy model (MPa)
0
250
500
750
1000
1250
1500
2000

Low He–production rate (<1 appm He/dpa / neutron irradiation)

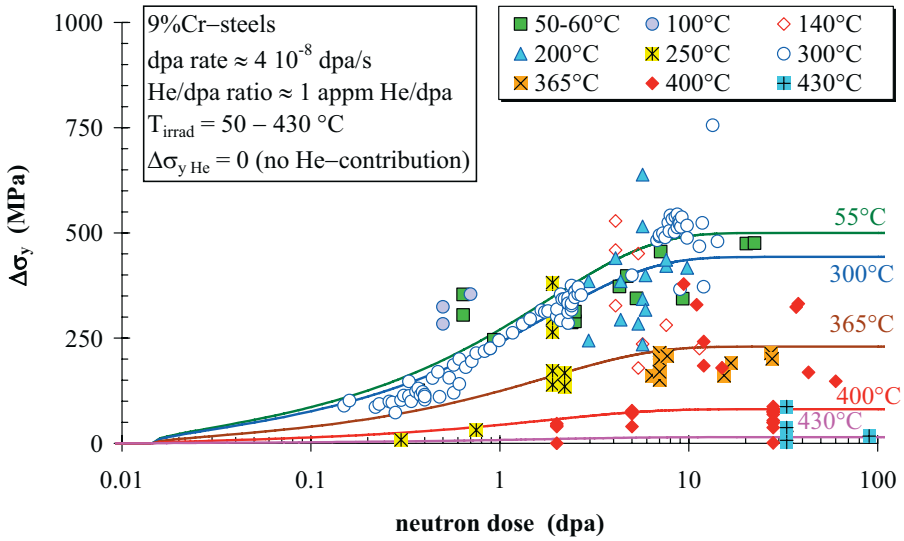

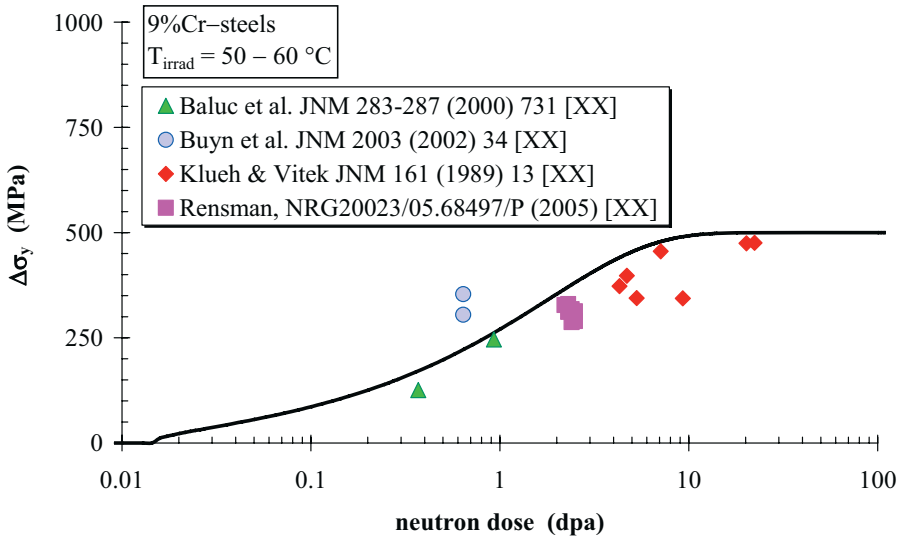

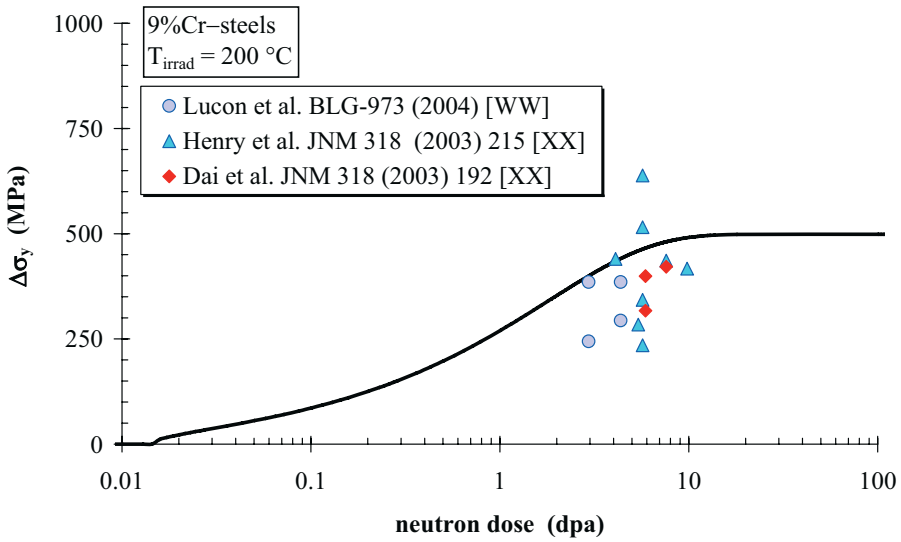
9%Cr–steels
T irrad = 200 °C
Lucon et al. BLG-973 (2004) [WW]
Henry et al. JNM 318 (2003) 215 [XX]
Dai et al. JNM 318 (2003) 192 [XX]
Δσy (MPa)
1000
750
500
250
0
0.01
0.1
1
10
100
neutron dose (dpa)

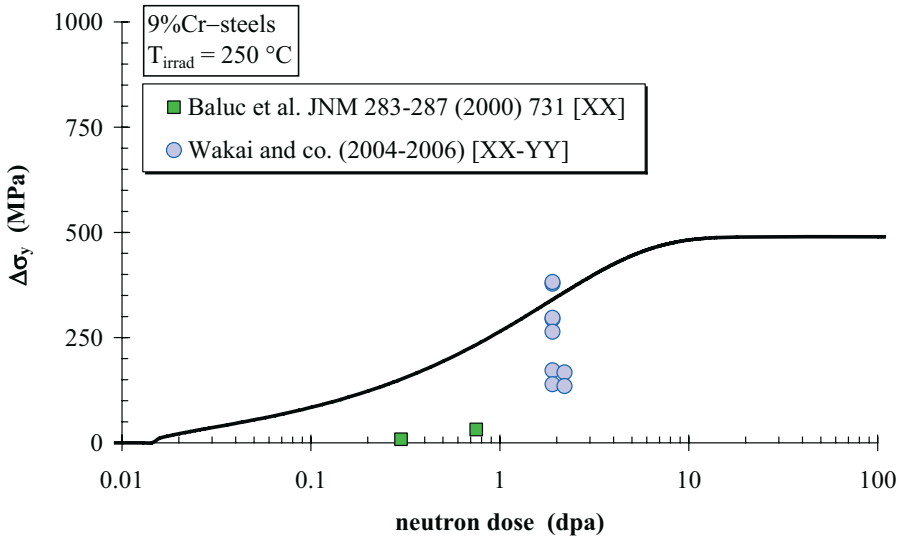
9%Cr–steels
T irrad = 250 °C
Baluc et al. JNM 283-287 (2000) 731 [XX]
Wakai and co. (2004-2006) [XX-YY]
Δσy (MPa)
1000
750
500
250
0
0.01
0.1
1
10
100
neutron dose (dpa)

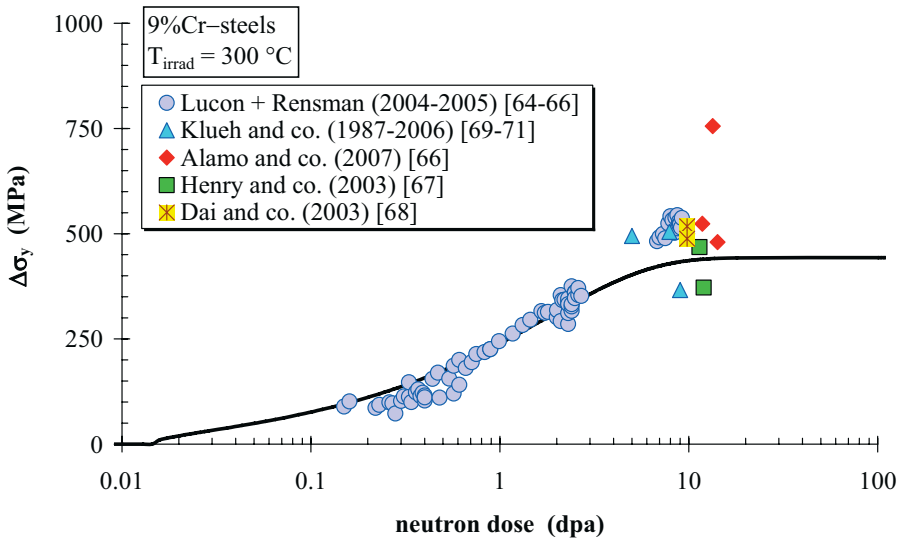
9%Cr–steels
T_irrad = 300 °C
Lucon + Rensman (2004-2005) [64-66]
Klueh and co. (1987-2006) [69-71]
Alamo and co. (2007) [66]
Henry and co. (2003) [67]
Dai and co. (2003) [68]
Δσy (MPa)
1000
750
500
250
0
0.01
0.1
1
10
100
neutron dose (dpa)

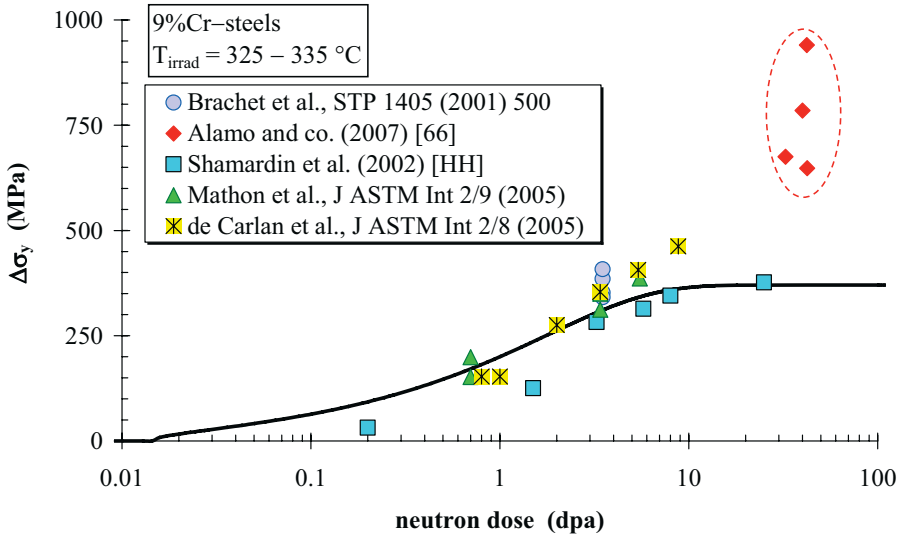
9%Cr–steels
T_irrad = 325 – 335 °C
Brachet et al., STP 1405 (2001) 500
Alamo and co. (2007) [66]
Shamardin et al. (2002) [HH]
Mathon et al., J ASTM Int 2/9 (2005)
de Carlan et al., J ASTM Int 2/8 (2005)
Δσy (MPa)
1000
750
500
250
0
0.01
0.1
1
10
100
neutron dose (dpa)

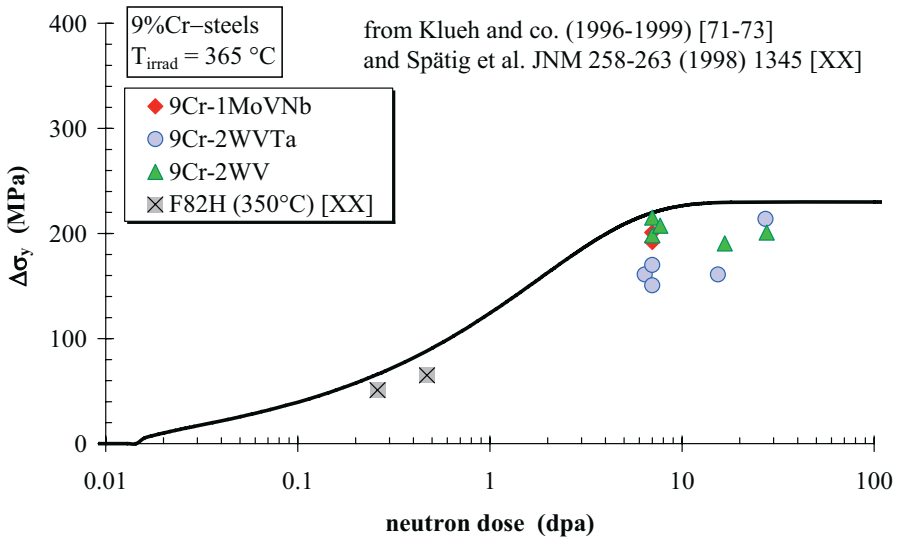
9%Cr–steels
T irrad = 365 °C
from Klueh and co. (1996-1999) [71-73]
and Spätig et al. JNM 258-263 (1998) 1345 [XX]
9Cr-1MoVNb
9Cr-2WVTa
9Cr-2WV
F82H (350°C) [XX]
Δσy (MPa)
neutron dose (dpa)

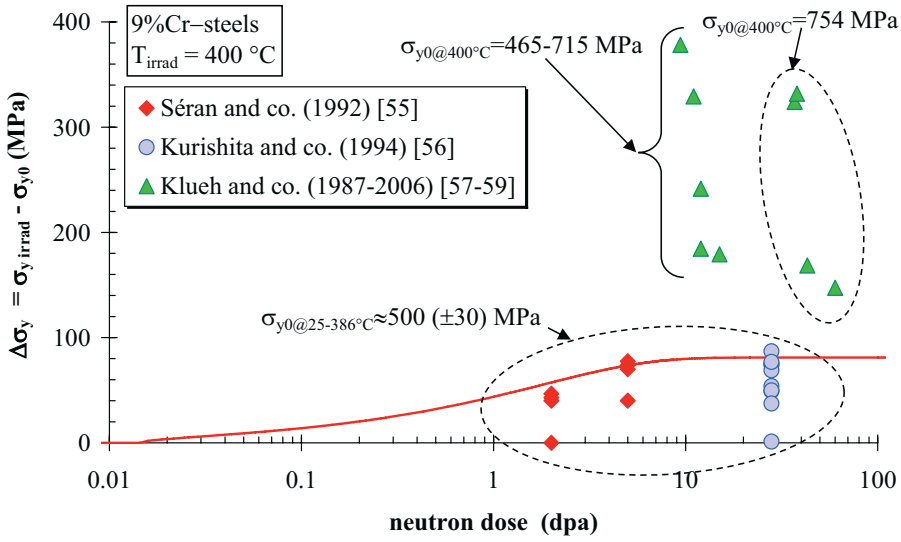
9%Cr–steels
T irrad = 400 °C
Séran and co. (1992) [55]
Kurishita and co. (1994) [56]
Klueh and co. (1987-2006) [57-59]
σy0@400°C=465-715 MPa
σy0@400°C=754 MPa
σy0@25-386°C≈500 (±30) MPa
Δσy = σy irrad - σy0 (MPa)
neutron dose (dpa)

Medium He–production rate (~100 appm He/dpa / proton irradiation)

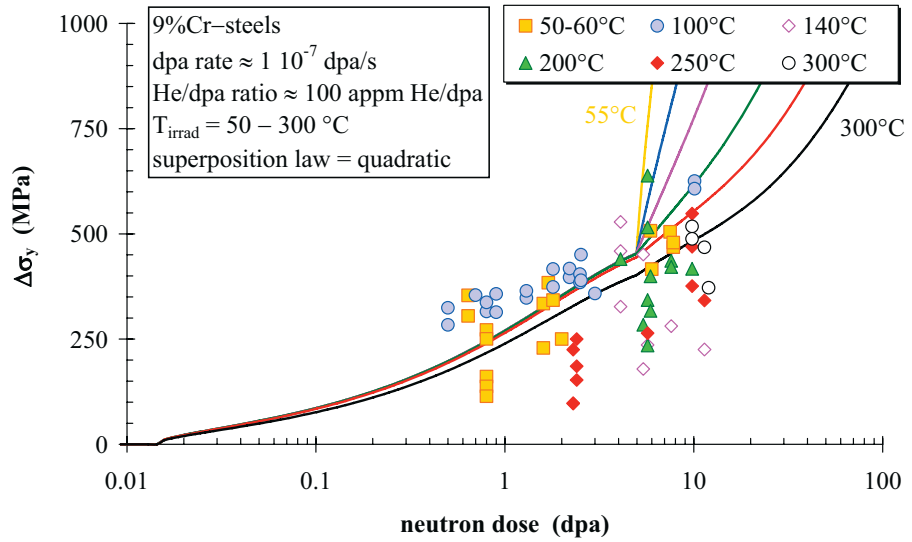

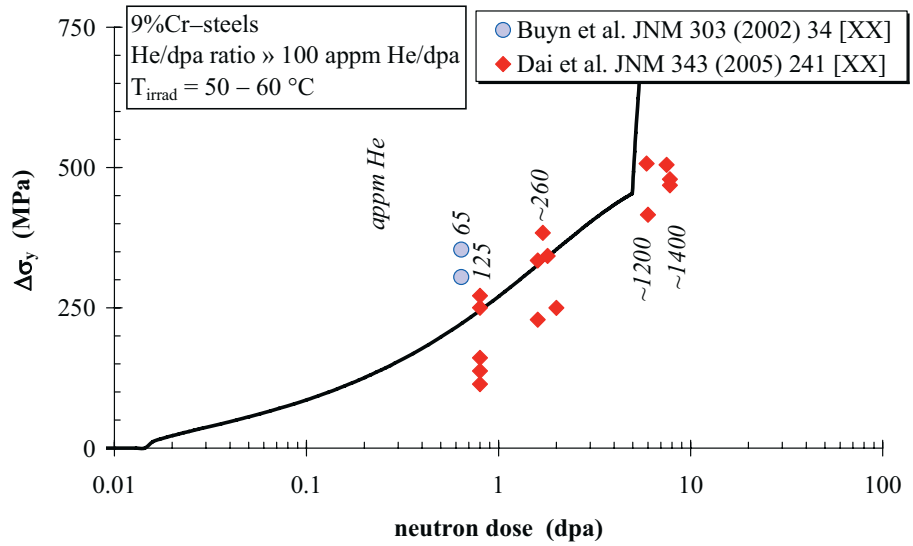

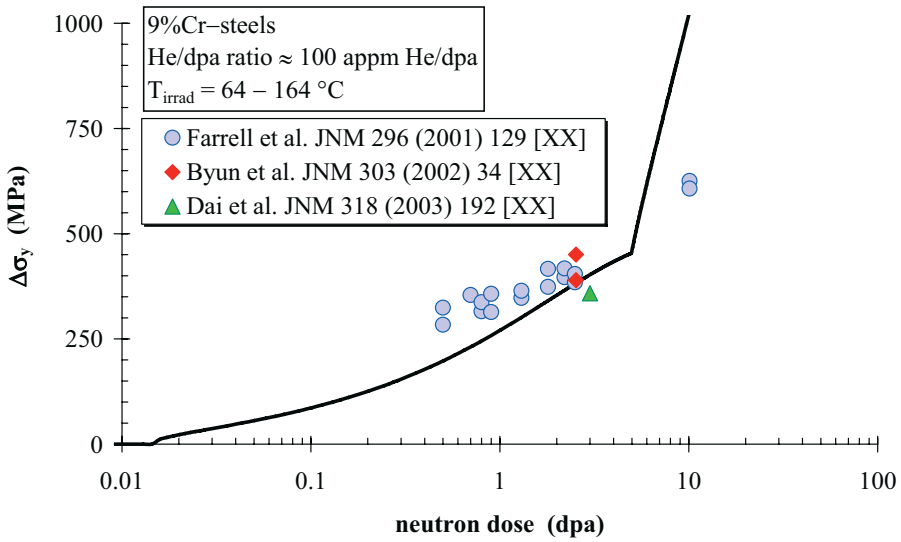
9%Cr–steels
He/dpa ratio ≈ 100 appm He/dpa
T_irrad = 64 – 164 °C
Farrell et al. JNM 296 (2001) 129 [XX]
Byun et al. JNM 303 (2002) 34 [XX]
Dai et al. JNM 318 (2003) 192 [XX]
Δσ_y (MPa)
1000
750
500
250
0
0.01
0.1
1
10
100
neutron dose (dpa)

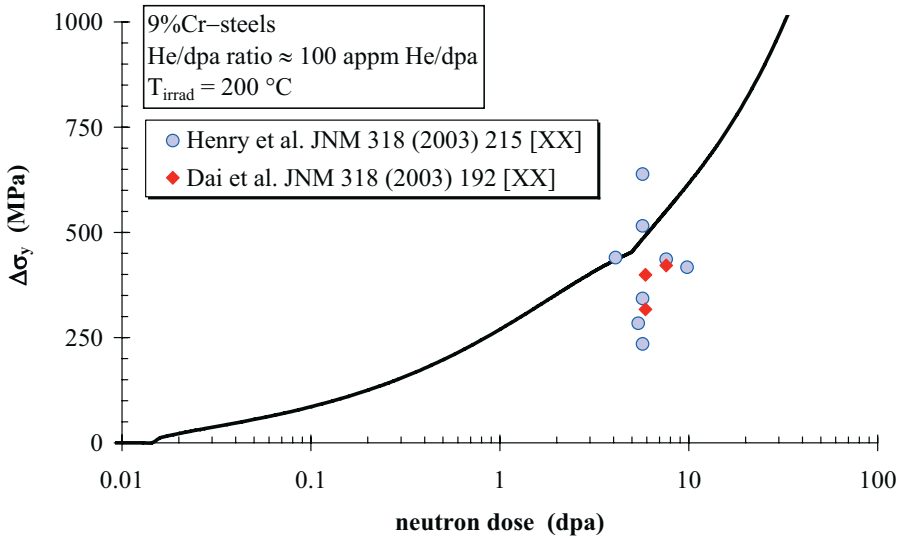
9%Cr–steels
He/dpa ratio ≈ 100 appm He/dpa
T_irrad = 200 °C
Henry et al. JNM 318 (2003) 215 [XX]
Dai et al. JNM 318 (2003) 192 [XX]
Δσ_y (MPa)
1000
750
500
250
0
0.01
0.1
1
10
100
neutron dose (dpa)

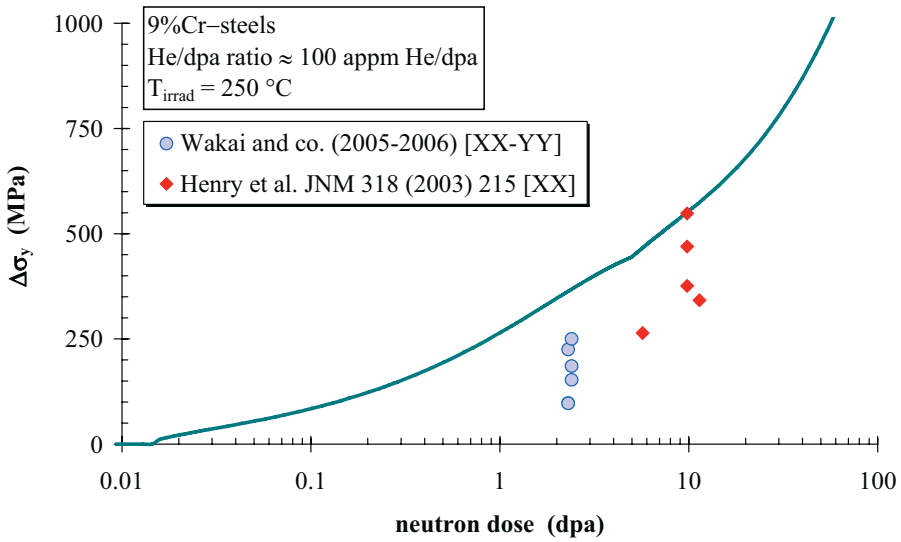
9%Cr–steels
He/dpa ratio ≈ 100 appm He/dpa
T_irrad = 250 °C
Wakai and co. (2005-2006) [XX-YY]
Henry et al. JNM 318 (2003) 215 [XX]
Δσ_y (MPa)
1000
750
500
250
0
0.01
0.1
1
10
100
neutron dose (dpa)

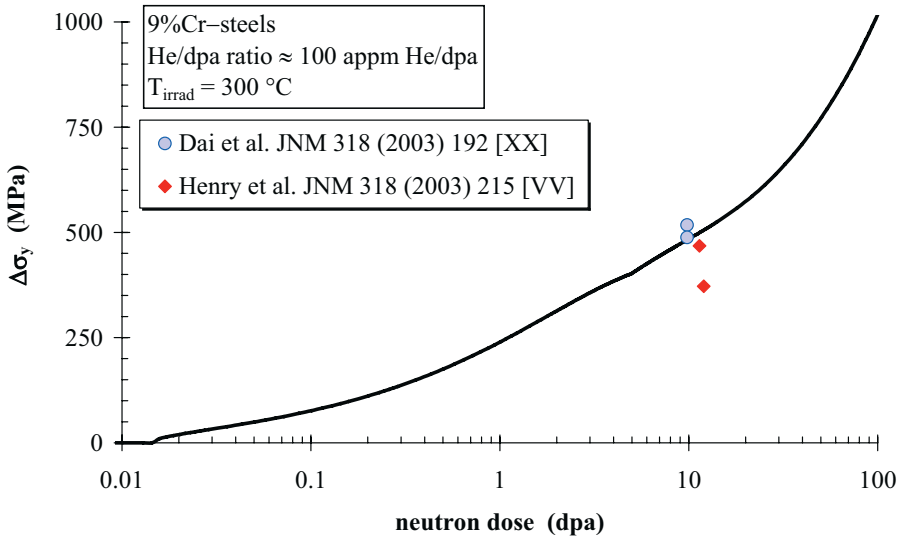
9%Cr–steels
He/dpa ratio ≈ 100 appm He/dpa
T_irrad = 300 °C
Dai et al. JNM 318 (2003) 192 [XX]
Henry et al. JNM 318 (2003) 215 [VV]
Δσ_y (MPa)
1000
750
500
250
0
0.01
0.1
1
10
100
neutron dose (dpa)

High He–production rate (~6400 appm He/dpa / He–implantation)

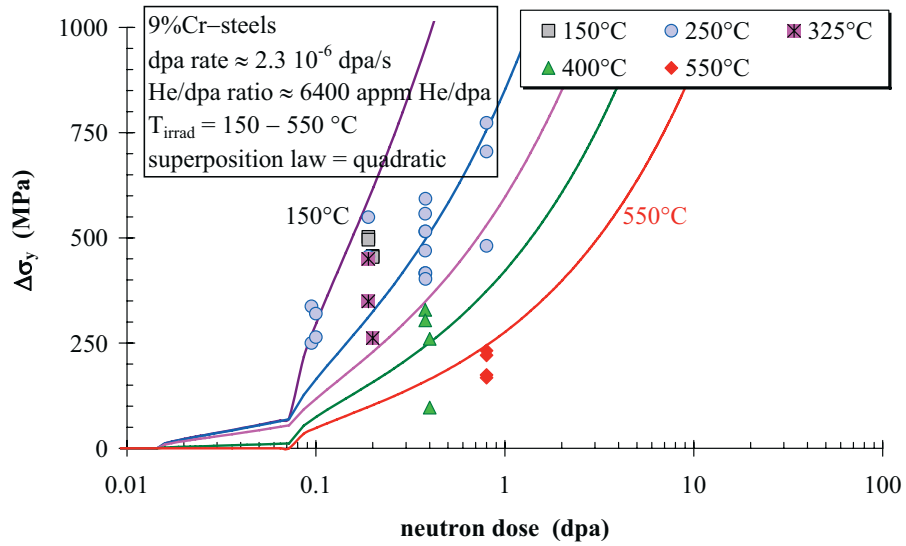

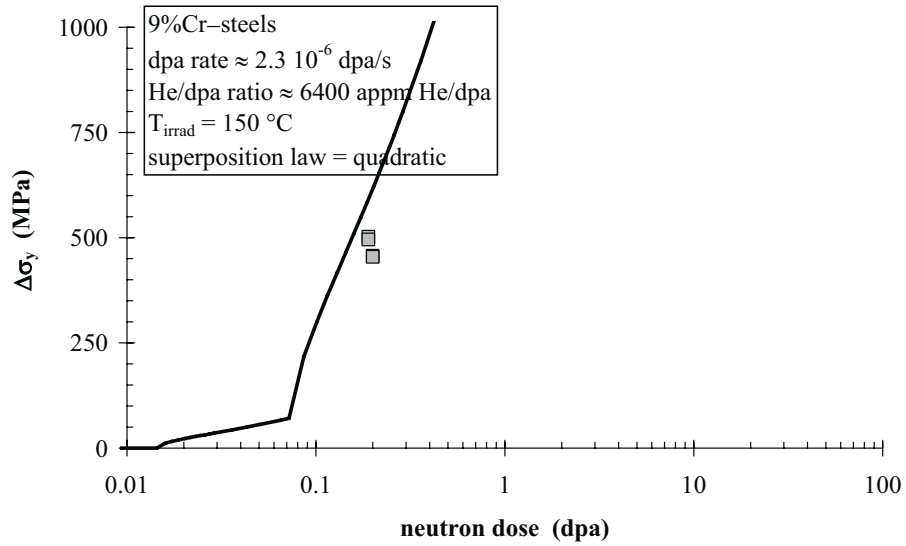

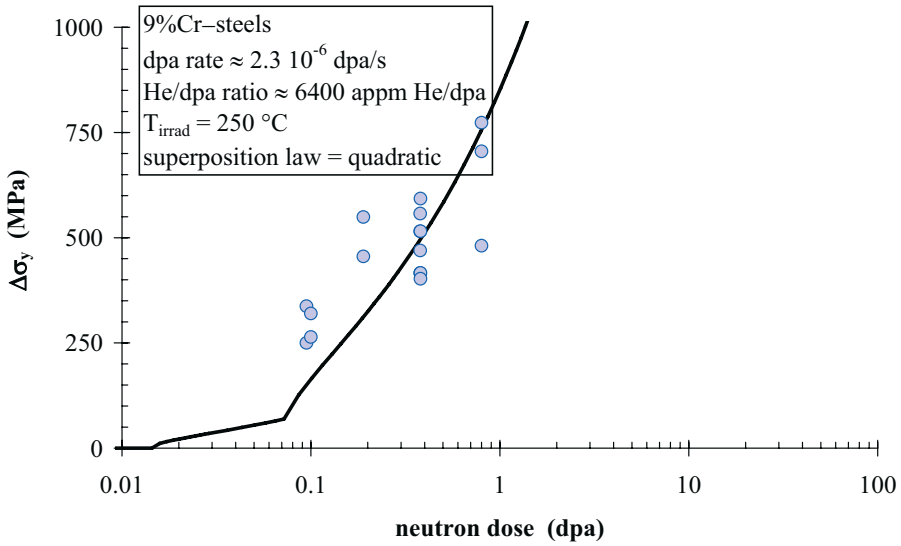
9%Cr–steels
dpa rate ≈ 2.3 10-6 dpa/s
He/dpa ratio ≈ 6400 appm He/dpa
Tirrad = 250 °C
superposition law = quadratic
1000
750
500
250
0
Δσy (MPa)
0.01
0.1
1
10
100
neutron dose (dpa)

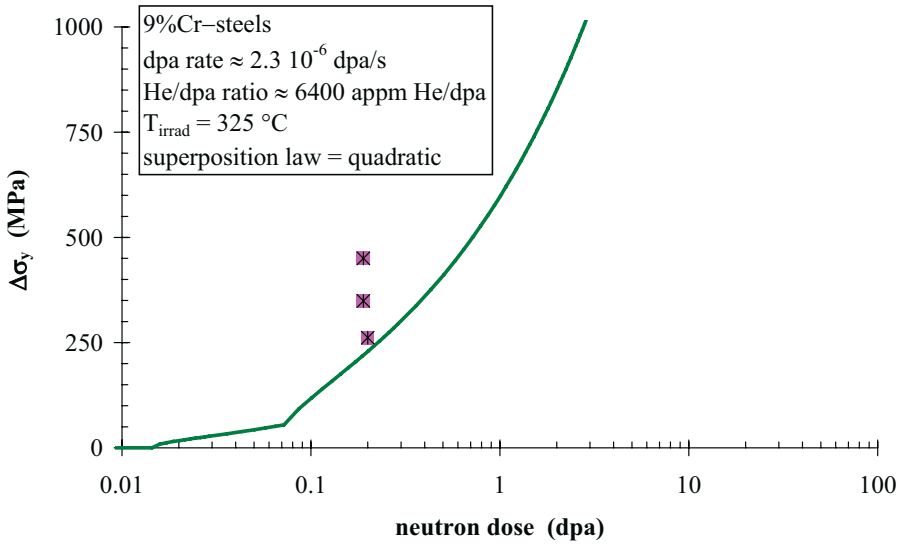
9%Cr–steels
dpa rate ≈ 2.3 10-6 dpa/s
He/dpa ratio ≈ 6400 appm He/dpa
Tirrad = 325 °C
superposition law = quadratic
1000
750
500
250
0
Δσy (MPa)
0.01
0.1
1
10
100
neutron dose (dpa)

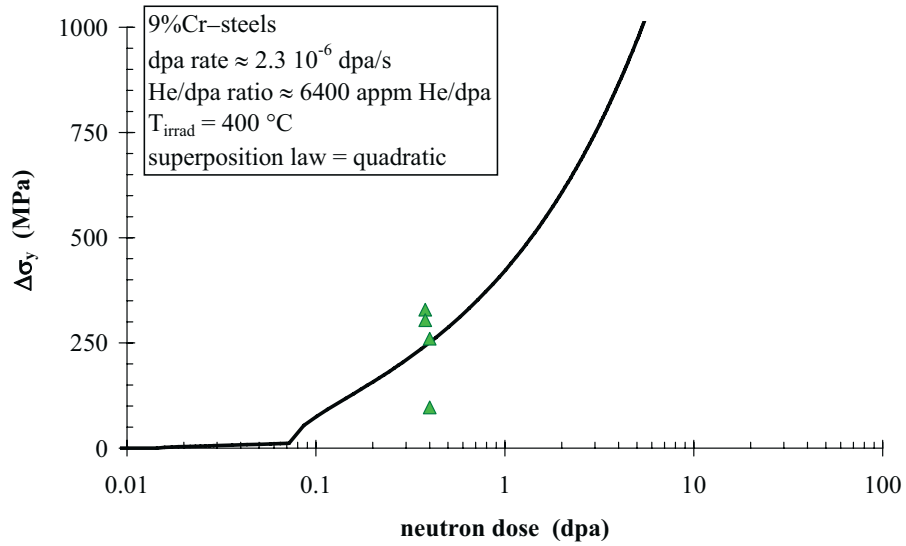
9%Cr–steels
dpa rate ≈ 2.3 10-6 dpa/s
He/dpa ratio ≈ 6400 appm He/dpa
Tirrad = 400 °C
superposition law = quadratic
Δσy (MPa)
1000
750
500
250
0
0.01
0.1
1
10
100
neutron dose (dpa)

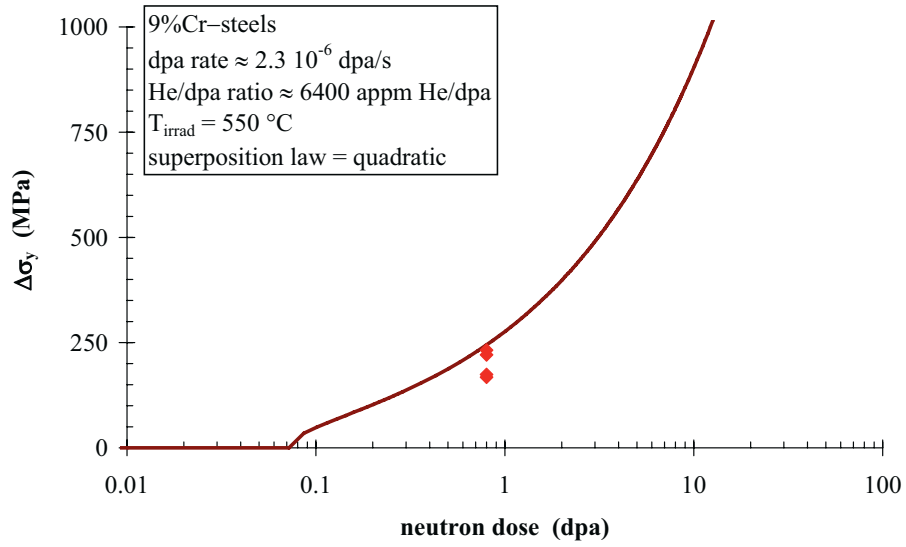
9%Cr–steels
dpa rate ≈ 2.3 10-6 dpa/s
He/dpa ratio ≈ 6400 appm He/dpa
Tirrad = 550 °C
superposition law = quadratic
Δσy (MPa)
1000
750
500
250
0
0.01
0.1
1
10
100
neutron dose (dpa)

1. **Einsatz von multispektralen Satellitenbilddaten in der Wasserhaushalts- und Stoffstrommodellierung – dargestellt am Beispiel des Rureinzugsgebietes**
   von C. Montzka (2008), XX, 238 Seiten
   ISBN: 978-3-89336-508-1

2. **Ozone Production in the Atmosphere Simulation Chamber SAPHIR**
   by C. A. Richter (2008), XIV, 147 pages
   ISBN: 978-3-89336-513-5

3. **Entwicklung neuer Schutz- und Kontaktierungsschichten für Hochtemperatur-Brennstoffzellen**
   von T. Kiefer (2008), 138 Seiten
   ISBN: 978-3-89336-514-2

4. **Optimierung der Reflektivität keramischer Wärmedämmschichten aus Yttrium-teilstabilisiertem Zirkoniumdioxid für den Einsatz auf metallischen Komponenten in Gasturbinen**
   von A. Stuke (2008), X, 201 Seiten
   ISBN: 978-3-89336-515-9

5. **Lichtstreuende Oberflächen, Schichten und Schichtsysteme zur Verbesserung der Lichteinkopplung in Silizium-Dünnschichtsolarzellen**
   von M. Berginski (2008), XV, 171 Seiten
   ISBN: 978-3-89336-516-6

6. **Politikszenarien für den Klimaschutz IV – Szenarien bis 2030**
   hrsg.von P. Markewitz, F. Chr. Matthes (2008), 376 Seiten
   ISBN 978-3-89336-518-0

7. **Untersuchungen zum Verschmutzungsverhalten rheinischer Braunkohlen in Kohledampferzeugern**
   von A. Schlüter (2008), 164 Seiten
   ISBN 978-3-89336-524-1

8. **Inorganic Microporous Membranes for Gas Separation in Fossil Fuel Power Plants**
   by G. van der Donk (2008), VI, 120 pages
   ISBN: 978-3-89336-525-8

9. **Sinterung von Zirkoniumdioxid-Elektrolyten im Mehrlagenverbund der oxidkeramischen Brennstoffzelle (SOFC)**
   von R. Mücke (2008), VI, 165 Seiten
   ISBN: 978-3-89336-529-6

10. **Safety Considerations on Liquid Hydrogen**
    by K. Verfondern (2008), VIII, 167 pages
    ISBN: 978-3-89336-530-2

11. **Kerosinreformierung für Luftfahrtanwendungen**
    von R. C. Samsun (2008), VII, 218 Seiten
    ISBN: 978-3-89336-531-9

12. **Der 4. Deutsche Wasserstoff Congress 2008 – Tagungsband**
    hrsg. von D. Stolten, B. Emonts, Th. Grube (2008), 269 Seiten
    ISBN: 978-3-89336-533-3

13. **Organic matter in Late Devonian sediments as an indicator for environmental changes**
    by M. Kloppisch (2008), XII, 188 pages
    ISBN: 978-3-89336-534-0

14. **Entschwefelung von Mitteldestillaten für die Anwendung in mobilen Brennstoffzellen-Systemen**
    von J. Latz (2008), XII, 215 Seiten
    ISBN: 978-3-89336-535-7

15. **RED-IMPACT**
    Impact of Partitioning, Transmutation and Waste Reduction Technologies on the Final Nuclear Waste Disposal
    SYNTHESIS REPORT
    ed. by W. von Lensa, R. Nabbi, M. Rossbach (2008), 178 pages
    ISBN 978-3-89336-538-8

16. **Ferritic Steel Interconnectors and their Interactions with Ni Base Anodes in Solid Oxide Fuel Cells (SOFC)**
    by J. Froitzheim (2008), 169 pages
    ISBN: 978-3-89336-540-1

17. **Integrated Modelling of Nutrients in Selected River Basins of Turkey**
    Results of a bilateral German-Turkish Research Project
    project coord. M. Karpuzcu, F. Wendland (2008), XVI, 183 pages
    ISBN: 978-3-89336-541-8

18. **Isotopengeochemische Studien zur klimatischen Ausprägung der Jüngeren Dryas in terrestrischen Archiven Eurasiens**
    von J. Parplies (2008), XI, 155 Seiten, Anh.
    ISBN: 978-3-89336-542-5

19. **Untersuchungen zur Klimavariabilität auf dem Tibetischen Plateau – Ein Beitrag auf der Basis stabiler Kohlenstoff- und Sauerstoffisotope in Jahrringen von Bäumen waldgrenznaher Standorte**
    von J. Grießinger (2008), XIII, 172 Seiten
    ISBN: 978-3-89336-544-9

20. **Neutron-Irradiation + Helium Hardening & Embrittlement Modeling of 9%Cr-Steels in an Engineering Perspective (HELENA)**
by R. Chaouadi (2008), VIII, 139 pages
ISBN: 978-3-89336-545-6

Abstract

This report provides a physically-based engineering model to estimate the radiation hardening of 9%Cr-steels under both displacement damage (dpa) and helium. The model is essentially based on the dispersed barrier hardening theory and the dynamic re-solution of helium under displacement cascades. The parameters of the model were experimentally derived using a database. The model and its performance and limitation are extensively discussed.

Author

Dr. Rachid Chaouadi is a senior scientist from the Belgian Nuclear Research Centre in the field of radiation effects on structural materials. He is mainly involved in the evaluation of radiation effects on reactor pressure vessel steels and various fusion materials. During his sabbatical stay at the Forschungszentrum Jülich, Germany, he performed the present work within the frame of the HELENA project, sponsored by the European Commission.

Institute of Energy Research
IEF-2 Materials Microstructure and Characterization

The research topics of IEF-2 are focussed on the development and characterization of materials for efficient gas and steam power plants, for high temperature fuel cells and for future fusion reactor components subjected to high thermal loads. The scientific expertises of the institute cover microstructural investigations, surface analysis techniques and the physical, chemical, mechanical and corrosion behaviour of metallic high temperature materials and of ceramic materials used either as structural components or as elements of coating systems.

Band | Volume 20
ISBN 978-3-89336-545-6

JÜLICH
FORSCHUNGSZENTRUM